CORA Cork Open Research Archive
Cartlann Taighde Oscailte Chorcaí

Title	Rate-induced tipping to metastable Zombie fires
Authors	O'Sullivan, Eoin
Publication date	2023
Original Citation	O'Sullivan, E. G. 2023. Rate-induced tipping to metastable Zombie fires. PhD Thesis, University College Cork.
Type of publication	Doctoral thesis
Rights	© 2023, Eoin O'Sullivan. - https://creativecommons.org/licenses/by/4.0/
Download date	2026-11-08 00:12:24
Item downloaded from	https://hdl.handle.net/10468/15016



UCC
University College Cork, Ireland
Coláiste na hOllscoile Corcaigh

Rate-induced Tipping to Metastable Zombie Fires



Thesis presented by
Eoin O'Sullivan

for the degree of
Doctor of Philosophy

University College Cork
School of Mathematical Sciences

Head of School: Dr. Kevin Hayes
Head of Discipline: Prof. Sebastian Wieczorek

Supervisors: Dr. Kieran Mulchrone, Prof. Sebastian Wieczorek

2023

Contents

1 Introduction **2**

1.1 Arctic Peatlands 2

1.2 Tipping Points 4

1.3 R-tipping in a Toy Model 6

1.4 Excitable Systems 10

1.5 Fast-Slow Dynamical Systems 12

1.6 Excitability Quasithresholds: Fitzhugh-Nagumo 17

1.7 Background Summary and Thesis Structure 21

2 The Nonautonomous Soil-Carbon Model **25**

2.1 The Model Equations 25

2.2 Soil-to-Atmosphere Heat Transfer 26

2.3 Modified Microbial Respiration 28

2.4 The Autonomous Frozen System and the Moving Equilibrium . 29

2.5 R-tipping to a Hot Metastable State and Zombie Fires 31

2.6 Excitability in The Nonautonomous Soil-Carbon Model 34

3 The Autonomous Compactified Soil-Carbon Model **37**

3.1 Asymptotically Constant External Inputs 37

3.2 Compactification 38

3.2.1 Continuous Differentiability of The Compactified System 40

3.2.2 Special Case: Compactification Using The External Input 41

3.3 Stability of Equilibria for the Compactified System 42

3.4 Timescales of The Autonomous Compactified Soil-Carbon Model 42

4 Defining R-tipping due to Crossing Quasithresholds 47
4.1 Quasithresholds in The Frozen System 47
4.2 Quasithresholds vs Regular Thresholds 52
4.3 Threshold Instability for Quasithresholds 53
4.4 R-tipping Mechanism for an Instantaneous Switch 54
4.5 R-tipping Mechanism for a Super-Fast Shift 56
4.6 Adiabatically Slow System 56
4.7 Parameter Sensitivity of The Frozen System 59
4.8 Hopf Bifurcation and Relaxation Oscillations 59

5 R-tipping mechanisms for Global Warming 63
5.1 R-tipping and Canards in The Compactified System 63
5.2 The Desingularised Reduced Problem 66
5.2.1 Three R-tipping Cases for $\epsilon = 0$ 69
5.2.2 The simple case 72
5.2.3 The complicated case 72
5.2.4 The degenerate case 75
5.3 Bringing it Together: Unfolding of Global FSN-I 77
5.4 Secondary and Composite Canards 81
5.4.1 Secondary Canards 81
5.4.2 Composite Canards 83
5.5 R-tipping Tongues 84
5.6 Approximating the Critical Rate 88

6 R-tipping mechanisms for Summer Heatwaves 92
6.1 R-tipping and Canards in The Compactified System 92
6.2 The Layer Problem 95
6.3 Bringing it Together: Saddle-to-Saddle Heteroclinic Orbit 100
6.4 Approximating the Critical Rate 102

7 Numerical Methods for Duck Hunting in C# 104
7.1 The Compactified System 104
7.2 Adaptive Stepsize Control 105
7.3 R-tipping Diagrams 107

7.4 Hunting Secondary and Composite Canards 110
7.5 Computing Slow Manifolds 111

8 Conclusion and Outlook **116**

A Details for Figures **119**
A.1 Details for Figure 1 119
A.2 External Input and Parameter Details for Figure 2 119
A.3 External Input and Parameter Details for Figure 3 120
A.4 External Input and Parameter Details for Figure 4 120

B Additional Derivations **121**
B.1 Threshold Instability Condition 121
B.2 Compactified Summer Heatwave 122

C Table of Parameters **123**

Declaration

This is to certify that the work I am submitting is my own and has not been submitted for another degree, either at University College Cork or elsewhere. All external references and sources are clearly acknowledged and identified within the contents. I have read and understood the regulations of University College Cork concerning plagiarism and intellectual property.

Abstract

Surface wildfires are generally believed to be the cause of so-called *Zombie fires* observed in peatlands, that disappear from the surface, smoulder underground during the winter, and "come back to life" in the spring. Here, we propose rate-induced tipping (R-tipping) to a *subsurface hot metastable state* in bioactive peat soils as a main cause of Zombie fires. Our hypothesis is based on a conceptual soil-carbon model subjected to realistic changes in weather and climate patterns, including global warming scenarios and summer heatwaves.

Mathematically speaking, R-tipping to the hot metastable state is a nonautonomous instability, due to crossing an elusive *quasithreshold*, in a multiple-timescale dynamical system. The instability is *reversible*, in the sense that the system eventually returns to its base state. To explain this instability, we provide a framework that combines a special compactification technique with concepts from geometric singular perturbation theory. This framework allows us to reduce a reversible R-tipping problem due to crossing a quasithreshold to a heteroclinic orbit problem in a singular limit. Thus, we identify generic cases of such R-tipping via: (i) unfolding of a codimension-two *heteroclinic folded saddle-node type-I singularity* for global warming, and (ii) analysis of a codimension-one *saddle-to-saddle hetroclinic orbit* for summer heatwaves, which in turn reveal new types of excitability quasithresholds.

Acknowledgements

First, I would like to thank ATSR ltd. for funding my work. I would like to thank my supervisor Kieran Mulchrone for his patience, guidance and generosity. It is often said that your choice of supervisor is the biggest determiner of your PhD experience, and I can confidently say that my choice was the correct one. Between a global pandemic and moving countries, a lot has happened in four years and it is a testament to him that I have made it to end. I would like to thank Sebastian Wieczorek for first introducing me to the fascinating topic of rate-induced tipping in peat soils, as well as for his his time, patience and insight throughout. His input has always been considered and invaluable, with a way of bringing a new perspective to any problem I was working on. Kieran and Sebastian brought complimentary perspectives to my supervision, and I believe this is reflected in the quality of the final work. I would like to thank my parents Marie and Donal, as well as my brothers Rory and Tadhg for their support, encouragement and advice. Finally, I would like to thank my partner Astrid who has shown me more patience and understanding than I could have ever asked for.

Chapter 1

Introduction

This thesis examines reversible rate-induced tipping due to crossing a quasithreshold in a conceptual soil-carbon model incorporating a time varying climatic input and physical processes that evolve on multiple timescales. In this background chapter, we review some of the scientific and mathematical results which support this work. First, we discuss Arctic Peatlands and the physical conditions that motivate studying their response to climate change. Second, we discuss tipping points, and in particular the concept of reversible R-tipping. Third, we discuss excitability, and explain the connection between this extensively studied phenomenon and reversible R-tipping. Fourth, we discuss the theory of multiple timescale dynamical systems (referred to as geometric singular perturbation theory), and state the Fenichel Theorems, which will be relied upon throughout this work. We apply the techniques of geometric singular perturbation theory to study excitability in the classical Fitzhugh-Nagumo model, illustrarting the concept of a quasithreshold and showing how such techniques may be used to understand reversible R-tipping due to crossing quasithresholds. Finally, we provide a summary and outline the structure of this thesis.

1.1 Arctic Peatlands

The main motivation for this thesis is a combination of two environmental features of the Arctic. First is the organic carbon content. Estimates for the

organic carbon contained in Northern and Arctic permafrost peat soil alone range from approximately 500Gt [119] to approximately 1700Gt [93, 71, 66]. For comparison, the atmospheric carbon pool is estimated to be approximately 850 Gt [64]. Second is the rate of atmospheric warming and the increasing trends in summer heatwaves. Due to so called "Arctic Amplification" [89], both the so-far observed and future predicted warming for Arctic regions are approximately double the global mean [73]. This means that the Arctic is home to massive deposits of ancient peat carbon and is the fastest warming region on the planet. To visualise this combination of environmental features we combine in figure 1.1 (colourscale) recent rates of global warming[1] obtained from the Berkeley Earth [5, 85] global temperature dataset and (greyscale) the global distribution of peat soils obtained from the PEATMAP dataset [118]. In addition to the increase in the mean global temperature, there is an increase in the intensity, frequency and duration of summer heatwaves in the Northern Hemisphere [4, 75], with the Arctic temperature record a scorching 38°C in 2020 [1]. Since peat soils are bioactive and thus temperature sensitive [69], such conditions can lead to a tipping point as we show here. This is the reason why northern latitude peat-soils were identified as a potential tipping element in [57]. To the best of our knowledge, the first example of R-tipping in peat soils triggered by atmospheric warming was reported, but not emphasised, by Khvorostyanov et al. [45, Fig.4(a)]. Later, Luke and Cox [60] proposed a conceptual soil-carbon model that exhibits a short-lived explosive release of soil carbon into the atmosphere above some critical rate of global warming, which they termed the "compost-bomb instability"; see also [26]. The dynamical mechanism responsible for this instability was explained by Wieczorek et al. [112]. Additionally, it has been known that spontaneous combustion is the main cause of fires at composting facilities [21], which can then spread, e.g. the recent Wennington fire in London [87, 104].

[1]Note that these recent short-term rates of global warming exceed the long-term rates in the CMIP5 outputs.

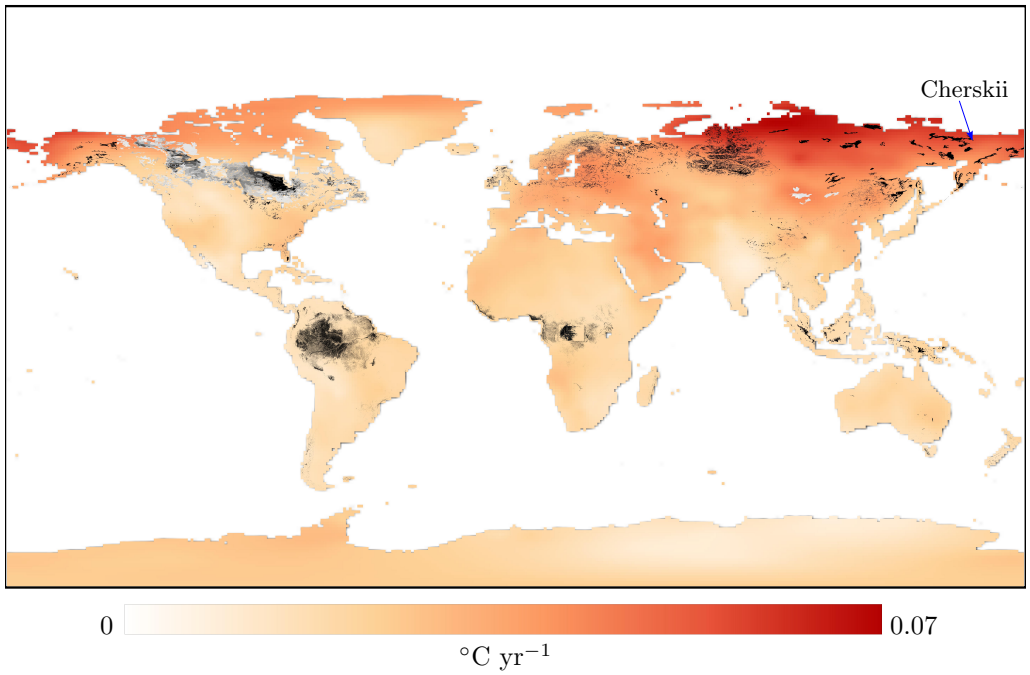


Figure 1.1: (Colourscale) Historical global rates of warming from the period 1951-1980 to the period 2017-2021 obtained using observations compiled by Berkeley Earth [5, 85], together with (black and gray) the global distribution of peat soils obtained from PEATMAP [118]. Note the largest warming rates at higher latitudes, in areas with a significant concentration of peat soils, such as (blue arrow) Cherskii in Northern Siberia.

1.2 Tipping Points

Tipping points, or critical transitions, are instabilities known to occur in natural and human systems subjected to changing external conditions, or external inputs. They may be explained in layman's terms as a sudden and large change in the state of a system in response to a small or slow change in the external input. The change in the state of the system may be permanent or transient.

Interest in the study of tipping points has accelerated due to theorised [57, 84] and observed [23, 18] tipping points in the earth system caused by climate change. Earth subsystems may be thought of as dynamical systems with their own *internal* dynamics and state variables, with the changing climate playing

the role of a changing *external* variable or input. It is theorised that climate change may cause some earth subsystems to cross tipping points, providing either potential feedback for climate change or catastrophic consequences in their own right [20]. Many of the tipping elements identified in [57], for example the loss of Arctic sea ice or the shutdown of the Atlantic Meridional Overturning Circulation, can be captured by elaborate, high-resolution mathematical models referred to as General Circulation Models (GCMs). Additionally, there are tipping elements in the earth system that are not captured by GCMs, such as Amazon rainforest dieback [27, 19], that may have an equally strong global impact. In this thesis, we use a conceptual soil-carbon model with time-varying climate as an external input to describe one such tipping element, namely a release of gigatonnes of carbon from temperature-sensitive peat soils into the atmosphere.

Owing to the explicit time dependence of the external input, the ensuing dynamical system is nonautonomous. This means that analysis of tipping points requires, in general, techniques beyond classical autonomous stability theory [112, 13, 9, 47, 72, 59, 53, 10, 113]. Nonetheless, it is useful to consider the corresponding *autonomous frozen system* with fixed-in-time inputs. In the frozen system we identify a desired stable state, and refer to this state as the *base state*. When the external input changes over time, the shape and position of the base state may change too, and the nonautonomous system will try to *track* the moving base state. However, in some cases tracking is not possible and tipping occurs. Ashwin *et al* [12] identified three generic mechanisms for tipping [2] :

(i) *Bifurcation-induced tipping* or *B-tipping* occurs in systems with a stationary base state when the external input passes through a *dangerous* [94] bifurcation of the base state, at which point the *base state disappears or becomes unstable*, forcing the system to move to a different state. [12, 54]

(ii) *Noise-induced tipping* or *N-tipping* occurs when external *random fluctuations* drive the system too far from the base state and across some tipping

[2] In addition to these three mechanisms, *Phase-Tipping* or *P-Tipping* has recently been identified as a distinct mechanism for systems with non-stationary base states [10].

threshold [41] or *gate*, e.g. into the domain of attraction of a different state [24, 31].

(iii) *Rate-induced tipping* or *R-tipping* occurs when the external input varies either too quickly or too slowly, so the system deviates too far from the moving base state and crosses some tipping threshold [12, 112, 98, 113], e.g. into the domain of attraction of a different state. The special case of delta-kick external input is referred to as *shock-tipping* or S-tipping [39]. In contrast to B-tipping, R-tipping need not involve any bifurcations of the base state.

Mathematically speaking, B-tipping and N-tipping may be understood using classical bifurcation theory and probability theory respectively. In contrast, R-tipping is less well understood. Since R-tipping may occur in the absence of noise and away from dangerous bifurcations, modern techniques from non-autonomous dynamical systems theory are typically required for analysis.

1.3 R-tipping in a Toy Model

To illustrate R-tipping we consider the following toy model, which is a modified version of the system studied in [77, 13, 117, 91]:

$$\frac{dx}{dt} = 1 - (\lambda - x)^2 \tag{1.1}$$

$$\frac{d\lambda}{dt} = r\lambda(3 - \lambda), \tag{1.2}$$

where we consider $x(t) \in \mathbb{R}$ to be the internal state variable of the system, $\lambda(t) \in [0, 3]$ is the external input [3] and r is the "rate-parameter", the key control parameter in the study of rate-induced tipping.

We first consider the 'frozen system' where the external input $\lambda(t)$ is frozen

[3] Note that [77, 13, 117, 91] formulate a non-autonomous problem with explicitly defined $\lambda(t)$, and subsequently compactify the problem; see chapter 3.

in time. The frozen system is obtained by setting $r = 0$:

$$\frac{dx}{dt} = 1 - (\lambda - x)^2, \tag{1.3}$$

where we consider system (1.3) for different but fixed values of $\lambda \in [0, 3]$. For any such $\lambda \in [0, 3]$ the frozen system (1.3) contains a stable equilibrium $e(\lambda)$ which is the desirable 'base state', and an unstable equilibrium $e_r(\lambda)$. We write $\tilde{e}(\lambda) = (e(\lambda), \lambda)$ to represent the position of the stable equilibrium of the frozen system (1.3) in the phase space of the full system (1.1)–(1.2). Although $\tilde{e}(\lambda)$ is not a solution of system (1.1)–(1.2), since it is the stable equilibrium of the internal variable of the system it serves as a useful reference. We refer to $\tilde{e}(\lambda)$ as the 'moving base state' of system (1.1)–(1.2), and we similarly define the "moving unstable state" as $\tilde{e}_r(\lambda) = (e_r(\lambda), \lambda)$.

Having considered the equilibria of the frozen system (1.3), we now examine equilibria of the the full system (1.1)–(1.2). We first note that $\mathbb{R} \times \{0\}$ and $\mathbb{R} \times \{3\}$ are flow-invariant subspaces. These invariant subspaces contain four equilibria which we denote:

$$\tilde{e}^- = \tilde{e}(0), \quad \tilde{e}_r^- = \tilde{e}_r(0), \quad \tilde{e}^+ = \tilde{e}(3), \quad \text{and} \quad \tilde{e}_r^+ = \tilde{e}_r(3), \tag{1.4}$$

so that the moving base state $\tilde{e}(\lambda)$ moves from $\tilde{e}^-$ to $\tilde{e}^+$ as λ increases monotonically from 0 to 3. Similarly $\tilde{e}_r(\lambda)$ moves from $\tilde{e}_r^-$ to $\tilde{e}_r^+$. In system 1.1–1.2, $\tilde{e}^-$ and $\tilde{e}_r^+$ are saddles, $\tilde{e}_r^-$ is a source, while $\tilde{e}^+$ is a sink and the only attractor. To simplify the discussion of R-tipping, we focus on the behaviour of $W^{u,[r]}(\tilde{e}^-)$ [4], the unstable manifold of $\tilde{e}^-$. This allows us to understand how the system behaves if it is initialised near equilibrium for $\lambda = 0$, and λ is then increased continuously and monotonically from 0 to 3.

Figure 1.2(a) shows that for r less than some critical value r_c, $W^{u,[r]}(\tilde{e}^-)$ connects to $\tilde{e}^+$. However for larger $r > r_c$ as in figure 1.2(c), $W^{u,[r]}(\tilde{e}^-)$ diverges in the negative x direction to $-\infty$. In other words, the system tips away from the desirable base state, even though the corresponding frozen system (1.3) does not pass through any bifurcation for $\lambda \in [0, 3]$. As the transition to tipping is

[4] the superscript $[r]$ indicates that the manifold is dependent on the rate parameter r.

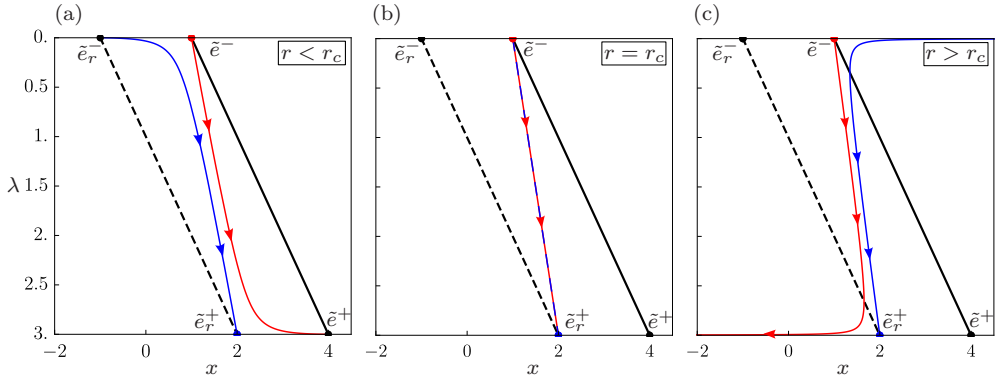


Figure 1.2: Phase portraits for system (1.1)–(1.1) showing (a) tracking for $r =< r_c$, (b) the critical rate $r = r_c$ and (c) R-tipping for $r > r_c$. The three phase portraits show the transition from tracking in (a) to R-tipping in (c) as (red) $W^{u,[r]}(\tilde{e}^-)$ crosses (blue) the R-tipping threshold $W^s(\tilde{e}_r^+)$ anchored by (blue) the R-tipping edge state $\tilde{e}_r^+$. Note that panel (b) shows the heteroclinic connection from $\tilde{e}^-$ to $\tilde{e}_r^+$ at the transition.

not due to any bifurcation, and occurs when the external variable $\lambda(t)$ changes too quickly, we say that the system R-tips.

The R-tipping instability of figure 1.2 can be explained in terms of a *global bifurcation* as follows. The boundary of the basin of attraction of $\tilde{e}^+$ is formed by $W^s(\tilde{e}_r^+) \bigcup (\mathbb{R} \times \{0\})$, the stable manifold of $\tilde{e}_r^+$ and the flow-invariant subspace for $\lambda = 0$. This means that $W^s(\tilde{e}_r^+)$ is the separatrix partitioning initial conditions in $\mathbb{R} \times (0, 3]$ of system (1.1)–(1.2) into those which limit in forward time to $\tilde{e}^+$, and those which diverge in the negative x direction to $-\infty$. When $r = r^c$, we have $\overline{W^{u,[r]}(\tilde{e}^-)} = \overline{W^s(\tilde{e}_r^+)}$ forming a heteroclinic connection from $\tilde{e}^-$ to $\tilde{e}_r^+$. At this critical rate r_c, the system neither tracks nor R-tips and instead connects to $\tilde{e}_r^+$. As $\tilde{e}_r^+$ is a regular saddle equilibrium; following [113] it is termed a *regular R-tipping edge state*. Corresondingly, as the separatrix $W^s(\tilde{e}_r^+)$ is by definition a codimension-one embedded orientable forward-invariant subset of the stable set of $\tilde{e}_r^+$, it is termed *regular R-tipping threshold*; also following [113]. R-tipping occurs then as $W^{u,[r]}(\tilde{e}^-)$ crosses the regular R-tipping threshold and for an isolated value $r = r_c$ as in figure 1.2(b), $W^{u,[r]}(\tilde{e}^-)$ connects to the R-tipping edge state, giving a heteroclinic connection from $\tilde{e}^-$ to $\tilde{e}_r^+$ along $W^s(\tilde{e}_r^+)$.

In summary, R-tipping in system (1.1)–(1.2) may be understood in terms

of passage through a heteroclinic connection to an *R-tipping edge state* along a *regular R-tipping threshold* as the rate parameter r is increased. This framework has been extended to the general case of R-tipping due to regular R-tipping thresholds in [113]. As noted in [113], not all R-tipping thresholds are regular. A particularly interesting case is that of *R-tipping quasithresholds*, which do not contain a regular R-tipping edge state. This introduces three challenges:

- As R-tipping quasithresholds do not contain regular R-tipping edge states, the framework outlined above for analysing R-tipping in terms of heteroclinic connections to such regular R-tipping edge states does not extend immediately to the case of quasithresholds.

- The lack of regular R-tipping edge states means that R-tipping quasithresholds are not given by unique trajectories which makes their definition challenging. As such R-tipping quasithresholds have not been defined to-date.

- R-tipping quasithresholds give rise to what is termed *reversible R-tipping*, where the system transitions away from its base state, possibly to some alternative *transient state*, before eventually returning to the base state. This is in contrast to what the *irreversible R-tipping* seen in this section, where there is a qualitative change in the long-term system behaviour. This means R-tipping due to crossing aquasithrehsold a quantitative rather than qualitative phenomenon, making its analysis challenging. There is an equivalence between "reversible" R-tipping and excitability, which will be explored in section 1.6.

In the current work, we give an account of the peculiar nature of reversible R-tipping due to crossing quasithresholds, uncover new types of R-tipping quasithresholds and provide a framework to analyse reversible R-tipping and pin down elusive quasithresholds. In particular, we first carefully define R-tipping quasithresholds in section 4.1, before highlighting the differences between R-tipping quasithresholds and regular R-tipping thresholds in section 4.2. Next, in sections 5 and 6 we show how R-tipping due to quasithresholds is also mediated by heteroclinic connections in a suitable reduction of the original system.

In contrast to the regular threshold of system (1.1)–(1.2), where the connection is to a regular edge state given by a regular equilibrium, in the case of a quasithreshold we will examine heterolinic connections to *singular edge states*, which only exist in the singular limit of infinite timescale separations.

1.4 Excitable Systems

The concept of excitability arose in the study of neurons, which may be triggered into an "excitable response" [37] by some external input. Excitability is a phenomological rather than mathematical concept, and as such can be difficult to define precisely. However, following [112] we can say that generally speaking, an *excitable system* is a dynamical system with three properties:

(i) *A quiescent state*, that is some attracting state which is stable under small enough perturbations, and to which the system returns after an excitable response.

(ii) An *excitability threshold*. If the system is sufficiently perturbed from the quiescent state, it will evolve away from it, giving an *excitable response*.

(iii) A *return mechanism*, which determines the character of the excitable response, and brings the system back to the quiescent state after a *refractory period*, after which the system may be excited again. This process is sometimes referred to as *relaxation*.

The study of excitable dynamical systems touches many topics of current research interest in the field of nonlinear dynamics, and we refer to [81, 42] for a more in-depth discussion of excitability. First, it follows from points (i)-(iii) that the study of excitability is often concerned with transient phenomena, where traditional bifurcation and stability theory may not be sufficient. Thus, modern techniques such as geometric singular perturbation theory (see section 1.5) are employed to explain excitable dynamics in terms of slow manifolds [68, 102, 109]. Second, excitable responses are primarily observed in systems which are subjected to some form of stimulus or external input. Such systems are inherently non-autonomous, lack compact invariant sets and so are not amenable to

many of the classical tools of nonlinear dynamics. Often, modern concepts and techniques such as *pullback attractors*, *slow manifolds* and *compactification* are required to analyse such systems [49, 109]. Third, excitability has been identified and studied in wide range of fields including: neuroscience, semiconductor lasers, cardiology, ecology, oceanography, urban geography and the dynamics of electricity markets [81, 110, 50, 111, 42, 79, 98, 99, 78, 58].

Most significant for the current work is the similarity between the study of tipping points and the study of excitable systems [112, 78]. The study of tipping points is the study of how a system evolves away from its attracting base state, while the study of excitable systems is the study of the special case where the system eventually returns to its attracting base state, possibly after visiting some alternative state. It follows then that the objects of interest in excitable systems are often the objects of interest in the study of tipping points: *quiescent / base states*, *excitability / tipping thresholds*, *excitability / tipping quasithresholds* and alternative *transient* or *metastable* states. In particular, there is an equivalence between reversible R-tipping, where the system eventually returns to its base state, and excitability.

Following [112], excitability may be divided into two types:

- *Type-A* excitability has a unique excitability threshold given by the unstable manifold of some unstable state, and the transition from no response to an excitable response is discontinuous.

- *Type-B* excitability has no unique excitability threshold, rather it occurs as the system crosses a continuous excitability *quasithreshold*. The transition from no response to an excitable response as in figure 1.4 is *abrupt but continuous*.

In short, a unique excitability threshold may be identified in type-A excitability, while type-B excitability occurs due to a non-unique *quasithreshold*. Such quasithresholds arise due to a timescale separation [112, 68]. That is, the model variables evolve on distinct timescales. As reversible R-tipping and excitability are equivalent, we can divide reversible R-tipping into two types in the same manner. Reversible R-tipping may occur due to:

- *Crossing a regular threshold*: where there is unique regular R-tipping threshold given by the stable manifold of a regular R-tipping edge state, and the transition from tracking to R-tipping is discontinuous; see canonical examples II, IV, and VI in [117].

- *Crossing a quasithreshold*: where there is no unique regular R-tipping threshold, rather R-tipping occurs as the system crosses a R-tipping *quasithreshold*. The transition from tracking to R-tipping is *abrupt but continuous*; see canonical example V in [117] and chapters 5 and 6 of the current work.

In the current work we study a soil-carbon model with timescale separation, which undergoes reversible R-tipping due to crossing a quasithreshold to a metastable state. The type of R-tipping quasithreshold depends on the timescale, magnitude and shape of the external input. The following section discusses the theory of systems containing a timescale separation, referred to as fast-slow dynamical systems.

1.5 Fast-Slow Dynamical Systems

In this section, we review elements of the study of fast-slow systems and geometric singular perturbation theory that are relevant for this work. We refer to [43, 55, 109] for a more in-depth review. Generally speaking, a fast-slow dynamical system is a system of ordinary differential equations that can be written in the form [5]:

$$\epsilon \frac{dx}{dt} = f(x, y, \epsilon) \tag{1.5}$$

$$\frac{dy}{dt} = g(x, y, \epsilon), \tag{1.6}$$

where $x \in \mathbb{R}^n$, $y \in \mathbb{R}^m$, $f : \mathbb{R}^{n\times m} \to \mathbb{R}^n$, $g : \mathbb{R}^{n\times m} \to \mathbb{R}^m$ and $0 < \epsilon \ll 1$. The *small parameter* ϵ both indicates the presence of, and quantifies, the timescale

[5] We note that much work has been done recently on a coordinate-independent theory of fast-slow systems, where the timescale splitting may not be explicit [108]

separation between the x variables and the y variables. The x variables are referred to as the *fast variables* while the y variables are referred to as the *slow variables*. We refer to system (1.5)-(1.6) as an *n-fast m-slow* system.

System (1.5)-(1.6) is referred to as the *slow form*, and may be written in the flow-equivalent *fast form* using the time rescaling $\tau = t/\epsilon$ [6]:

$$\frac{dx}{d\tau} = f(x, y, \epsilon) \tag{1.7}$$

$$\frac{dy}{d\tau} = \epsilon g(x, y, \epsilon), \tag{1.8}$$

where we refer to τ as the *fast time*, and t as the corresponding *slow time*. System (1.7)-(1.8) makes the timescale separation more apparent in that it is clear that the y component of the vector field defined by system (1.7)-(1.8) will in general be small relative to the x component. Thus, the slow y variables will tend to evolve "more slowly" than the fast x variables except, perhaps, when $f(x, y, \epsilon) \approx 0$.

The timescale separation of fast-slow systems may be exploited to gain insight into their dynamics. The strategy is to notice that system (1.5)–(1.6) (or equivalently system (1.7)–(1.8)) may be treated as a perturbation problem in the small parameter ϵ. As each system is qualitatively different in the limit $\epsilon \to 0$, the perturbation problem is *singular*. We proceed with system (1.5)–(1.6) and take the limit $\epsilon \to 0$ to obtain the *reduced problem*:

$$0 = f(x, y, 0) \tag{1.9}$$

$$\frac{dy}{dt} = g(x, y, 0), \tag{1.10}$$

which we may also refer to as the *slow subsystem*, and we refer to the flow defined by system (1.9)–(1.10) as the *slow flow*. From a mathematical standpoint, the only set where the vector field associated to (1.5)–(1.6) remains well defined in

[6] The symbol τ is often used to denote the slow time, however as the base time t in the problem at hand is slow, we use it to denote the fast time.

the limit $\epsilon \to 0$ of is the set:

$$S := \{(x, y) \,:\, f(x, y, 0) = 0\}, \tag{1.11}$$

which is referred to as the *critical manifold*. From an intuitive standpoint, smaller ϵ represents a greater timescale separation between the fast and slow variables. In the reduced problem we deal with the limiting case where the timescales are separated completely, and the fast variables have gone to equilibrium on the set S. Only when the fast variables have gone to equilibrium do we then consider the motion of the slow variables. In other words, the reduced problem is an approximation of the slow dynamics along the manifold of equilibria of the fast variables.

The next step is to approximate the fast dynamics away from the critical manifold. If we examine system (1.7)–(1.8) which is in the fast time τ, we can take the limit $\epsilon \to 0$ to obtain the *layer problem*:

$$\frac{dx}{d\tau} = f(x, y, 0) \tag{1.12}$$

$$\frac{dy}{d\tau} = 0, \tag{1.13}$$

which we may also refer to as the *fast subsystem*, and we refer to the flow defined by system (1.12)–(1.13) as the *fast flow*. The vector field defined by system (1.12)–(1.13) is a close approximation of the vector field defined by system (1.7)–(1.8). Intuitively, away from the critical manifold S the fast variables dominate the dynamics and the slow variables may be disregarded as a first approximation in the sense that the slow variables remain constant-in-time. The points of S are equilibria of the layer problem (1.12)–(1.13) for different values of the slow variables. This allows us to classify the points of S by their stability type as equilibria of system (1.12)–(1.13).

We can use the layer problem (1.12)–(1.13) to approximate the dynamics of (1.7)–(1.8) away from S, and the reduced problem to approximate the dynamics near S. However, the great success of geometric singular perturbation theory is that the connection between dynamics in singular limit $\epsilon \to 0$ and the

full dynamics for $0 < \epsilon \ll 1$ may be made stronger through application of the *Fenichel Theorems*. We provide the relevant parts of Fenichel's first and second theorems and refer to [55] for a more in-depth review.

We first define the notion of normal-hyperbolicity, which is a key regularity assumption underpinning much of the theory:

Definition 1.5.1. Let M be a critical manifold as defined above. A subset $S \subset M$ is called *normally hyperbolic* if the $n \times n$ Jacobian matrix $(D_x f)(p, 0)$ of first partial derivatives with respect to the fast variables has no eigenvalues with zero real part for all $p \in S$.

We are now ready to state the first and second Fenichel Theorems:

Theorem 1.5.1 (Fenichel's First Theorem)**.** Let M be a critical manifold as defined above. Suppose S is a compact normally hyperbolic submanifold (possibly with boundary) of the critical manifold $S \subset M$, and $f, g \in C^r$ $(r < \infty)$. Then for $\epsilon > 0$ sufficiently small, the following hold:

(F1) There exists a *locally invariant*, C^r smooth, normally hyperbolic manifold S_ϵ which is diffeomorphic to S.

(F2) S_ϵ has the same stability properties with respect to the fast variables as S.

(F3) The flow on S_ϵ converges to the slow flow as $\epsilon \to 0$.

In summary, given a normally hyperbolic critical submanifold S in the singular limit $\epsilon \to 0$ and a slow flow defined by a reduced problem as in (1.9)–(1.10), the first Fenichel Theorem guarantees the existence of a *slow manifold* S_ϵ for $0 < \epsilon \ll 1$ with the same stability properties, and the flow along S_ϵ is well approximated by the slow flow of the reduced problem (1.9)–(1.10).

Theorem 1.5.2 (Fenichel's Second Theorem)**.** As points of S are equilibria of the layer problem (1.12)–(1.13), each point has local stable and unstable manifolds. Let the collection all such stable manifolds be written $W^s_{loc}(S)$ and the collection of all such unstable manifolds be written $W^u_{loc}(S)$. We refer to $W^s_{loc}(S)$ and $W^u_{loc}(S)$ as the stable and unstable manifolds of S respectively. Then for $\epsilon > 0$ sufficiently small, the following hold:

(F4) There exist *locally invariant*, C^r smooth, normally hyperbolic manifolds $W^s_{loc}(S_\epsilon)$ and $W^u_{loc}(S_\epsilon)$ which are diffeomorphic to $W^s_{loc}(S)$ and $W^u_{loc}(S)$ respectively.

(F5) $W^s_{loc}(S_\epsilon)$ and $W^u_{loc}(S_\epsilon)$ have the same stability properties with respect to the fast variables as $W^s_{loc}(S)$ and $W^u_{loc}(S)$.

(F6) The flow on $W^s_{loc}(S_\epsilon)$ and $W^u_{loc}(S_\epsilon)$ converges to the fast flow as $\epsilon \to 0$.

We refer to $W^s_{loc}(S_\epsilon)$ and $W^u_{loc}(S_\epsilon)$ as stable and unstable *fast manifolds* respectively. Given a stable manifold $W^s_{loc}(S)$ or unstable manifold $W^u_{loc}(S)$ of a critical manifold S in the layer problem (1.12)–(1.13), the second Fenichel theorem guarantees the existence of a stable fast manifold $W^s_{loc}(S_\epsilon)$ or unstable fast manifold $W^u_{loc}(S_\epsilon)$ for $0 < \epsilon \ll 1$ with the flow along the fast manifold well approximated by the flow of the layer problem (1.12)–(1.13). In essence, the first and second Fenichel theorems make equivalent statements about the existence of, and the dynamics along, slow manifolds and fast manifolds respectively.

The first and second Fenichel theorems give a near complete picture of how the layer problem (1.12)–(1.13) and the reduced problem (1.9)–(1.10) together, may be related to the original, singularly perturbed problem (1.5)–(1.6). The theory breaks down close to non-hyperbolic *folds* denoted F, which are subsets of S consisting of non-hyperbolic equilibria of the layer problem (1.12)–(1.13) separating attracting and repelling branches of the critical manifold (1.11). Solutions of the reduced problem (1.9)–(1.10) which reach non-hyperbolic folds typically blow up, that is reach infinity in finite time. As such, folds mediate transitions from slow dynamics to fast dynamics. The extension of geometric singular perturbation theory to non-hyperbolic folds is non-trivial, and research is ongoing in this area [92, 106, 51, 52]. Dynamics close to non-hyperbolic folds will be central to this work, and we will further discuss these dynamics and the relevant recent results in sections 4.1 and 5 as required.

1.6 Excitability Quasithresholds: Fitzhugh-Nagumo

The classical example of quasithresholds in a fast-slow dynamical system is the Fitzhugh-Nagumo model, which is a two-dimensional simplification of the Hodgkin-Huxley model of spike generation in squid giant axons. The model was originally formulated as a modified version of the Van der Pol model to isolate the mathematical phenomenon of excitability as identified in the more complex Hodgkin Huxley model. Consequently, this model is also the classical example of an *excitable system*, with Fitzhugh being the first to classify types of excitability [37]. The equations of the Fitzhugh-Nagumo model as considered by Fitzhugh may be written as a fast slow dynamical system as follows:

$$\frac{dv}{d\tau} = v - \frac{v^3}{3} - w + I \tag{1.14}$$

$$\frac{dw}{d\tau} = -\epsilon(v + a - bw), \tag{1.15}$$

where v is the membrane potential, w is the recovery variable and I is the magnitude of the stimulus current. For the parameter values $a = 5/6$, $b = 1$ and $I = I^- = 0$, the system has a single, globally asymptotically stable equilibrium $e(I^-)$. In excitability terms, $e(I)$ is the quiescent state. Fitzhugh studied how system (1.14)–(1.15) initialised at $e(I^-)$ responded to a subsequent instantaneous switch in I to $I^+ > I^-$. This is equivalent to setting $I = I^+$ in system (1.14)–(1.15), and examining the solution initialised at $e(I^-)$.

For I^+ small enough, the system converges to the new equilibrium $e(I^+)$. However, for I^+ large enough, despite not crossing any bifurcation the system undergoes an excitable response as shown in figure 1.3(a). Specifically, it undergoes a fast excursion in the positive v direction, stabilises for a time at some transient state, before undergoing a fast relaxation and return to equilibrium $e(I^+)$. Perhaps more significantly, the system transition from 'no response' to 'excitable response' is not discontinuous, rather it is *abrupt but continuous* [7] in I^+ as shown in figure 1.3(b).

As the only equilibrium of the system $e(I^+)$ remains stable, bifurcation the-

[7] Sometimes referred to as an 'apparent' discontinuity

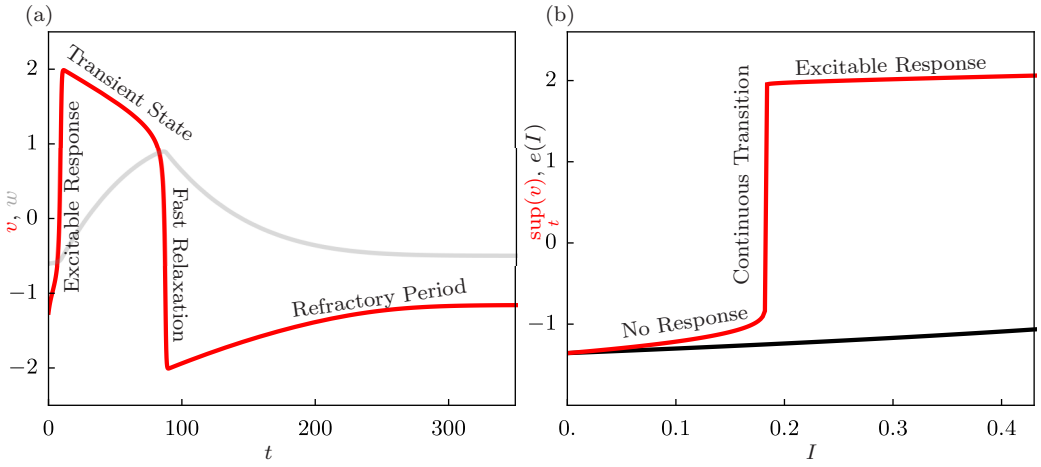


Figure 1.3: (a) The time trace of different stages of the excitable response of (red) v. (b) The maximum value of v, (red) $\sup_t(v)$ together with (black) $v^e(I)$ against the magnitude of the switch in I, represented by I^+. The transition from no response to and excitable response is abrupt but continuous.

ory gives no insight into the excitable response. However, the Fitzhugh Nagumo model as given in (1.14)–(1.15) is a fast-slow system, and we may use the techniques of geometric singular perturbation theory outlined in section 1.5 to understand the nature of the observed excitable response.

System (1.14)–(1.15) has 1 fast variable v which evolves on the fast time τ, and 1 slow variable w which evolves on the slow time $t = \epsilon\tau$. Consequently, system (1.14)–(1.15) is a 1-fast 1-slow system. We take the limit $\epsilon \to 0$ of system (1.14)–(1.15). As τ is the fast time, this gives the layer problem:

$$\frac{dv}{d\tau} = v - \frac{v^3}{3} - w + I \tag{1.16}$$

$$\frac{dw}{d\tau} = 0, \tag{1.17}$$

the dynamics of which are in the horizontal v direction and are shown in Figure 1.4 as double arrows.

We may convert system (1.14)–(1.15) to the slow time by the substitution

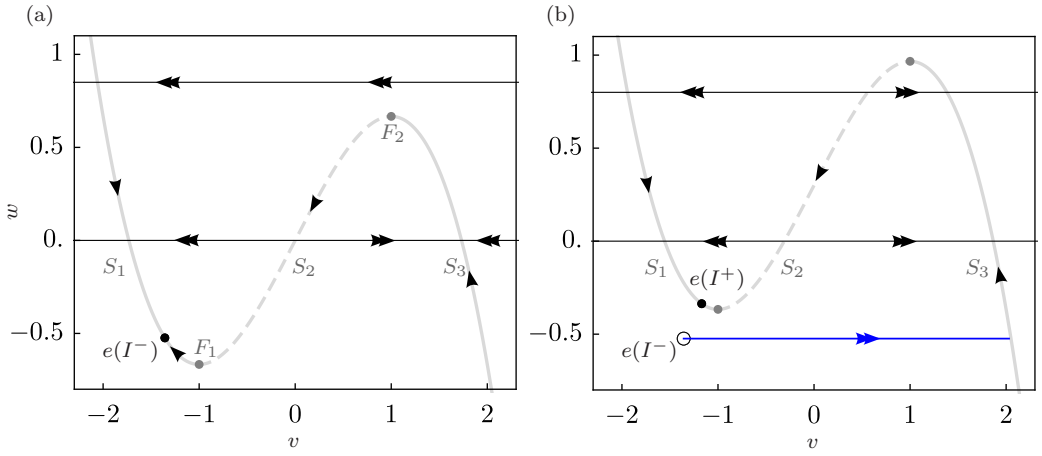


Figure 1.4: The critical manifold $S(I)$ with (solid grey) two normally hyperbolic attracting branches, $S_1(I)$ and $S_3(I)$, and (dashed grey) a normally hyperbolic repelling branch $S_2(I)$, for system (1.14)–(1.15) with $\epsilon = 0$, together with (single arrows) the slow dynamics of the reduced problem (1.20)–(1.21) along $S(I)$ in the slow time t, and (double arrows) the fast dynamics of the layer problem (1.16)–(1.17) in the fast time τ for different values of w. These are shown for (a) $I = I^- = 0$ and (b) $I = I^+ = 0.3$ where (blue) the trajectory initialised at (white circle) $e(I^-)$ in the layer problem (1.16)–(1.17) is also shown.

$t = \epsilon\tau$, giving:

$$\epsilon\frac{dv}{dt} = v - \frac{v^3}{3} - w + I \tag{1.18}$$

$$\frac{dw}{dt} = v + a - bw, \tag{1.19}$$

the dynamics of which are equivalent to those of system (1.14)–(1.15), in the sense that they define the same flow. If we take the limit $\epsilon \to 0$ of system (1.18)–(1.19) we obtain the reduced problem:

$$0 = v - \frac{v^3}{3} - w + I \tag{1.20}$$

$$\frac{dw}{dt} = v + a - bw, \tag{1.21}$$

whose dynamics are restricted to the critical manifold:

$$S(I) := \left\{ (v, w) \,:\, w = v - \frac{v^3}{3} + I \right\}. \tag{1.22}$$

We classify the points of S by examining their stability in the layer problem (1.16)– (1.17). Specifically, $S(I)$ has two normally hyperbolic attracting branches, denoted $S_1(I)$ and $S_3(I)$, which are separated from a normally hyperbolic repelling branch $S_2(I)$ by two non-hyperbolic fold points, denoted $F_1(I)$ and $F_2(I)$. In other words, the critical manifold can be partitioned as follows

$$S(I) = S_1(I) \cup F_1(I) \cup S_2(I) \cup F_2(I) \cup S_3(I).$$

The attracting branch $S_1(I)$ contains the quiescent state $e(I)$. The other attracting branch, $S_3(I)$, is the transient state that the system reaches following an excitable response. Figure 1.4 shows the branches of S in grey, and the reduced dynamics along S as single arrows.

Figure 1.4(a) shows the reduced and layer problems together with S in the (v, w) phase plane for $I = I^- = 0$. Figure 1.4(b) shows the same for $I = I^+ > I^-$, and illustrates how the critical manifold S shifts upwards relative to $e(I^-)$. Specifically, if I^+ is larger than some critical value I^{inst}, then $e(I^-)$ will lie on a trajectory of the layer problem where the flow is directed toward the transient state S_3; shown in blue in figure 1.4(b). This illustrates how an excitable response occurs for $0 < \epsilon \ll 1$ and $I^+ > I^{inst}$ large enough.

As I is increased across the range $[0, I^+]$ where $I^+ > I^{inst}$, when $\epsilon = 0$ the transition to an excitable response occurs discontinuously as I crosses I^{inst}. However, for $0 < \epsilon \ll 1$ the transition to an excitable response is *abrupt but continuous*; see figure 1.3(b). This is characteristic of crossing an *excitability quasithreshold*. The excitability quasithreshold in this model was explored in detail by Fitzhugh [97], and is a separatrix formed by a continuum of trajectories in (v, w) phase space which separate initial conditions which give an excitable response, from those which do not. This quasithreshold can be related to S_2, the repelling branch of the critical manifold.

We have shown how timescale separation may give rise to excitable dynamics,

and geometric singular perturbation theory provides the tools for understanding the mechanisms governing those dynamics. In section 4.1 we precisely define a quasithreshold, and in section 4.4 we study an instantaneous switch in external conditions, both in the context of R-tipping. In each case, we use geometric singular perturbation theory in a similar manner to the present section.

1.7 Background Summary and Thesis Structure

So far, we have discussed Arctic peatlands, tipping points, excitable systems, and fast-slow dynamical systems. We have also shown that geometric singular perturbation theory may be used to uncover the dynamical mechanism responsible for excitability in the Fitzhugh-Nagumo model, which is a fast-slow dynamical system. In the remainder of this thesis, we will examine reversible Rate-induced tipping in a soil-carbon model which has a similar fast-slow structure. The reversible R-tipping is due to crossing a quasithreshold, and is equivalent to type-B excitability as discussed in section 1.4 in the following sense. The soil carbon model can be made to transition from its desirable base state, to an alternative, undesirable, *metastable* state which is analagous to the transient state of figure 1.3. This transition occurs abruptly and continuously as the system is pushed across an R-tipping *quasithreshold* by a changing external input. Since the resulting metastable state is transient, and the system returns to its attracting base state in the infinite time limit in the same manner as an excitable system. However, although the system eventually recovers its carbon, the amount of carbon released and the time spent in the metastable state and refractory period are significant from a human standpoint as, to the best of our knowledge, human beings are themselves finite time phenomena. Clearly, understanding reversible R-tipping is important, even when the dynamics are "transient". This is the motivation for this thesis, which aims to do so by synthesising ideas from the theory of tipping points, excitability theory and fast-slow dynamical systems.

This thesis is organised in three parts. In the first, mathematical modelling

part of the thesis (Chapter 2), we:

- Modify the conceptual soil-carbon model introduced by Luke and Cox [60] with a more realistic microbial soil respiration function.
- Show that the modified conceptual model has a new *alternative hot metastable state* and reproduces the key features of the medium-complexity model from [45, Fig.4(a)].
- Demonstrate R-tipping to the hot metastable state for realistic climate change scenarios including global warming and summer heatwaves.
- Based on the above, propose an explanation for "Zombie fires" in peatlands [3, 88, 65, 100] that disappear from the surface, smoulder underground during the winter, and "come back to life" in the spring.

In the second, mathematical analysis part of the thesis (Chapters 3–6), we identify non-obvious dynamical mechanisms that are responsible for the R-tipping instability to the hot metastable state. The main obstacles to analysis of this instability are twofold: the soil-carbon model is a non-autonomous dynamical system, so it does not have any equilibria or compact invariant sets, and the R-tipping is due to crossing an elusive quasithreshold in the phase space [97, 112, 68, 76, 98, 99, 44, 11]. To overcome these obstacles we combine three different strategies. Firstly, we consider external inputs that decay to a constant at infinity. Secondly, we compactify the problem to include the equilibrium base states for the autonomous limit systems from infinity [114]. These two strategies alone work for R-tipping due to crossing regular thresholds since these thresholds are anchored at infinity by compact invariant sets called *regular edge states* [113]. However, quasithresholds do not contain such edge states [113, Sec.8(d)]. Therefore, thirdly, we build on [112, 76], take advantage of large timescale separation in the compactified soil-carbon model and apply concepts from geometric singular perturbation theory [36, 43, 109, 55]. Specifically, we:

- Define R-tipping due to crossing a quasithreshold in terms of *slow manifolds* and *canard trajectories* [109] in the autonomous compactified system.

- Identify *singular edge states*: special points called *folded singularities* [92] that arise in the slow (reduced) system, and new saddle equilibria that arise in the fast (layer) system.

- Reduce an R-tipping problem due to crossing a quasithreshold to a heteroclinic orbit connecting the base state for the past limit system to a singular edge state. We use this reduction to identify four different cases of R-tipping as follows:

  - For global warming, we identify three (slow) cases of R-tipping via unfolding of a codimension-two *heteroclinic folded saddle-node type-I singularity* that arises in the reduced system.

  - For a summer heatwave, we identify a fourth (fast) case of R-tipping via analysis of a codimension-one *heteroclinic orbit* connecting the base state for the past limit system to a new saddle equilibrium that arises in the layer system.

- Show that a quasithreshold gives rise to *critical ranges of rate of change* of the external input rather than isolated critical rates. We reveal new types of quasithresholds by relating a family of canard trajectories associated with a singular edge state to a quasithreshold.

In the third, numerical analysis part of the thesis (Chapter 7), we review some of the numerical methods employed throughout the rest of the thesis. Some of the methods and numerical problems are particular to fast-slow dynamical systems, or to compactified nonautonomous problems. In particular we:

- Numerically study the compactified system in an efficient manner.

- Numerically determine the behaviour of a solution of interest; tracking, R-tipping, canard with or without head, secondary or composite canard.

- Compute attracting and repelling slow manifolds together with maximal canards which cross via their intersections, following the methods outlined in [28, 30].

Finally, in chapter 8 we summarise, and give an outlook for possible future directions in which this work could be extended. The material throughout this thesis, with the exception of Chapter 7, is based on a paper that is currently being revised for Proceedings of the Royal Society A: Eoin O'Sullivan, Kieran Mulchrone and Sebastian Wieczorek. Rate-Induced Tipping to Metastable Zombie Fires.

Chapter 2

The Nonautonomous Soil-Carbon Model

2.1 The Model Equations

The starting point of our analysis is a discussion of the soil-carbon model introduced by Luke and Cox [60]. This model describes the time evolution of the soil temperature T and soil carbon concentration C in peat soils:

$$\mu \frac{dT}{dt} = -\lambda(T - T_a(rt)) + A\,C\,R_s(T), \tag{2.1}$$

$$\frac{dC}{dt} = \Pi - C\,R_s(T). \tag{2.2}$$

The model incorporates three soil processes and one time-varying external input. The first process describes equilibration of the soil temperature T with atmospheric temperature T_a according to Newton's Law of Cooling [62], at a rate that depends on the soil-to-atmosphere heat transfer coefficient λ and the specific heat capacity of the soil μ. The second process describes a linear increase in the soil carbon concentration C over time at a rate Π, due to carbon generated from decaying plant litter and other processes referred to as "Gross Primary Production" [86].[1] The third and only nonlinear process in the model describes temperature-sensitive microbial activity in the soil in terms of the soil

[1]Note that dC/dt is the "Net Primary Production" in the model.

respiration function $R_s(T)$. This process couples the dynamics of T and C, and is discussed in detail in section 2.3. Atmospheric temperature $T_a(rt)$ is a time-varying external input, which represents weather anomalies or climate variation. The *rate parameter* $r > 0$ quantifies the time scale of climatic variability and is the key *input parameter* in the model. An important aspect of our study is that we use realistic values of the soil parameters based on [60], which are given in Table C.1 in the Appendix, a realistic soil respiration function $R_s(T)$ introduced in section 2.12.3, and realistic climate-change scenarios $T_a(rt)$ based on real weather data from Cherskii in Siberia [2]; see the blue arrow in Fig. 1.1.

To facilitate analysis, we introduce a *small parameter* $\epsilon = \mu/A \ll 1$ $\mathrm{Kg\,m^{-2}\,{}^{\circ}C^{-1}}$ [2] and rewrite the soil-carbon model (2.1)–(2.2) as a fast-slow nonautonomous dynamical system [112]:

$$\epsilon \frac{dT}{dt} = f_1(T, C, T_a(rt)) := -\frac{\lambda}{A}(T - T_a(rt)) + C\,R_s(T), \tag{2.3}$$

$$\frac{dC}{dt} = f_2(T, C) \qquad := \Pi - C\,R_s(T), \tag{2.4}$$

where we define f_1 and f_2 for convenience. Note that system (2.1)–(2.2) or (2.3)–(2.4) does not have any equilibria (stationary solutions) owing to the time-varying external input $T_a(rt)$.

2.2 Soil-to-Atmosphere Heat Transfer

Following Luke and Cox [60], we assume the soil is covered by an insulating layer of moss which is typical in northern-latitude peat soils, where the peat itself is often formed by semi-decomposed sphagnum moss [116, 16]. This is a commonly made assumption when modelling northern-latitude peat soils [46]. It follows that the the soil-to-atmosphere-heat transfer coefficient λ is a function of λ_{soil}, the heat transfer coefficient of the soil, and λ_{moss} the heat transfer coefficient of

[2] For ease of exposition, we omit the units of ϵ for the remainder of this work, with the understanding that it has units of $\mathrm{Kg\,m^{-2}\,{}^{\circ}C^{-1}}$.

the moss:

$$\lambda = \frac{\lambda_{soil}\lambda_{moss}}{\lambda_{soil} + \lambda_{moss}}. \tag{2.5}$$

For a soil of depth dz, λ_{soil} is related to soil thermal conductivity κ_{soil} in [60] by:

$$\lambda_{soil} = \frac{\kappa_{soil}}{0.5dz}, \tag{2.6}$$

where κ_{soil} is the thermal conductivity of soil. The heat transfer coefficient of the moss layer λ_{moss} may be related to its thermal conductivity κ_{moss} in the same manner. Soil thermal conductivity in turn may be expressed function of soil volumetric water content θ_s and soil porosity θ_{sat} by the following relationship:

$$\kappa_{soil}(\theta_s) = \kappa_{solids}^{1-\theta_{sat}} \kappa_{air}^{\theta_{sat}} \left(\frac{\kappa_{water}}{\kappa_{air}}\right)^{\theta_s}. \tag{2.7}$$

Here, $\kappa_{solids}, \kappa_{air}$ and κ_{water} are the thermal conductivities of soil solids, air and water respectively while θ_{sat} is the soil porosity and $\theta_s \in [0, \theta_{sat}]$. Following [60, 16], we choose a soil porosity of $\theta_{sat} = 0.7$. The thermal conductivity of the moss layer κ_{moss} may be similarly expressed in terms of its water content θ_m by setting $\theta_{sat} = 0.9$ [16]. High porosity is a well documented quality of sphagnum moss [116, 105, 16], meaning that a drier layer of sphagnum moss acts as an insulating layer on top of the soil. Representative values of the conductivities are $\kappa_{solids} = 0.25\,\mathrm{W\,m^{-1}\,{}^\circ C^{-1}}$, $\kappa_{air} = 0.025\,\mathrm{W\,m^{-1}\,{}^\circ C^{-1}}$ and $\kappa_{water} = 0.573\,\mathrm{W\,m^{-1}\,{}^\circ C^{-1}}$ [80].

For this work, we fix $\lambda = 5.049 \times 10^6\,\mathrm{J\,y^{-1}\,m^{-2}\,{}^\circ C^{-1}}$ which in SI units is approximately $\lambda \approx 0.16\,\mathrm{W\,m^{-2}\,{}^\circ C^{-1}}$. Using equation 2.5, this corresponds to, for example, a soil of depth 1 m with soil moisture $\theta_s \approx 0.2502$, and a dry moss layer of depth 0.1 m so that $\theta_m = 0$. For the influence of varying λ on the model, see section 4.8.

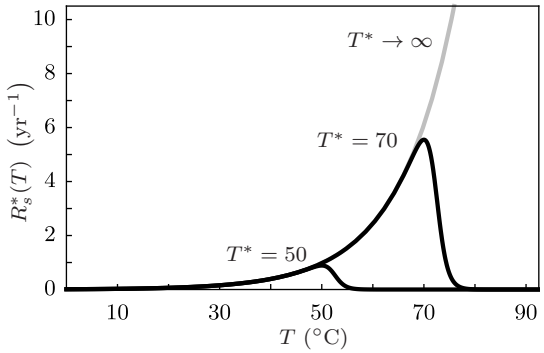


Figure 2.1: (Black) The modified non-monotone microbial soil respiration function $R_s^*(T)$ in (2.11) with $c = 10$ and the die-off temperature $T^* = 50$ and 70. (Grey) In the limit $T^* \to \infty$, we recover the unmodified monotone microbial soil respiration function $R_s^\dagger(T)$ in (2.10). See Table C.1 for other parameter values.

2.3 Modified Microbial Respiration

Microbial respiration is the key nonlinearity coupling soil carbon C and temperature T which underpins this study. The rate at which soil carbon is consumed due to microbial respiration is dependent on both the soil carbon C, and the soil temperature T [3]:

$$\frac{dC}{dt} \sim C\, R_s(T). \tag{2.8}$$

As $R_s(T)$ is simply a rate, it has units of yr^{-1}. Vertically integrated soil carbon C has units kg m^{-2} so that (2.8) has units kg $\mathrm{m}^{-2}t^{-1}$.

Microbial respiration is an exothermic reaction, and so warms the soil at a rate which is dependent on the specific heat of the reaction A and the specific heat capacity of peat soil μ:

$$\frac{dT}{dt} \sim \frac{A}{\mu}\, C\, R_s(T). \tag{2.9}$$

As detailed in table C.1, the term A/μ has units $^\circ\mathrm{C}\,\mathrm{kg}^{-1}\,\mathrm{m}^2$ so that 2.9 has units $^\circ C\,\mathrm{yr}^{-1}$

[3] Microbial respiration also depends soil moisture θ_s, however we do not consider this dependence in this study.

Our contribution to the model introduced by Luke and Cox is a modification of the microbial soil respiration function from [60]. At low to moderate soil temperatures, the temperature dependent component of microbial soil respiration can be described by a Q_{10} exponential function [48]:

$$R_s^\dagger(T) = R_s(0)\, e^{\alpha T} \quad \text{with} \quad \alpha = \ln(Q_{10})/10, \tag{2.10}$$

where the dimensionless, soil-specific parameter Q_{10} may be estimated from experimental data [48]. While the monotone $R_s^\dagger(T)$ in (2.10) captures the trigger mechanism for the R-tipping instability, it becomes unrealistic at high T. Specifically, T quickly increases to unrealistically high levels due to microbial soil respiration alone, [60, 112]. To address this issue, we account for an important limitation, that is, soil microbes die above some *die-off temperature* $T = T^*$. Specifically, we construct a modified non-monotone microbial soil respiration function

$$R_s^*(T) = R_s(0)\, \frac{e^{\alpha b} + e^{-c\alpha b}}{e^{-\alpha(T-b)} + e^{c\alpha(T-b)}} \quad \text{with} \quad b = T^* + \frac{\ln c}{\alpha + c\alpha}, \tag{2.11}$$

that agrees with the Q_{10} exponential growth (2.10) for $T < T^*$, has a maximum at $T = b \approx T^*$, and decays exponentially for $T > T^*$; see figure 2.1. Such $R_s^*(T)$ prevents soil temperature T from reaching unrealistically high levels. Note that this construction introduces two additional parameters, namely the die-off temperature T^*, and the ratio c of the exponential decay rate for $T > T^*$ and exponential growth rate α for $T < T^*$. In the remainder of the thesis, we use

$$R_s(T) = R_s^*(T).$$

2.4 The Autonomous Frozen System and the Moving Equilibrium

To gain insight into the tipping mechanisms in the nonautonomous system (2.3)–(2.4), or equivalently system (2.1)–(2.2), we set $r = 0$ and consider the resulting

autonomous *frozen system* for different but fixed-in-time values of the atmospheric temperature T_a. The frozen system has just one equilibrium

$$e(T_a) = (T^e(T_a), C^e(T_a)) = \left(T_a + \frac{A\Pi}{\lambda}, \frac{\Pi}{R_s(T_a + \frac{A\Pi}{\lambda})} \right), \tag{2.12}$$

which is the "base state" described in the introduction. Although the position of $e(T_a)$ in the phase plane (T, C) changes with T_a, the equilibrium remains linearly stable (hyperbolic) and globally attractive[4] within the realistic range of the soil parameters and T_a used in our study. Thus, we can exclude the possibility of B-tipping from $e(T_a)$ [12].

To discuss R-tipping, we consider the stable equilibrium of the frozen system parameterised by time t for a given input $T_a = T_a(rt)$, which we denote

$$e(T_a(rt)), \tag{2.13}$$

and refer to as the *moving stable equilibrium* [72, 113].[5]. The moving stable equilibrium is not a solution to the nonautonomous system (2.3)–(2.4). However, it can serve as a useful reference. We follow the approach of [13, 72, 113] and relate solutions of the nonautonomous system (2.3)–(2.4) to $e(T_a(rt))$ for different rates $r > 0$. For small r, solutions to (2.3)–(2.4) started near $e(T_a(rt))$ are guaranteed to stay near or track $e(T_a(rt))$ [113, Th.7.1]. However, a nonautonomous R-tipping instability in the form of a large departure from $e(T_a(rt))$ to an alternative *transient state* for a finite period of time may appear for larger r; see [60, 112, 26]. In the next section we give an intuitive explanation of this instability and propose it as a main cause of recently observed Zombie fires in peatlands [3, 88, 65, 100] and, possibly, compost fires [21, 70].

[4]Meaning that $e(T_a)$ attracts all initial conditions.

[5]Note that $e(T_a(rt))$ is also referred to as a "quasistatic equilibrium" or an "instantaneous equilibrium" [13].

2.5 R-tipping to a Hot Metastable State and Zombie Fires

The nonlinear process of microbial soil respiration gives rise to a *vicious cycle* that underpins R-tipping and can be understood in terms of *thermal runaway* [115] as follows. As soil microbes release carbon from the soil into the atmosphere via organic matter decomposition, they generate heat. Typically, the cooler atmosphere allows the soil to achieve a balance between heat and carbon, which is represented by the moving stable equilibrium $e(T_a(rt))$. However, this balance may be disturbed if the atmosphere warms up too fast. The faster the atmosphere warms up, the faster the soil warms up, and the quicker the increase in microbial activity, allowing soil temperature T to reach a level where it can no longer be equilibrated by the cooler atmosphere. This further accelerates microbial activity, which in turn speeds up the growth of T and the release of soil carbon C into the atmosphere. Once the soil carbon burns out, the soil temperature drops suddenly and carbon starts accumulating again. Hence, despite having a linearly stable and globally attractive equilibrium $e(T_a)$ for any fixed value of the atmospheric temperature T_a, the system is very sensitive to how fast the atmospheric temperature T_a increases over time. In other words, the system may evolve away from the moving stable equilibrium $e(T_a(rt))$ and visit an alternative transient state for a finite period of time if $T_a(rt)$ rises too fast.

We now demonstrate that the soil respiration function $R_s^*(T)$ introduced in section 2.1 gives rise to a new alternative transient state at high T that could explain smouldering "Zombie fires" [3]. This is evidenced by two remarkable results of the soil-carbon model (2.3)–(2.4) with realistic soil parameters, realistic microbial soil respiration function $R_s(T) = R_s^*(T)$, and different climate-change scenarios $T_a(rt)$ based on real weather data from Cherskii in Siberia [2].

(a) *R-tipping to a hot metastable state.* The more realistic $R_s(T) = R_s^*(T)$ in (2.3)–(2.4) breaks the vicious cycle (or thermal runaway) giving rise to a hot metastable state at high soil temperatures $T \approx T^*$. This state is reminiscent of "Zombie fires" observed in tropical and arctic peat-

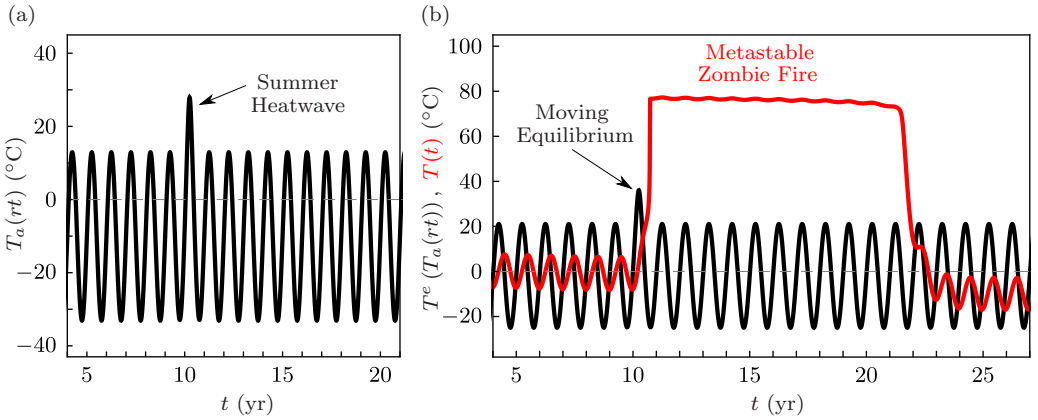


Figure 2.2: (a) Realistic seasonal variations of atmospheric temperature $T_a(rt)$ with a summer heatwave in year 10, based on observations at Cherskii in Northern Siberia [2]; see (A.2) for details of $T_a(rt)$. (b) Time evolution of (black) moving equilibrium soil temperature $T^e(T_a(rt))$ from (2.12) and (red) the actual soil temperature $T(t)$ obtained by solving (2.3)–(2.4) in response to the external input $T_a(rt)$ from panel (a). Initial soil temperature is $T(0) = -10°\text{C}$. Initial soil carbon is $C(0) = 120\,\text{kg}\,\text{m}^{-2}$, which corresponds to $\approx 3.64\,\text{m}$ soil depth assuming a volumetric carbon density of $33\,\text{kg}\,\text{m}^{-3}$ [45, 121]. $R_s(T) = R_s^*(T)$ given in (2.11) with $T^* = 70°\text{C}$. Other parameter values are given in Table C.1.

lands [3, 88, 65, 100]: such fires appear to be extinguished, but smoulder underground throughout the winter and re-emerge the following year [88]. Zombie fires are generally believed to happen as a result of surface wildfires [3]. Here, we suggest that R-tipping to a subsurface hot metastable state because of atmospheric warming is a main cause of Zombie fires. Furthermore, we show that such R-tipping can be triggered by realistic climate patterns ranging from summer heatwaves to global warming.

Figure 2.2 shows the soil temperature change in response to seasonal variations of the atmospheric temperature. Rather amazingly, *a summer heatwave* in year 10 breaks the seasonal response pattern and triggers a sudden transition to a hot metastable state that lasts for over a decade[6] and releases most of the carbon from the soil into the atmosphere. Following this, the system settles to a lower than initial soil temperature pattern for a refractory period of over a century, during which time both soil carbon

[6]The duration of the metastable state depends on its temperature $T \approx T^*$.

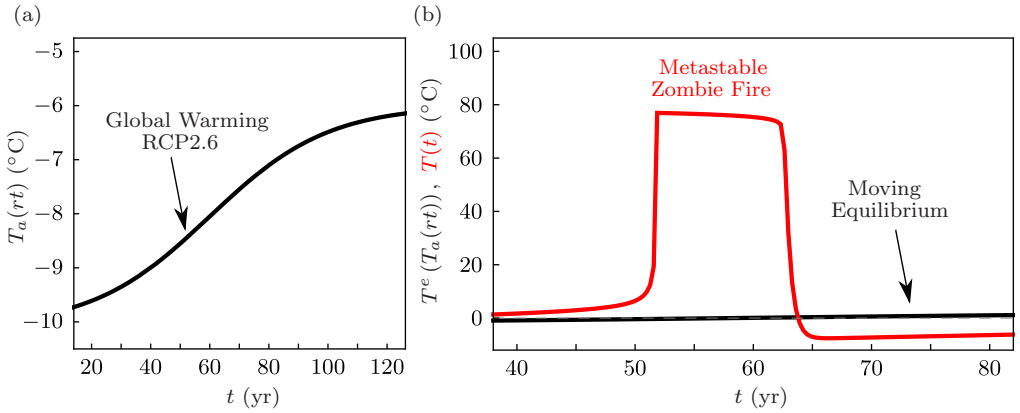


Figure 2.3: (a) A realisation within the range of uncertainty of the "very stringent" low-emissions RCP2.6 global warming scenario for Arctic regions [74, 73], based on observations at Cherskii in Northern Siberia [2]; see (A.3) for details of $T_a(rt)$. (b) Time evolution of (black) the moving equilibrium soil temperature $T^e(T_a(rt))$ from (2.12) and (red) the actual soil temperature $T(t)$ obtained by solving (2.3)–(2.4) in response to the external input $T_a(rt)$ from panel (a). Initial soil temperature is $T(0) = T_a^- + \frac{A\Pi}{\lambda} \approx -1.95$°C. Initial soil carbon $C(0)$ and $R_s(T)$ are the same as in figure 2.2. Other parameter values are given in Table C.1.

and soil temperature slowly increase back to their initial seasonal patterns.

Figure 2.3 shows the mean soil temperature change in response to a slow increase in the mean atmospheric temperature of 4°C over 200 years. We use 4°C in this example because the global climate change mitigation target is an increase in the global mean temperature of 2°C by 2100 compared to pre-industrial levels (1850–1900) [63, 96]. Note that the 2°C target is within the range of uncertainty of CMIP5 outputs under two greenhouse gas concentration pathways: the "very stringent" RCP2.6 that gives a 1.5°C increase, and the "intermediate" RCP4.5 that gives a 2.4°C increase [73]. Due to the well documented phenomenon of "Arctic amplification" [73, 89], this target corresponds to an increase of roughly 4°C in the Arctic mean temperature over the same period. In this scenario, a sudden transition to a hot metastable state that lasts for over a decade is triggered, and astonishingly occurs after only a modest mean temperature increase of ≈ 1.1°C.

(b) *Qualitative and quantitative agreement with PDE models.* The conceptual Ordinary Differential Equation (ODE) model (2.3)–(2.4) with the more realistic $R_s(T) = R_s^*(T)$ captures the key nonlinearities of the soil-carbon system. This is evidenced by the ODE model reproducing both qualitatively and quantitatively the peat soil instability predicted by a medium-complexity Partial Differential Equation (PDE) model of Siberian permafrost carbon dynamics under climate change [45, 46]. Specifically, figure 2.4 shows that the ODE model manages to capture the four key features of the PDE dynamics: permafrost thawing, R-tipping to the hot metastable state that lasts for half a century, a sudden soil cooling to a lower than initial soil temperature, followed by a slow increase to a low but higher than initial soil temperature.

The R-tipping instabilities in figures 2.2 and 2.3 arise when time-variation of the atmospheric temperature interacts with different inherent timescales of the soil-carbon system. Our next aim is to understand this interaction and uncover the underlying dynamical mechanisms. Thus, the remainder of the thesis is devoted to mathematical analysis of these instabilities in the soil-carbon model (2.3)–(2.4) with $R_s(T) = R_s^*(T)$ given in equation (2.11) and canonical inputs $T_a(rt)$ introduced in sections 5 and 6.

2.6 Excitability in The Nonautonomous Soil-Carbon Model

Figures 2.2–2.4 clearly show the features of excitability defined in section 1.4. In figure 2.5(a) we reproduce figure 2.3(b) and identify the different stages of the excitable response. Namely, the quiescent state, excitable response, transient state and refractory period (see figure 1.3 for reference to a traditional excitable system). In figure 2.5(b), we show that each stage of excitability is also significant from a physical standpoint. Namely, the attracting base state, thermal runaway, metastable zombie fire and carbon recovery respectively.

In summary, figure 2.5 showcases the equivalence of reversible R-tipping due to crossing a quasithreshold and excitability in the type-B sense discussed in

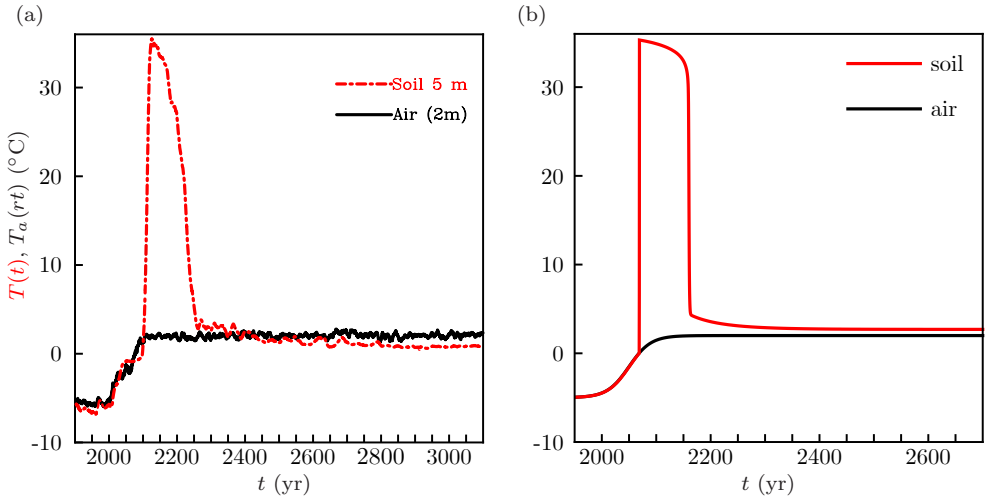


Figure 2.4: (a) The output of a PDE model [46] parameterised by data from near Cherskii in Siberia to simulate a soil column with a depth of 12m and a volumetric carbon density of $33\,\mathrm{kg\,m^{-3}}$, reproduced from [45, Fig.4(a)]. Shown are time evolution of (black) air temperature at 2 metres above the ground, and (red) soil temperature at a depth of 5m. (b) Time evolution of (red) the soil temperature $T(t)$ obtained by solving (2.3)–(2.4) in response to an increase in (black) atmospheric temperature $T_a(rt)$ given in (A.4). For comparison with (a), we use $\Pi = 0.09$ kg m^{-2} y^{-1}, $R_s(T) = 0$ for $T \leq 0$ as in [45], and $R_s(T) = R_s^*(T)$ given in (2.11) with $T^* = 30°\mathrm{C}$ for $T > 0$. Initial soil temperature is $T(0) = -6°\mathrm{C}$. Initial soil carbon is $C(0) = 396\,\mathrm{kg\,m^{-2}}$, which corresponds to a soil column with a depth of 12 m and a volumetric carbon density of $33\,\mathrm{kg\,m^{-3}}$ matching [45]. Other parameter values are given in Table C.1.

section 1.4 and [112]. It is clear that the soil carbon model (2.3)– (2.4) is an excitable system. The following sections will uncover the nature of the return mechanism, the excitable response and most significantly the nature of the excitability quasithresholds. While our analysis is from the point of view of R-tipping, given the strong connection to excitability theory we note that the methods employed will also be of interest to researchers studying excitable systems. In particular, the R-tipping quasithresholds we identify are also excitability quasithresholds, and we signpost where the R-tipping quasithresholds that we identify represent new kinds of excitability quasithresholds that have not been reported on to date.

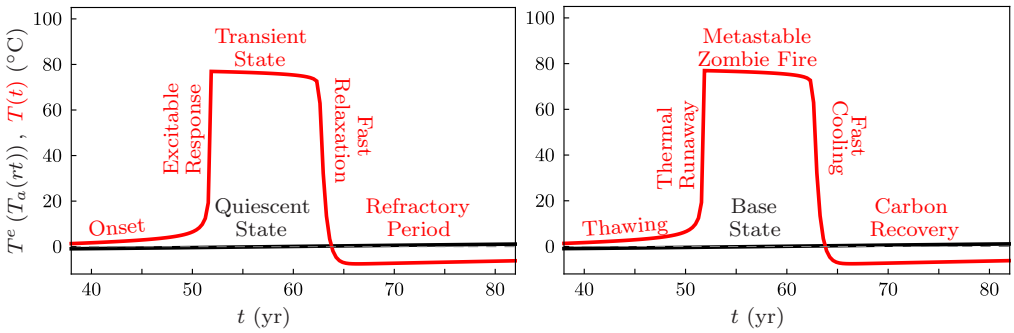


Figure 2.5: (a) Recreation of figure 2.3(b), with the different stages of the excitable response highlighted. (b) The stages of the excitable response relabelled to show the physical significance of each stage.

Chapter 3

The Autonomous Compactified Soil-Carbon Model

To facilitate mathematical analysis of non-obvious dynamical mechanisms that are responsible for the R-tipping instabilities in figures 2.2 and 2.3, we:

- Consider canonical external inputs $T_a(rt)$ that tend exponentially to a constant at infinity and generalise the linear ramp input used in [112].
- Use the compactification technique of [114, 113] to transform the R-tipping problem in the nonautonomous system (2.3)–(2.4) into a heteroclinic orbit problem in an autonomous compactified system in the limit $\epsilon = 0$ [76, 117].

3.1 Asymptotically Constant External Inputs

We choose to work with external inputs $T_a(rt)$ that decay exponentially to a constant $T_a^{\pm}$ as time t tends to $\pm\infty$. To be precise, we follow [113, Def.6.1] and define

Definition 3.1.1. We say $T_a(rt)$ is *exponentially bi-asymptotically constant* if, for all $r > 0$,

$$\lim_{t\to\pm\infty} T_a(rt) = T_a^{\pm} \in \mathbb{R} \quad \text{and} \quad \lim_{t\to\pm\infty} \frac{dT_a(rt)/dt}{e^{\mp\rho rt}} \in \mathbb{R},$$

for some *decay coefficient* $\rho > 0$.

Thus, we can define the autonomous *past limit system* with $T_a(rt) = T_a^-$,

$$\epsilon \frac{dT}{dt} = f_1(T, C, T_a^-), \tag{3.1}$$

$$\frac{dC}{dt} = f_2(T, C), \tag{3.2}$$

and the autonomous *future limit system* with $T_a(rt) = T_a^+$,

$$\epsilon \frac{dT}{dt} = f_1(T, C, T_a^+), \tag{3.3}$$

$$\frac{dC}{dt} = f_2(T, C), \tag{3.4}$$

which are examples of the frozen system. We note that, unlike the nonautonomous soil-carbon model (2.3)–(2.4), the autonomous past (3.1)–(3.2) and future (3.3)–(3.4) limit systems contain the equilibria

$$e^- := e(T_a^-) \quad \text{and} \quad e^+ := e(T_a^+), \tag{3.5}$$

respectively, and $e(rt) \to e^\pm$ as $t \to \pm\infty$ for any $r > 0$. The next step is to include these limit systems and their equilibria in the model.

3.2 Compactification

In this section, we reformulate the two-dimensional nonautonomous soil-carbon model (2.3)–(2.4) with exponentially bi-asymptotically constant input $T_a(rt)$ as a three-dimensional autonomous compactified system that includes the autonomous dynamics and equilibria e^- and e^+ of the limit systems (3.1)–(3.2) and (3.3)–(3.4) from infinity.

In the standard approach [49], the two-dimensional nonautonomous system (2.3)–(2.4) is augmented with an unbounded dependent variable $u = rt$, which gives an extended autonomous system on $\mathbb{R}^3$ that does not have any equilibria. Here, we use a different approach. We follow [114, Sec.4] and [113, Sec.6] and augment the nonautonomous system (2.3)–(2.4) with a bounded dependent

variable

$$s = g_\nu(rt) = \tanh\left(\frac{\nu}{2}\, rt\right). \tag{3.6}$$

We note that $s \in (-1, 1)$ for $t \in \mathbb{R}$ and all $r > 0$, use the definition of $\tanh^{-1}$ to obtain the inverse

$$rt = g_\nu^{-1}(s) = \frac{1}{\nu}\, \ln \frac{1+s}{1-s}, \tag{3.7}$$

and differentiate (3.6) with respect to t to derive the differential equation for s:

$$\frac{ds}{dt} = \frac{\nu r}{2}\,(1 - s^2).$$

Next, we continuously extend the new dependent variable s to include the limits from $t = \pm\infty$, which correspond to $s = \pm 1$. This gives the *autonomous compactified system*

$$\epsilon\, \frac{dT}{dt} = f_1(T, C, T_a^\nu(s)), \tag{3.8}$$

$$\frac{dC}{dt} = f_2(T, C), \tag{3.9}$$

$$\frac{1}{r}\, \frac{ds}{dt} = \frac{\nu}{2}(1 - s^2), \tag{3.10}$$

with the continuously extended external input

$$T_a^\nu(s) = \begin{cases} T_a\left(g_\nu^{-1}(s)\right) & \text{for} \quad s \in (-1, 1), \\ T_a^+ & \text{for} \quad s = 1, \\ T_a^- & \text{for} \quad s = -1. \end{cases} \tag{3.11}$$

For $T_a(rt)$ with a decay coefficient ρ, we choose the *compactification parameter* $\nu \in (0, \rho]$ so the compactified system is continuously differentiable on the extended phase space $\mathbb{R}^2 \times [-1, 1]$; see [114, Cor.4.1] and [113, Prop.6.1]. We discuss different choices of ν for the canonical external inputs in Sections 5 and 6, respectively.

3.2.1 Continuous Differentiability of The Compactified System

For $s \in (-1, 1)$, the right hand side of (7.8)–(7.10) is given by:

$$\epsilon \frac{dT}{dt} = f_1(T, C, T_a(g_\nu^{-1}(s))), \tag{3.12}$$

$$\frac{dC}{dt} = f_2(T, C), \tag{3.13}$$

$$\frac{1}{r}\frac{ds}{dt} = \frac{\nu}{2}(1 - s^2), \tag{3.14}$$

which after applying the inverse compactification transformation (3.7) defines a vector field where two components dT/dt and dC/dt are equivalent to the nonautonomous system (2.1), and so are continuously differentiable. As ds/dt is a polynomial in s, it is also continuously differentiable. What remains to be shown is the continuous differentiabilty of (7.8)–(7.10) when $s = \pm 1$. While we refer to [114, Cor.4.1] for a formal proof of the necessary conditions, we provide a sketch overview here.

Note that by the chain rule:

$$\lim_{s\to\pm 1} \frac{d}{ds} T_a(g_\nu^{-1}(s)) = \lim_{s\to\pm 1} \dot{T}_a(g_\nu^{-1}(s))\dot{g}_\nu^{-1}(s) = \lim_{t\to\pm\infty} \frac{\dot{T}_a(rt)}{\dot{g}_\nu(rt)} \tag{3.15}$$

Note also that since the compactification transformation (3.6):

$$\dot{g}_\nu(rt) \sim 2\nu\, r\, e^{\nu r} \quad \text{as} \quad t \to \pm\infty, \tag{3.16}$$

it follows that if the limit:

$$\lim_{t\to\pm\infty} \frac{dT_a(rt)/dt}{e^{\rho t}}, \tag{3.17}$$

exists for some $\rho > 0$, then $\lim_{s\to\pm 1} \frac{d}{ds} T_a(g_\nu^{-1}(s))$ exists for all $\nu \in (0, \rho]$ and the compactified system (7.8)–(7.10) is C^1-smooth for all such ν. We ensure throughout that we choose values of ν that are compatable with our chosen external inputs.

3.2.2 Special Case: Compactification Using The External Input

To represent global warming in section 5, we use the external input:

$$T_a(rt) = \frac{T_a^+}{2}\left(\tanh\left(rt\right) + 1\right). \tag{3.18}$$

Applying the parameterised compactification transformation (3.6) with $\nu = 2$ [1] and in particular the inverse transformation (3.7) we obtain:

$$T_a(g_2^{-1}(s)) = \frac{T_a^+}{2}\left(s + 1\right) \tag{3.19}$$

Together with (3.11), this defines a smooth, invertible change of coordinates between s and T_a. In particular, this means that the s component of the compactified vector field may be exchanged for a T_a component through an application of the chain rule:

$$\begin{aligned} \epsilon\,\frac{dT}{dt} &= f_1(T, C, T_a^2), \\ \frac{dC}{dt} &= f_2(T, C), \\ \frac{1}{r}\,\frac{dT_a^2}{dt} &= \frac{2rT_a}{T_a^+}\left(T_a^+ - T_a\right). \end{aligned} \tag{3.20}$$

The advantage of choosing $\nu = 2$ is that the extra compactified dimension has a clear physical meaning. However, the drawback is that the extra eigendirections of the equilibria of the limit systems that are gained through compactifcation (see section 3.3) in the planes $T_a = 0$ and $T_a = T_a^+$ are not guaranteed to be normal to these planes. It follows that $W^{u,[r]}(\tilde{e}^-)$, the unstable manifold of $\tilde{e}^-$ which we focus on in the present study, will not be guaranteed to be normal to the plane $T_a = T_a^-$.However, as $W^{u,[r]}(\tilde{e}^-)$ corresponds to a pullback attractor of the nonautonomous system (2.1), it may still be still well approximated with a modified version of the set-up described in section 7.1.

[1] Note that this is the maximum possible value of ν at which the system is continuously differentiable.

3.3 Stability of Equilibria for the Compactified System

A particular advantage of compactification is that the flow-invariant planes

$$\mathbb{R}^2 \times \{-1\} \quad \text{and} \quad \mathbb{R}^2 \times \{1\}, \tag{3.21}$$

of the extended phase space $\mathbb{R}^2 \times [-1, 1]$ contain equilibria e^- and e^+ of the autonomous past (3.1)–(3.2) and future (3.3)–(3.4) limit systems, respectively. When embedded in the extended phase space, e^- gains one unstable eigendirection with positive eigenvalue $\nu\, r > 0$ and becomes a hyperbolic saddle

$$\tilde{e}^- = \big(e^-, -1\big), \tag{3.22}$$

whereas e^+ gains one additional stable eigendirection with negative eigenvalue $-\nu\, r < 0$ and becomes a hyperbolic sink

$$\tilde{e}^+ = \big(e^+, 1\big), \tag{3.23}$$

which is the only attractor for the compactified system (7.8)–(7.10); see [114, Sec.3] and [113, Prop.6.3]. Furthermore, we note that the moving equilibrium $e(T_a(rt))$ with $t \in \mathbb{R}$ corresponds to

$$\tilde{e}(s) := \big(e(T_a\left(g_\nu^{-1}(s)\right), s\big) \text{ with } s \in (-1, 1),$$

in the extended phase space of the compactified system (7.8)–(7.10), and $\tilde{e}(s) \to \tilde{e}^\pm$ as $s \to \pm 1$.

3.4 Timescales of The Autonomous Compactified Soil-Carbon Model

As discussed in section 4.5, a key feature of many natural systems is that they evolve on multiple inherent timescales, which can be quantified by one or more

Timescales		
System Parameters	System Timescales	Case Name
$0 < \epsilon \ll 1,\ r = 0$	1 fast (T), 1 slow (C)	Frozen System
$0 < \epsilon r \ll \epsilon \ll 1$	1 fast (T), 1 slow (C) 1 super-slow (s)	Adiabtically slow
$0 < \epsilon r \lesssim \epsilon \ll 1$	1 fast (T), 2 slow (C, s)	Global Warming
$0 < \epsilon \ll \epsilon r \ll 1$	1 fast (T), 1 intermediate (s), 1 slow (C)	Intermediate
$0 < \epsilon \ll \epsilon r \lesssim 1$	2 fast (T, s), 1 slow (C)	Hot Summer Anomaly
$0 < \epsilon \ll 1 \ll \epsilon r$	1 super-fast (s), 1 fast (T), 1 slow (C)	Super-Fast Switch
$0 < \epsilon \ll 1,\ r \to \infty$	1 instantaneous (s), 1 fast (T) 1 slow (C)	Instantaneous Switch

Table 3.1: Different timescales are present in system (7.8) depending on the magnitude of the rate parameter r. The "Global Warming" and "Hot Summer Anomaly" are the two cases of primary interest.

small parameters. Such systems are often said to have a *separation* of timescales. This is true for example for many earth subsystems. The atmosphere itself, a key external input for earth subsystems, is often modelled with the timescales of the weather system and the climate "well separated" [40]. Identifying distinct timescales within a system is advantageous, as following section 1.5 such systems contain structure which may be exploited using geometric singular perturbation theory using the methods discussed in section 4.5. The nonautonomous soil-carbon model (2.3)–(2.4) is one such system. The left-hand side of (7.8)–(7.10) shows that it may evolve on up to three different timescales, depending on the rate parameter r. The system has two internal timescales, these are the *slow time* t which is the timescale of the *slow variable* C, and the *fast time* $\tau = t/\epsilon$ which is the timescale of the *fast variable* T. The *third time* $u = rt$ is an external timescale. This is the timescale of the external input $T_a(rt)$, which is represented by the augmented variable s. The relation between the timescales of the internal variables is most easily seen by substituting the fast time τ into

the compactified system (7.8)–(7.10):

$$\frac{dT}{d\tau} = f_1(T, C, T_a^\nu(s)), \tag{3.24}$$

$$\frac{dC}{d\tau} = \epsilon\, f_2(T, C), \tag{3.25}$$

$$\frac{ds}{d\tau} = \epsilon\, r\, \frac{\nu}{2}(1 - s^2), \tag{3.26}$$

where it becomes clear that what determines the relationship between the internal and external timescales of the model, is the magnitude of ϵr relative to ϵ. Assuming $0 < \epsilon \ll 1$ is fixed, the magnitude of the third time u relative to t and τ, and thus the total number of timescales in the model, depends on the magnitude of the rate parameter r. Including the two limiting cases, there are seven possible combinations of timescales which are summarised in table 3.1. Each case has a distinct geometry governing the dynamics, which may be uncovered using geometric singular perturbation theory.

The two most interesting and challenging cases are those in which the external timescale u is comparable to either the slow internal timescale t or the fast internal timescale τ. These cases are also the most physically relevant, and are explored in detail in chapters 5 and 6 respectively, and are the main focus of this thesis. In these two cases, the interaction of timescales leads to either a layer or reduced problem of dimension $n = 2$. This creates more complex dynamics in the singular limit $\epsilon \to 0$, which in turn produce complex dynamics when $0 < \epsilon \ll 1$. The seven possibilities for the timescales of system (7.8)–(7.10), summarised in table 3.1, are as follows:

(i) The autonomous *frozen system*, which is a limiting case when the external input is shut off, is represented by $r = 0$. The compactified system (7.8)–(7.10) becomes a 1-fast 1-slow system with the fast variable T, the slow variable C, and a fixed-in-time input parameter T_a. The frozen system contains a single small parameter ϵ. The frozen system evolves according to the unforced, internal dynamics of the system, serving as an important reference for when the system is externally forced. This case is examined in detail in section 4.1.

(ii) The *adiabatically slow* system is represented by either $r \ll \epsilon$ or $r \lesssim \epsilon$. The compactified system (7.8) becomes a 1-fast 1-slow 1-super-slow system with the fast variable T, the slow variable C, and the super-slow variable s. The *adiabatically slow* system contains two small parameters $0 < \epsilon\, r \ll \epsilon \ll 1$. This case is examined in section 4.6.

(iii) A *global warming scenario* is represented by $r \lesssim 1$. This means that $u = rt \lesssim t$ is another *slow time*, s becomes the second *slow variable*, and the compactified system (7.8)–(7.10) becomes a *1-fast 2-slow* system with the fast variable T and slow variables C and s. The compactified system with global warming contains a single small parameter ϵ, and interaction of the two slow timescales leads to non-trivial dynamics in the reduced problem, which are examined in detail in section 5

(iv) The *intermediate* system is represented by $1 \ll r \ll 1/\epsilon$. This means that $u = rt \gg t$ is an *intermediate time*, s becomes an *intermediate variable*. The compactified system (7.8)–(7.10) becomes a *1-fast 1-intermediate 1-slow* system with the fast variable T, intermediate variable s and slow variables C. The intermediate system contains two small parameters $0 < \epsilon\, r \ll \epsilon \ll 1$. This case is discussed briefly in chapter 6, to provide additional insight into the case when s is a fast variable.

(v) *A summer heatwave* is represented by $r \lesssim 1/\epsilon$. This means that $u = \epsilon r \tau \lesssim \tau$ is another *fast time*, s becomes the second *fast variable*, and the compactified system (7.8)–(7.10) becomes a *2-fast 1-slow* system with two fast variables, T and s, and one slow variable C. The compactified system with a summer heatwave contains two small variables $0 < \epsilon r \lesssim \epsilon \ll 1$, and the interaction between the two fast timescales leads to non-trivial dynamics in the layer problem, which are examined in detail in chapter 6.

(vi) A *super-fast shift* is represented by $r \gg 1/\epsilon$.The compactified system (7.8) becomes a 1-super-fast 1-fast 1-slow system with the super-fast variable s, fast variable T, and the slow variable C. The compactified system with a super-fast switch has two small parameters $0 < \epsilon \ll 1/\epsilon r \ll 1$. This

case is examined in section 4.5, relying on the analysis of an instantaneous switch in section 4.4.

(vii) The *instantaneous switch* system, which is a limiting case when the external input changes instantaneously, is represented by the limit $r \to \infty$. This means that the compactified system (7.8) becomes a 1-instantaneous 1-fast 1-slow system with the instantaneous or discontinuous variable s, fast variable T, and the slow variable C. In a sense, a discontinuous variable can be understood to have the fastest possible timescale relative to the other system variables. As well as being a case of timescale separation in its own right, the instantaneous switch system is the reduced problem for the case of a super-fast shift. The case of an instantaneous switch gives insight into soil-carbon model as an excitable system, and is physically relevant as permafrost peat soils are often subjected to sudden, discontinuous, even explosive changes [95, 22, 56]. The case of an instantaneous switch is examined in detail in section 4.4.

In the following chapters we will examine the dynamics of each timescale separation in turn. We focus on cases (i), (iii) and (v) in that we apply concepts and techniques of geometric singular perturbation theory [36, 43, 109, 55] first to (i) the autonomous frozen system and then to the autonomous compactified system (7.8)–(7.10) with (iii) global warming and (v) a summer heatwave, which allows us to define and analyse R-tipping in the soil-carbon model.

Chapter 4

Defining R-tipping due to Crossing Quasithresholds

4.1 Quasithresholds in The Frozen System

It is convenient to start the discussion with the frozen system obtained by setting $r = 0$ in system (2.3)–(2.4), so that T_a becomes a fixed-in-time input parameter. The frozen system is a 1-fast 1-slow singular perturbation problem with a small parameter ϵ. Taking the limit $\epsilon \to 0$ in the slow time t gives the (singular) *reduced problem*

$$\frac{dC}{dt} = f_2(T, C), \tag{4.1}$$

whose dynamics are restricted to the one-dimensional critical manifold

$$S(T_a) = \{(T, C) \ : \ f_1(T, C, T_a) = 0\} \subset \mathbb{R}^2.$$

Taking the limit $\epsilon \to 0$ in the fast time $\tau = t/\epsilon$ gives the *layer problem*

$$\frac{dT}{d\tau} = f_1(T, C, T_a), \tag{4.2}$$

where the slow variable C becomes an additional fixed-in-time parameter. Note that, for a given T_a, the critical manifold $S(T_a)$ consists of all branches of equi-

libria of the layer problem (4.2) parameterised by C. Hence, stability analysis of these equilibria gives stability of different branches of the critical manifold. Specifically, $S(T_a)$ has two normally hyperbolic attracting branches, denoted $S_1(T_a)$ and $S_3(T_a)$, which are separated from a normally hyperbolic repelling branch $S_2(T_a)$ by two non-hyperbolic fold points, denoted $F_1(T_a)$ and $F_2(T_a)$. In other words, the critical manifold can be partitioned as follows

$$S(T_a) = S_1(T_a) \cup F_1(T_a) \cup S_2(T_a) \cup F_2(T_a) \cup S_3(T_a).$$

The attracting branch $S_1(T_a)$ contains the equilibrium $e(T_a)$ of the frozen system. The other attracting branch, $S_3(T_a)$, is the hot metastable state that arises from the non-monotone microbial respiration function (2.11).[1] In figure 4.1(a), we show the dynamics of the reduced and layer problems, and introduce the (blue) *candidate quasithreshold* θ.

For $0 < \epsilon \ll 1$, the normally hyperbolic parts of $S(T_a)$ are guaranteed by the 'first' Fenichel theorem to perturb smoothly to nearby normally hyperbolic and *locally invariant slow manifolds* [35, 36, 43, 109, 55]. To be specific, $S_1(T_a)$ and $S_3(T_a)$ perturb to nearby attracting slow manifolds $S_{1,\epsilon}(T_a)$ and $S_{3,\epsilon}(T_a)$. Similarly, $S_2(T_a)$ perturbs to a nearby repelling slow manifold $S_{2,\epsilon}(T_a)$. Each slow manifold is usually non-unique in the sense that there is a family of such slow manifolds that lie exponentially close in ϵ to each other; see [109, Th.3.1] and [55, Th.3.1.4]. The strategy is to fix a representative for each of these manifolds and work with these representatives. Near the non-hyperbolic fold points $F_1(T_a)$ and $F_2(T_a)$, the hyperbolic branches $S_{1,\epsilon}(T_a)$, $S_{3,\epsilon}(T_a)$ and $S_{2,\epsilon}(T_a)$ typically split, meaning that they typically become slow manifolds with either one or two boundaries. In particular, $S_{1,\epsilon}(T_a)$ has one inflow boundary near $F_1(T_a)$, $S_{3,\epsilon}(T_a)$ has one outflow boundary near $F_2(T_a)$, while $S_{2,\epsilon}(T_a)$ has one inflow boundary near $F_1(T_a)$ and one outflow boundary near $F_2(T_a)$. Local invariance means that trajectories can enter or leave a slow manifold only through its boundary. Furthermore, the splitting of $S_{1,\epsilon}(T_a)$ and $S_{2,\epsilon}(T_a)$ near $F_1(T_a)$ gives rise to a narrow continuum of special solutions, referred to as *canards*, that move along $S_{2,\epsilon}(T_a)$ for some time [14, 34, 51, 92, 109]; see Fig. 4.1(b). In

[1] Note that this stable branch does not exist for the monotone respiration function in [60].

the remainder of the thesis we follow [107, 15] and [109, Sec.3.2.4] and identify three different types of canards.

Definition 4.1.1. In the autonomous frozen system and in the autonomous compactified system (7.8)–(7.10):

(i) *Canards "without head"* are solutions, or the corresponding trajectories, that move slowly along $S_{2,\epsilon}$ for time $t = \mathcal{O}(1)$ before moving quickly and directly to $S_{1,\epsilon}$.

(ii) *Canards "with head"* are solutions, or the corresponding trajectories, that move slowly along $S_{2,\epsilon}$ for time $t = \mathcal{O}(1)$, then move quickly and directly to $S_{3,\epsilon}$, then move slowly along $S_{3,\epsilon}$, before converging to $S_{1,\epsilon}$.

(iii) The *maximal canard* is the special solution, or the corresponding trajectory, that enters $S_{2,\epsilon}$ through its inflow boundary and exits $S_{2,\epsilon}$ through its outflow boundary.

Examples of the maximal canard, denoted θ_ϵ, a canard "without head" and a canard "with head" in the autonomous frozen system are shown in blue, cyan and magenta, respectively, in Fig. 4.1(b). Note that the (blue) maximal canard is a special example of a canard without head, and a perturbation of the candidate quasithreshold θ. In practice, the maximal canard is computed by choosing a suitable arclength and finding the solution along $S_2(T_a)$ that takes the longest time to trace out this arclength. The above discussion of canards highlights two main obstacles to defining R-tipping to the hot metastable state. First, the hot metastable state is a transient and thus quantitative phenomenon. In the long term, the system converges to the same stable state e^+ for any rate $r > 0$. Second, there is no unique threshold for R-tipping to the hot metastable state [113]. Rather, one speaks of a "quasithreshold" comprising a family of canards. As a consequence, there is no isolated critical rate for such R-tipping. The fast-slow analysis together with compactification allow us to overcome both of these obstacles. Our strategy is to relate nonautonomous and compactified system dynamics, and use these relations to define R-tipping for the nonautonomous system (2.3)–(2.4) in terms of slow manifolds and canards in the autonomous compactified system (7.8)–(7.10).

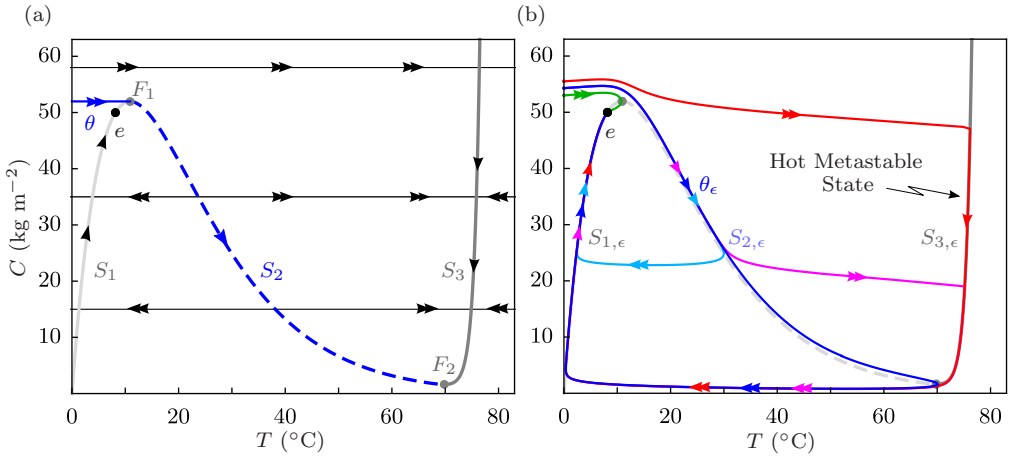


Figure 4.1: (a) The critical manifold $S(T_a)$ with (grey) two normally hyperbolic attracting branches, $S_1(T_a)$ and $S_3(T_a)$, and (dashed blue) a normally hyperbolic repelling branch $S_2(T_a)$, for the frozen system with $T_a = 0$ and $\epsilon = 0$. Shown also are (single arrows) the slow dynamics of the reduced problem (4.1) along $S(T_a)$ in the slow time t, and (double arrows) the fast dynamics of the layer problem (4.2) in the fast time τ for different values of C. (b) Five solutions to the frozen system with $T_a = 0$, $\epsilon \approx 0.064$, the same initial soil temperature $T(0) = 0$, and different initial carbon levels: (green) $C(0) = 53$, (cyan) $C(0) = 54.287996178057110079$, (blue) $C(0) \approx 54.28799617805711008$, (magenta) $C(0) = 54.287996178057110088$, and (red) $C(0) = 55.5$. Included for reference is (grey) $S(T_a)$. Other parameter values are given in Table C.1.

To be precise, we focus on R-tipping from e^-. Using the notation $x = (T, C) \in \mathbb{R}^2$ for the state variable of the soil-carbon system, we write

$$x^{[r]}(t, e^-) \in \mathbb{R}^2, \tag{4.3}$$

to denote the unique solution to the nonautonomous system (2.3)–(2.4) at time t, that limits to e^- as $t \to -\infty$ for a given rate parameter r, and varies nontrivially with r.[2] We also write $W^{u,[r]}(\tilde{e}^-)$ to denote the unique rate-dependent one-dimensional unstable invariant manifold of the hyperbolic saddle $\tilde{e}^-$ in the compactified system (7.8)–(7.10).[3] It follows from [113, Prop.6.4(a)] that $W^{u,[r]}(\tilde{e}^-)$

[2]This solution can be understood as a *local pullback attractor* for (2.3)–(2.4) [Th.2.2][13].

[3]For convenience, we leave out the dependence on ν in the notation for the unstable manifold.

contains $x^{[r]}(t, e^-)$ in the sense that

$$W^{u,[r]}(\tilde{e}^-) \supset \left\{(x, s) \ : \ x = x^{[r]}(t, e^-),\ s = g_\nu(t)\right\}_{t\in\mathbb{R}}. \tag{4.4}$$

This relation allows us to define tracking and R-tipping as follows:

Definition 4.1.2. Consider the nonautonomous system (2.3)–(2.4) with exponentially bi-asymptotically constant $T_a(rt)$ and decay coefficient $\rho > 0$, and the corresponding autonomous compactified system (7.8)–(7.10) with the compactification parameter $\nu \in (0, \rho]$. For a fixed $r > 0$:

(i) We say $x^{[r]}(t, e^-)$ *tracks* the moving stable equilibrium $e(T_a(rt))$ in system (2.3)–(2.4) if $W^{u,[r]}(\tilde{e}^-)$ connects to $\tilde{e}^+$ directly, that is without visiting $S_{2,\epsilon}$ or $S_{3,\epsilon}$, in system (7.8)–(7.10).

(ii) We say $x^{[r]}(t, e^-)$ *R-tips* in system (2.3)–(2.4), or say system (2.3)–(2.4) *R-tips* from e^-, if $W^{u,[r]}(\tilde{e}^-)$ visits $S_{3,\epsilon}$ before connecting to $\tilde{e}^+$ in system (7.8)–(7.10).

Next, we recognise that the nonautonomous system (2.3)–(2.4) with $0 < \epsilon \ll 1$ does not have unique R-tipping thresholds separating trajectories that track the moving stable equilibrium from those that R-tip, and does not have isolated critical rates r.[4] More precisely:

Definition 4.1.3. Consider the nonautonomous system (2.3)–(2.4) with exponentially bi-asymptotically constant $T_a(rt)$ and decay coefficient $\rho > 0$, and the corresponding autonomous compactified system (7.8)–(7.10) with the compactification parameter $\nu \in (0, \rho]$.

(i) We define a *critical range of* r as an interval of r for which $x^{[r]}(t, e^-)$ neither tracks the moving stable equilibrium $e(T_a(rt))$ nor R-tips.

(ii) For a fixed $r > 0$, we define an *R-tipping quasithreshold* in system (7.8)–(7.10) as a family of canards "without head" including the maximal canard, and in system (2.3)–(2.4) as a family of solutions $x^{[r]}(t)$ or trajectories corresponding to this family of canards.

[4] In some cases, e.g. the "complicated case" in Section 5.2.1, there is no unique critical rate even for $\epsilon = 0$.

4.2 Quasithresholds vs Regular Thresholds

There are important differences between *R-tipping quasithresholds* defined above and *regular R-tipping thresholds* introduced in [113]. To understand these differences, we consider the compactified system (7.8)–(7.10) and recall that, for typical values of r, $W^{u,[r]}(\tilde{e}^-)$ connects to an attractor for the future limit system [113, Rmk.5.1].

A *regular R-tipping threshold* is a codimension-one forward-invariant repelling manifold with inflow boundary.[5] Such a threshold is contained in the stable manifold of a *regular R-tipping edge state* that, in turn, is a compact invariant set with one unstable direction (not an attractor) for the future limit system; see [113, Def.5.1], [113, Def.5.3] and [113, Prop.6.4(b)]. Crossing a regular threshold typically occurs at special isolated *critical rates* r at which $W^{u,[r]}(\tilde{e}^-)$ enters a regular threshold and thus connects to a regular R-tipping edge state. Note that this behaviour is unusual for $W^{u,[r]}(\tilde{e}^-)$, which typically connects to an attractor.

In contrast, an *R-tipping quasithreshold* in Definition 4.1.1 is a codimension-zero family of canards "without head". Thus, crossing a quasithreshold occurs for *critical ranges of* r. Specifically, we expect the following behaviour across a transition from tracking to R-tipping due to crossing a quasithreshold. As r traverses the critical range, $W^{u,[r]}(\tilde{e}^-)$ contains a canard "without head". For different values of r in the critical range, $W^{u,[r]}(\tilde{e}^-)$ typically contains a different canard "without head". On the boundary of the critical range, $W^{u,[r]}(\tilde{e}^-)$ contains a maximal canard. Just past the critical range, $W^{u,[r]}(\tilde{e}^-)$ contains a canard "with head", giving R-tipping as per Definition 4.1.2(ii). Since a quasithreshold does not contain any regular edge states, $W^{u,[r]}(\tilde{e}^-)$ always connects to the same attractor $\tilde{e}^+$.

To relate quasithresholds to regular thresholds, we show in Sections 5 and 6 that if there is R-tipping due to crossing a quasithreshold in the soil-carbon model (2.3)–(2.4) with $0 < \epsilon \ll 1$, then $W^{u,[r]}(\tilde{e}^-)$ connects to a *singular R-tipping edge state* in the compactified system (7.8)–(7.10) with $\epsilon = 0$. However, there is no guarantee that a critical range of r for $0 < \epsilon \ll 1$ becomes an

[5] "Regular" means that it is embedded, orientable and normally hyperbolic.

isolated critical rate for $\epsilon = 0$. For example, we identify the "complicated case" in section 5.2.1, where the connection to a singular edge state for $\epsilon = 0$ persists on a critical range of r.

4.3 Threshold Instability for Quasithresholds

To give intuition for when to expect R-tipping due to crossing a quasithreshold in system (2.3)–(2.4), we extend the concept of threshold instability, introduced in [113, Def.4.5] for regular thresholds, to quasithresholds. Consider phase portraits for the frozen system with $\epsilon = 0$ and three different values of T_a in figure 4.2. Suppose that $T_a = 0°\text{C}$ and the system is settled at the base state $e(0)$; see figure 4.2(a). Then, there is a special value

$$T_a = T_a^{inst} \approx -\frac{1}{\alpha}\left(1 + \log\left(\alpha\frac{A\Pi}{\lambda}\right) - \alpha\frac{A\Pi}{\lambda}\right), \tag{4.5}$$

such that the base state for $T_a = 0$ crosses the candidate quasithreshold for $T_a = T_a^{inst}$, that is $e(0) \in \theta(T_a^{inst})$; see figure 4.2(b) and Appendix B.1. If T_a switches discontinuously from 0 to T_a^{max}, then $e(0)$ becomes the initial condition for the frozen system with $T_a = T_a^{max}$. Thus, if $T_a^{max} > T_a^{inst}$, $e(0)$ will find itself on the other side of the candidate quasithreshold $\theta(T_a^{max})$ and the system will undergo R-tipping; see figure 4.2(c). In section 4.4, we relate condition (4.5) to R-tipping conditions for $0 < \epsilon \ll 1$ and an instantaneous switch in $T_a(rt)$. In chapters 5 and 6, we relate condition (4.5) to R-tipping conditions for $0 < \epsilon \ll 1$ and continuously varying $T_a(rt)$.

In the remainder of the thesis, we study the interplay between the unstable manifold $W^{u,[r]}(\tilde{e}^-)$ and canards in the compactified system (7.8)–(7.10) to provide numerical verification and geometric insight into the different R-tipping mechanisms in figures 2.2 and 2.3. Furthermore, we exploit the fact that, in the limit $\epsilon = 0$, one can work with a reduced problem that approximates the slow dynamics, and with a layer problem that approximates the fast dynamics. These limit problems are of lower dimension than the compactified system (7.8)–(7.10), making R-tipping analysis more tractable. We use this approach for two

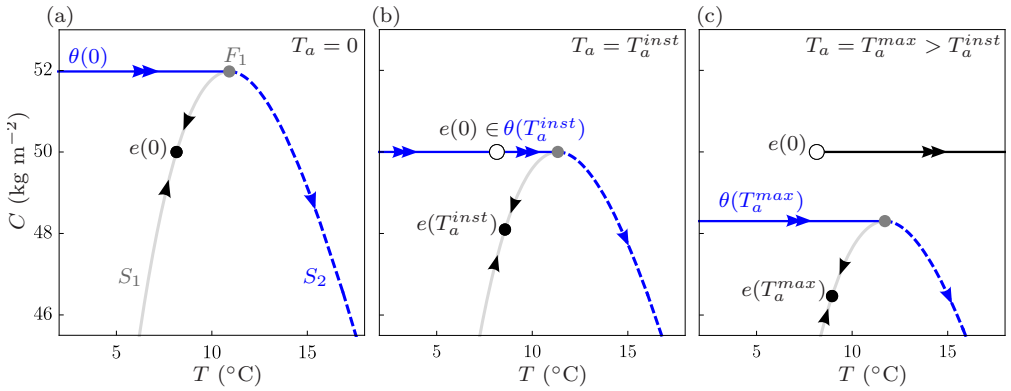


Figure 4.2: Phase portraits for the frozen system with $\epsilon = 0$ and three different values of T_a show when to expect R-tipping in the nonautonomous system (2.3)–(2.4) with $0 < \epsilon \ll 1$ and a time-varying T_a. Note the change in the position of the (blue) candidate quasithreshold $\theta(T_a)$ for different values of T_a relative to the fixed initial base state $e(0)$ at $T_a = 0$.

canonical external inputs $T_a(rt)$ from figure 5.1, which are exponentially bi-asymptotically constant and approximate the (a) global warming scenario from figure 2.3 and (b) summer heatwave from figure 2.2.

4.4 R-tipping Mechanism for an Instantaneous Switch

To illustrate tipping due to the crossing of a quasithreshold, we consider an instantaneous switch in $T_a(t)$ from a fixed atmospheric temperature $T_a^- = 0$ to some higher atmospheric temperature T_a^+ at time $t = 0$, as shown in Fig. 4.3(a). In addition to being an illustrative example, and a system undergoing the fastest possible forcing (discontinuous or $r \to \infty$), as discussed in section 3.4 we note that the system undergoing an instantaneous switch may also be used to understand the case of a super-fast switch when $r \gg 1/\epsilon$ (see section 4.5)

Suppose the system is initialised at e^-. Then, the system tracks $e(T_a(t))$ if T_a^+ is chosen such that e^- lies *below* the *R-tipping quasithreshold* for the frozen system with $T_a = T_a^+$; see the green trajectory in Figs. 4.1(b) and 4.3(a). The system R-tips if T_a^+ is chosen such that e^- lies *above* the R-tipping quasithresh-

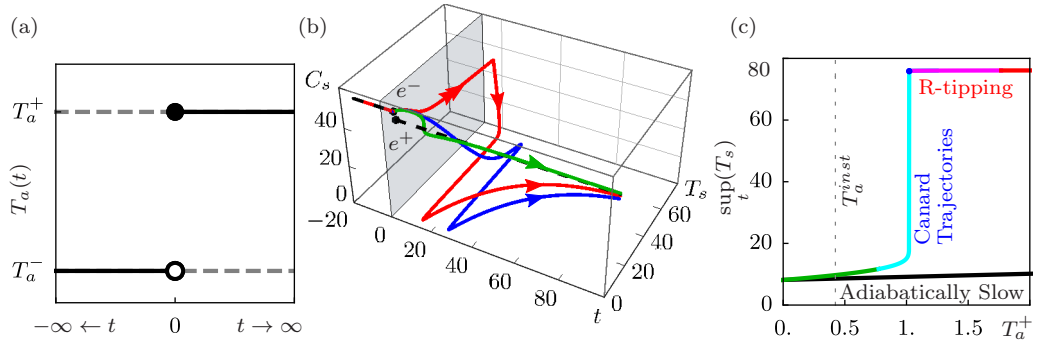


Figure 4.3: (a) An instantaneous switch in $T_a(rt)$ from T_a^- to T_a^+ at $t = 0$. (b) Solutions to the piecewise autonomous system with an instantaneous switch at $t = 0$ (grey) with $T_s^* = 70$. Each solution is initialised at e^- with $T_a^- = 0$, with a switch to $T_a^+ = 1$ (green), $T_a^+ \approx 1.021$ (blue) and $T_a^+ = 1.1$ (red). Solutions may converge to e^+ (green trajectory) or tip and visit the hot metastable state (red trajectory) depending on the magnitude of T_a^+. The transition to tipping occurs for a narrow but continuous range of T_a^+, where the system displays canard trajectories (blue trajectory). (c) The maximum value of T_s reached by solutions, depending on T_a^+, where the narrow, continuous transition to tipping may be seen. In this narrow interval, solutions are canards.

old for the frozen system with $T_a = T_a^+$; see the red trajectory in Figs. 4.1(b) and 4.3(a). However, if T_a^+ is chosen such that e^- lies *within* the R-tipping quasithreshold for $T_a = T_a^+$, then the system neither tracks nor R-tips. Rather, the system evolves along $S_{2,\epsilon}$ without visiting $S_{3,\epsilon}$ as shown by the blue canard trajectory θ_ϵ in Figs. 4.1(b) and 4.3(b). Thus, the family of canards "without head" including the maximal canard in the frozen system form an *R-tipping quasithreshold* for the system undergoing an instantaneous switch. This R-tipping quasithreshold gives rise to the *apparent discontinuity* in Fig. 4.3(c), which is an abrupt but continuous increase over a narrow interval of T_a^+ analagous to the one examined in figure 1.4. The apparent discontinuity converges to a proper discontinuity at $T_a^+ = T_a^{inst}$ as $\epsilon \to 0$. It follows that for the compost bomb model with an instantaneous switch, for R-tipping to occur for any $0 < \epsilon \ll 1$ it is a necessary but not sufficient condition that $T_a^+ > T_a^*$.

4.5 R-tipping Mechanism for a Super-Fast Shift

For completeness, we note that a super-fast nonlinear shift from $T_a^- = 0°\text{C}$ to a given $T_a^+ > 0$ with the rate parameter $r \gg 1/\epsilon$:

$$T_a(rt) = \frac{T_a^+}{2}\left(\tanh\left(rt\right) + 1\right), \tag{4.6}$$

may be approximated by the instantaneous switch discussed in the previous section. To see this, we examine the non-autonomous problem (2.3)–2.4 with external input 4.6. As $1/r$ is a small parameter, we take the limit $1/r \to 0$, which is equivalent to the limit $r \to \infty$. In the slow time t, the small parameter appears only in the external input which becomes:

$$T_a^\infty(t) = \lim_{r\to\infty} T_a(rt) = \lim_{r\to\infty}\left(\frac{T_a^+}{2}(\tanh(rt)+1)\right) = \frac{T_a^+}{2}\left(H(t)+1\right), \tag{4.7}$$

where $H(t)$ is the Heaviside step function with $H(0) = 1/2$. Note that if we replace $H(t)$ by:

$$\tilde{H}(t) = \begin{cases} 0 & \text{for} \quad t < 0, \\ 1 & \text{for} \quad t \geq 0, \end{cases} \tag{4.8}$$

which differs from $H(t)$ only on the measure-zero set $t = 0$, then the non-autonomous system with $T_a(rt) = T_a^\infty(t)$ is the instantaneous switch described in 4.4. In particular, since $dt/dt = 1 > 0$, the system dynamics are not affected by replacing $H(t)$ with $\tilde{H}(t)$.

4.6 Adiabatically Slow System

To contrast with an instantaneous switch, we consider an *adiabatically slow* external input $T_a(rt)$ with $0 < r \ll \epsilon \ll 1$ or $0 < r \lesssim \epsilon \ll 1$. It follows that (7.8) is a 1 fast (T) 1 slow (C) 1 super-slow (s) system. From [113, Th.7.1], we know already that for r small enough, $W^{u,[r]}(\tilde{e}^-)$ stays close to $\tilde{e}(s)$ and so the system tracks the moving equilibrium. However, in this section we will show this in detail using geometric singular perturbation theory. We treat (7.8) as a singular perturbation problem with small parameter r. Taking the limit $r \to 0$

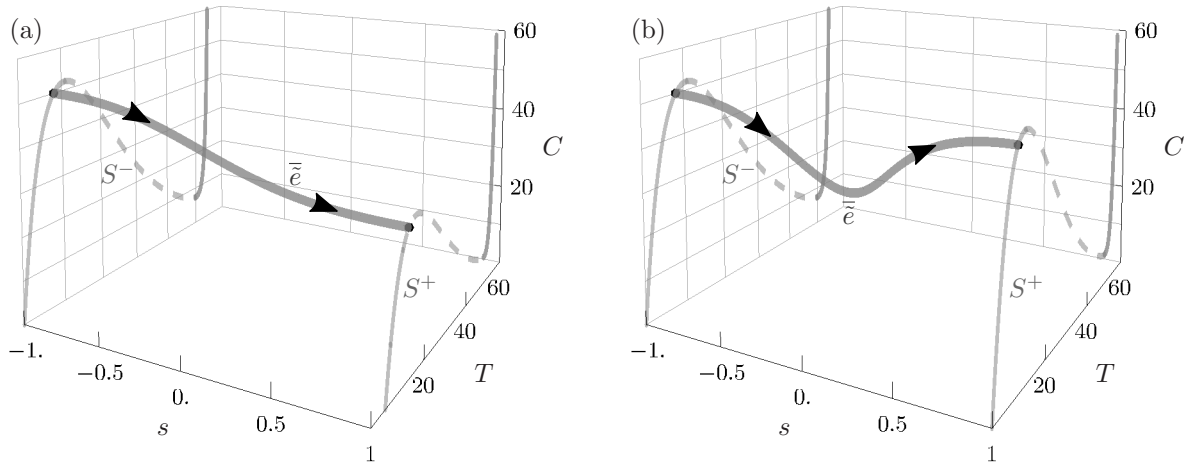


Figure 4.4: Shown are the (single arrows) reduced dynamics (4.9)–(4.11) for the adiabatically slow system along the (grey) critical manifold $\overline{\tilde{e}(s)}$ for (a) a monotone external input and (b) a non-monotone external input. Note that the (light grey) critical manifolds of the past and future limit systems are included for reference, but they do not form part of the critical manifold for the reduced system (4.9)–(4.11) for an adiabatically slow external input.

in the super slow time $u = rt$ gives the reduced problem:

$$0 = f_1(T, C, T_a^\nu(s)) \tag{4.9}$$

$$0 = f_2(T, C) \tag{4.10}$$

$$\frac{ds}{du} = \frac{1}{2}(1 - s^2). \tag{4.11}$$

The dynamics of the reduced problem are restricted to the critical manifold:

$$\overline{\tilde{e}} = \{\tilde{e}(s) : s \in [-1, 1]\}, \tag{4.12}$$

which contains the equilibria of the limit systems $\tilde{e}^{\mp}$ and also the moving equilibrium $\tilde{e}(s)$ for any $s \in (-1, 1)$.

The corresponding layer problem is found by taking $r \to 0$ in the slow time

t, which gives the frozen system:

$$\epsilon \frac{dT}{dt} = f_1(T, C, T_a^\nu(s)) \tag{4.13}$$

$$\frac{dC}{dt} = f_2(T, C) \tag{4.14}$$

$$\frac{ds}{dt} = 0, \tag{4.15}$$

in which s is a regular parameter of the system. As $e(T_a)$ is a normally hyperbolic stable equilibrium of the frozen system for all values of T_a, the critical manifold $\overline{\tilde{e}}$ consists of a single, attracting, everywhere normally hyperbolic branch. All solutions of the reduced problem (4.9)–(4.11) travel along $\overline{\tilde{e}}$ to $\tilde{e}^+$ at finite speed. For $0 < r \ll \epsilon \ll 1$, or $0 < r \lesssim \epsilon \ll 1$, the critical manifold $\overline{\tilde{e}}$ persists as a normally hyperbolic attracting slow manifold $\overline{\tilde{e}}_\epsilon$. A solution of (7.8) which begins on $\overline{\tilde{e}}_\epsilon$ will remain on $\overline{\tilde{e}}_\epsilon$ for all time independently of the form of the external input $T_a^\nu(s)$. Furthermore, as $W^{u,[r]}(\tilde{e}^-)$ contains the unique solution which limits in backwards time $t \to -\infty$ to $\tilde{e}^-$, we have that $W^{u,[r]}(\tilde{e}^-) = \overline{\tilde{e}}_\epsilon \backslash \tilde{e}^+$ and so is contained entirely within the slow manifold. As $\overline{\tilde{e}}_\epsilon$ lies $\mathcal{O}(\epsilon)$ close to $\overline{\tilde{e}}$ (see [55, Th.3.1.4]), it follows that $W^{u,[r]}(\tilde{e}^-)$ *δ-close tracks* the moving equilibrium $\tilde{e}(s)$ in the sense defined in [117, Def 3.2.13.] [6].

The instantaneous switch in section 4.4 represents the system (7.8) in the limit $r \to \infty$. For every value of T_a^+ that gives R-tipping for an instantaneous switch in figure 4.3(c), if $0 < r \ll \epsilon \ll 1$ the system will track the moving equilibrium, rather than R-tip. As the transition from loss of tracking to tipping in the case of an instantaneous switch is abrupt but continuous, it follows that for each such value of T_a^+ there must exist at least one *critical range* of r mediating a transition from tracking to R-tipping. In section 4.1, we precisely define the notion of an R-tipping quasithreshold, allowing for the precise definition of such a critical range. In sections 5 and 6, we will show that for a fixed T_a^+ it is possible to have multiple critical ranges of r.

[6] This is closely related to *ϵ-close tracking* defined in [13, Def.2.4]

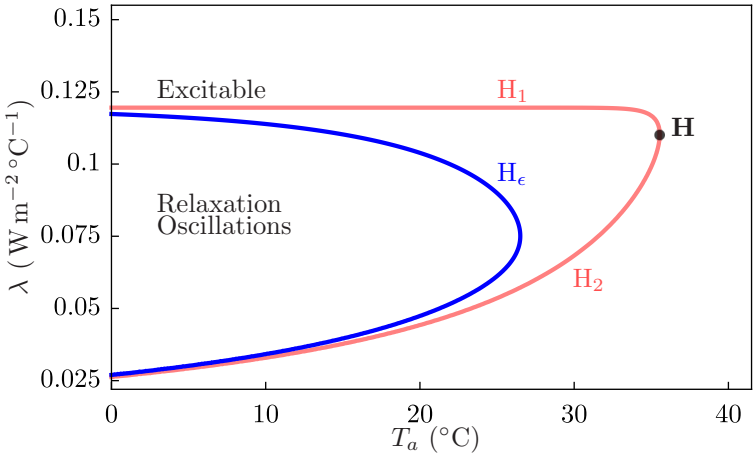


Figure 4.5: Two parameter bifurcation diagram of the frozen system in (T_a, λ). Shown are (blue) the supercritical singular Hopf bifurcation H_ϵ for $0 < \epsilon \ll 1$, as well as (red) the branches H_1 and H_2 where for $\epsilon = 0$, $e(T_a)$ coincides with F_1 and F_2 respectively. At the point H, all three of $e(T_a)$, F_1 and F_2 coincide.

4.7 Parameter Sensitivity of The Frozen System

In this section we examine the sensitivity of the model to changes in T_a, λ and Π, all of which may vary depending on the location, and physical characteristics of the soil. Specifically, we examine changes in the stability of the equilibrium $e(T_a)$ with respect to these parameters, as well as the shape and position of branches of the critical manifold $S(T_a)$, and the position of the special candidate trajectory $\theta(T_a)$, which perturbs to a maximal canard; see section 4.1.

4.8 Hopf Bifurcation and Relaxation Oscillations

Following section 4.1, we are interested in the behaviour of the frozen system for both $0 < \epsilon \ll 1$ and $\epsilon = 0$. We first note that a *singular Hopf bifurcation* is a Hopf bifurcation which occurs $\mathcal{O}(\epsilon)$ away from a fold point in both phase space and parameter space [38, 55]. Figure 4.5 shows (blue) the location of a

supercritical singular Hopf bifurcation of the frozen system for $0 < \epsilon \ll 1$ in (T_a, λ) parameter space. Note that here, λ is given in SI units rather than the units used in the rest of this study. Shown also in figure 4.5 is a red curve consisting of two branches H1 and H2, which emanate from a single point H. For $\epsilon = 0$, as the frozen system crosses H1 from above, $e(T_a)$ crosses from S_1 to S_2 via F_1 and changes stability type from stable to unstable. Along H1, $e(T_a)$ coincides with F_1. Similarly, as the system crosses H2 from above $e(T_a)$ crosses from S_2 to S_3 via F_2 and changes stability type, and along H2 is coincident with F_2. At the point H, all three of $e(T_a)$, F_1 and F_2 coincide. Above H_ϵ, the frozen system for $0 < \epsilon \ll 1$ is excitable. As the system crosses H_ϵ from above, the equilibrium $e(T_a)$ loses stability and the system undergoes small oscillations, followed by canard explosion (not shown) and relaxation oscillations. For this study, we work with $\lambda \approx 0.16\,\mathrm{W\,m^{-2}\,{}^{\circ}C^{-1}}$, away from the region of relaxation oscillations.

This discussion highlights the role of λ in the instability of the soil-carbon model. For smaller values of λ than is used in this study, the equilibrium of the frozen system $e(T_a)$ sits closer to the fold F_1 meaning that the system is more unstable with respect to forcing in atmospheric temperature T_a. That is to say, when there is less transfer of heat between the soil and air the system is less stable. Additionally, changing λ affects the position of the special candidate trajectory $\theta(T_a)$; see figure 4.6. This means that the system may be excited into crossing the corresponding quasithreshold by variations in λ, in addition to the variation in T_a examined the context of threshold instability in section B.1. This is significant, as the higher temperatures that we examine in this work are associated with drier weather, leading to drier soil and a drier moss layer. Drier soil and moss layers would result in decreased heat transfer between the soil and atmosphere, implying decreasing λ.

Figure 4.7 shows that the same singular Hopf bifurcation structure may also be induced by an increase in the gross primary production Π. This is significant as it is theorised, and has been observed, that increased global carbon emissions together with increasing temperatures may lead to a 'greening' of the Arctic, as readily available C02 leads to an increase in plant biomass and growth [17].

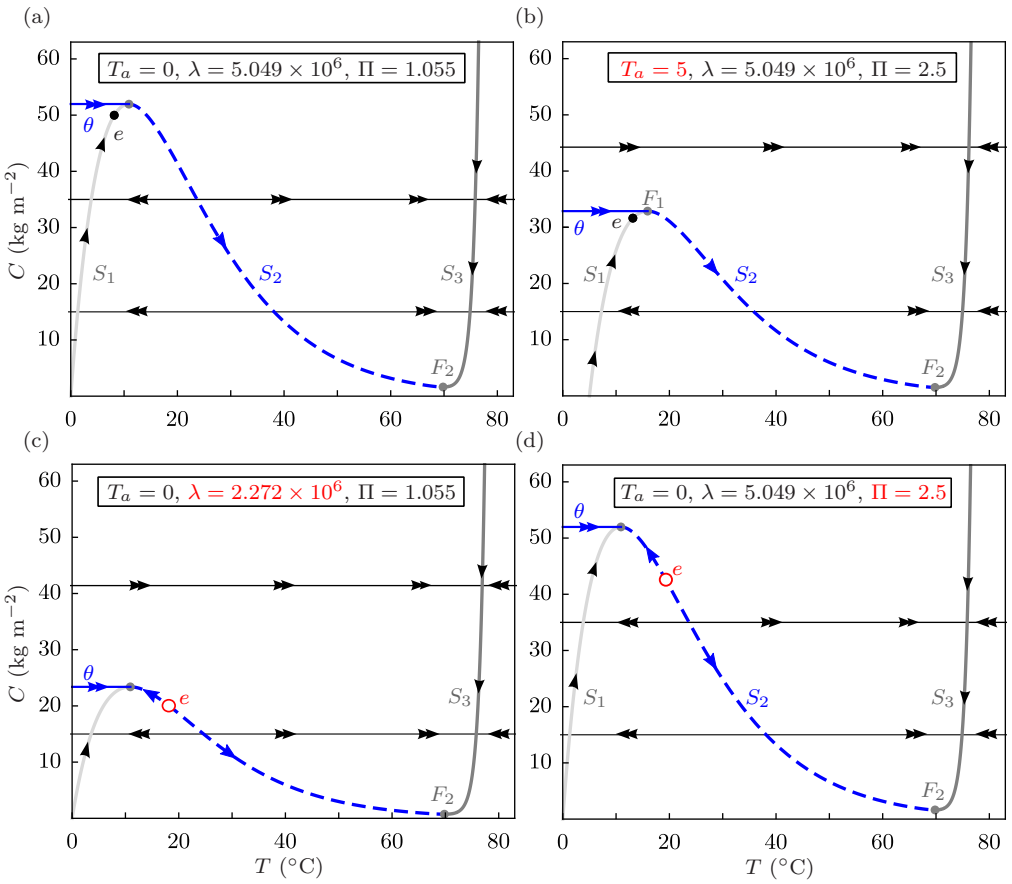


Figure 4.6: The critical manifold of the frozen system for (a) the parameter values as used in this work as in figure 4.1, (b) for $T_a = 5$°C, (c) for $\lambda = 2.272 \times 10^6\,\mathrm{J\,y^{-1}\,m^{-2}\,°C^{-1}}$ (d) for $\Pi = 2.5\,\mathrm{kg\,m^{-2}\,y^{-1}}$. Note in particular that in (c)–(d) the equilibrium e has crossed to S_2 and is unstable for both $\epsilon = 0$ and $0 < \epsilon \ll 1$, inducing relaxation oscillations.

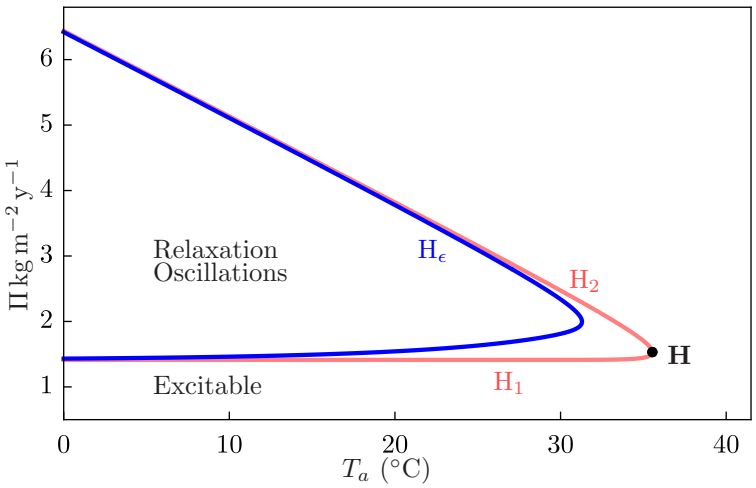


Figure 4.7: Two parameter bifurcation diagram of the frozen system in (T_a, Π). Shown are (blue) the supercritical singular Hopf bifurcation H_ϵ for $0 < \epsilon \ll 1$, as well as (red) the branches H_1 and H_2 where for $\epsilon = 0$, $e(T_a)$ coincides with F_1 and F_2 respectively. At the point H, all three of $e(T_a)$, F_1 and F_2 coincide.

In the context of this soil-carbon model, increased plant biomass would lead to an increase in gross primary productivity Π, which destabilises the system; see figures 4.7 and 4.6(d).

Chapter 5

R-tipping mechanisms for Global Warming

5.1 R-tipping and Canards in The Compactified System

The R-tipping instability in figure 2.3 arises because time-variation of the mean atmospheric temperature T_a interacts with the slow timescale of soil carbon C. Thus, we work with the reduced problem for the ensuing 1-fast 2-slow compactified system (7.8)–(7.10) to uncover the underlying dynamical mechanisms.

As a model of the global warming scenario, we consider a slow nonlinear shift from $T_a^- = 0°\text{C}$ to a given $T_a^+ > 0$ with the rate parameter $r \lesssim 1$:

$$T_a(rt) = \frac{T_a^+}{2}\left(\tanh\left(rt\right) + 1\right), \tag{5.1}$$

that decays exponentially with the decay coefficient $\rho = 2$ as per definition 3.1.1; see figure 5.1(a). We fix the compactification parameter $\nu = 1$ and consider system (7.8)–(7.10) with

$$T_a^\nu(s) = T_a^1(s) = \frac{T_a^+}{2}\,\frac{(1+s)^2}{1+s^2}, \tag{5.2}$$

which is obtained by applying the inverse compactification transformation (3.7)

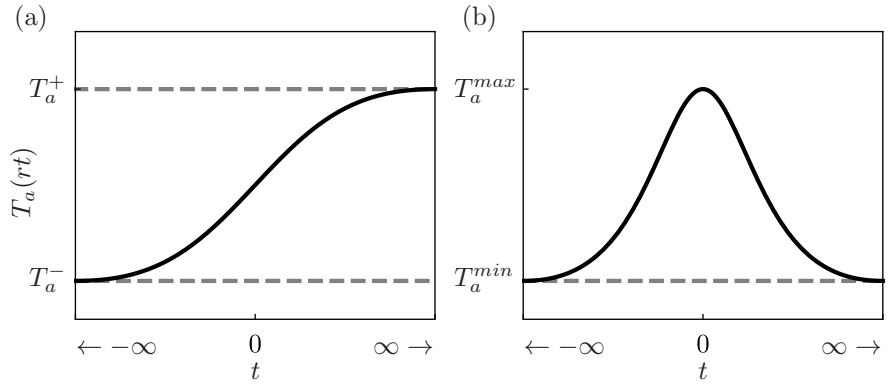


Figure 5.1: (a) A nonlinear shift from T_a^- to T_a^+ described by Eq. (5.1) approximating the global warming scenario in figure 2.3. (b) An impulse from $T_a^- = T_a^{min}$ to T_a^{max} and then back to $T_a^+ = T_a^{min}$ described by Eq. (6.1) approximating the summer heatwave in figure 2.2.

to (5.1). Our choice of $\nu = 1$ ensures that the corresponding system (7.8)–(7.10) is at least C^1-smooth on the extended phase space $\mathbb{R}^2 \times [-1, 1]$; see Sec. 3.2 and the references therein.

To give an overview of the dynamics near transitions from tracking to R-tipping, we plot an R-tipping diagram in the plane (T_a^+, r) of the input parameters; see figure 5.2. The diagram was obtained by computing $W^{u,[r]}(\tilde{e}^-)$ in system (7.8)–(7.10) for different values of T_a^+ and r, and using Definitions 4.1.1–4.1.3 to identify different dynamical regions for system (2.3)–(2.4). There are two R-tipping regions, and one tracking-tipping transition found for a large enough shift magnitude T_a^+. The smaller R-tipping region is a curious R-tipping tongue. This tongue gives rise to two (cyan) critical ranges of r for a fixed T_a^+ (one of them being very narrow), and suggests a possibility of different R-tipping cases for lower and higher magnitudes of the shift.

To gain geometric insight into the R-tipping instability caused by global warming, we plot in figure 5.3 the unstable manifold $W^{u,[r]}(\tilde{e}^-)$ for a fixed $T_a^+ = 5°\text{C}$ and three different rates $0 < r_1 < r_2 < r_3$ (see the black dots in figure 5.2), together with the critical manifold

$$S = \left\{(T, C, s) \ : \ f_1(T, C, T_a^1(s)) = 0\right\} \subset \mathbb{R}^2 \times [-1, 1], \tag{5.3}$$

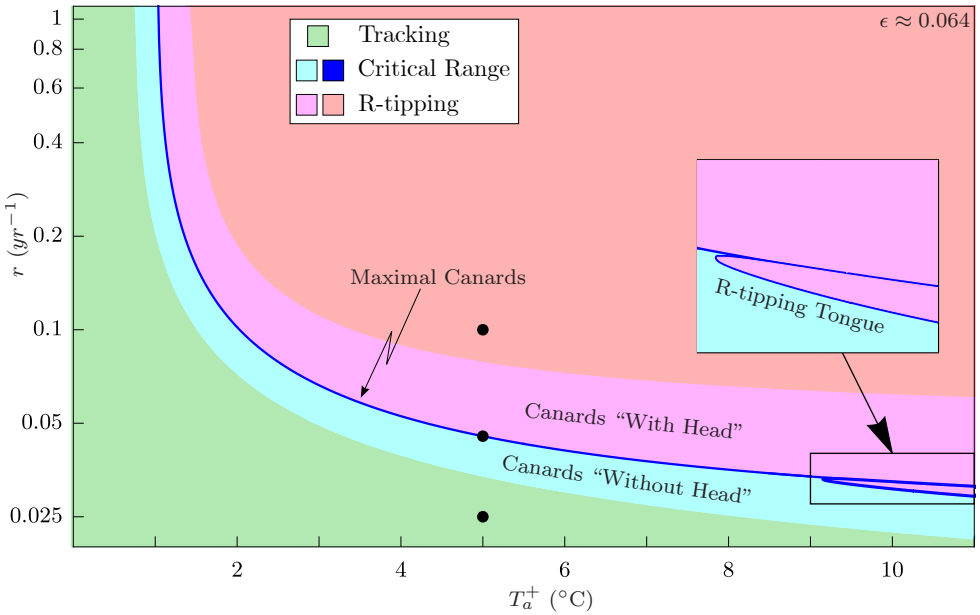


Figure 5.2: R-tipping diagram for nonautonomous system (2.3)–(2.4) with global warming scenario (5.1), in the plane of the shift amplitude T_a^+ and the rate parameter r, for $\epsilon \approx 0.064$. Shown are regions of (green) tracking, (cyan, blue) critical range, and (magenta, red) R-tipping from $\tilde{e}^-$. System parameter values are given in Table C.1.

for reference. Owing to the additional slow s-direction, the critical manifold S is now two-dimensional. It consists of two normally hyperbolic attracting sheets, S_1 containing $\tilde{e}(s)$, and S_3 being the hot metastable state, which are separated from a normally hyperbolic repelling sheet S_2 by two non-hyperbolic fold curves F_1 and F_2. Figure 5.3 shows that, as r is increased, tracking of $\tilde{e}(s)$ by (green) $W^{u,[r_1]}(\tilde{e}^-)$ is lost via canard trajectories, including the maximal canard contained in (blue) $W^{u,[r_2]}(\tilde{e}^-)$ that crosses F_1 and moves along S_2 for the longest time. This is followed by R-tipping at higher r as shown by (red) $W^{u,[r_3]}(\tilde{e}^-)$ that visits the hot metastable state $S_{3,\epsilon}$ before connecting to $\tilde{e}^+$. Thus, it should be possible to explain R-tipping instabilities caused by global warming in figure 5.2, including the curious R-tipping tongue, in terms of the slow dynamics of the reduced problem on S [112, 76, 98].

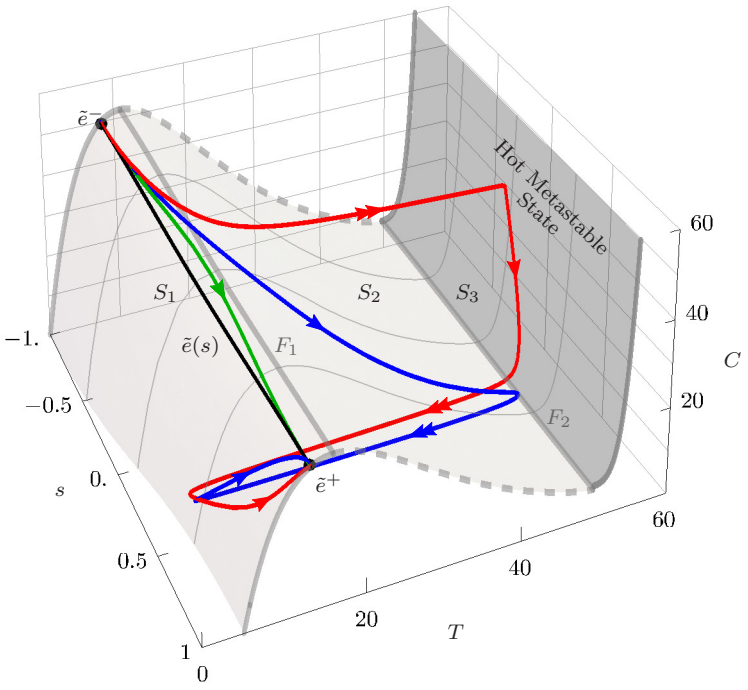


Figure 5.3: (Colour) The unstable invariant manifold $W^{u,[r]}(\tilde{e}^-)$ of the saddle $\tilde{e}^-$ for the compactified system (7.8)–(7.10) with $\epsilon \approx 0.064$, global warming scenario (5.2) with $T_a^+ = 5°\text{C}$, and three different values of the rate parameter: (green) $r_1 = 0.02$, (blue) $r_2 \approx 0.0454218$, and (red) $r_3 = 0.1$; see the black dots in figure 5.2. Included for reference is (grey) the critical manifold S defined in (5.3). System parameter values are given in Table C.1.

5.2 The Desingularised Reduced Problem

The reduced problem for the 1-fast 2-slow system (7.8)–(7.10) with global warming (5.2) is obtained by setting $\epsilon = 0$ in (7.8)–(7.10), which gives

$$0 = f_1(T, C, T_a^1(s)), \tag{5.4}$$

$$\frac{dC}{dt} = f_2(T, C), \tag{5.5}$$

$$\frac{ds}{dt} = \frac{r}{2}(1 - s^2). \tag{5.6}$$

This singular system describes the evolution of the slow variables C and s in the slow time t on the two-dimensional critical manifold S defined in (5.3). However,

the onset of R-tipping involves a sudden jump in the fast variable T, without any noticeable change in C. Thus, it is convenient to consider the evolution of the fast variable T in the slow time t on S, which is obtained by differentiating the critical-manifold condition in (5.3) or (5.4) with respect to t. Furthermore, we use this condition to project the slow flow within S onto the plane (T, s), i.e. eliminate the dependence on C, and reformulate the reduced problem as

$$\frac{dT}{dt} = -\frac{\partial f_1/\partial C \cdot f_2 + \partial f_1/\partial T_a^1 \cdot dT_a^1/ds \cdot ds/dt}{\partial f_1/\partial T}\bigg|_S, \tag{5.7}$$

$$\frac{ds}{dt} = \frac{r}{2}(1 - s^2), \tag{5.8}$$

where $|_S$ denotes restriction to S.

In the reduced problem (5.7)–(5.8), the question of loss of tracking boils down to whether $W^{u,[r]}(\tilde{e}^-)$ leaves S_1 through F_1. To address this question, we note that the denominator in (5.7) changes sign at a fold

$$\frac{\partial f_1}{\partial T}\bigg|_S \begin{cases} < 0 & \text{for} \quad (T, C, s) \in S_1 \cup S_3, \\ = 0 & \text{for} \quad (T, C, s) \in F_1 \cup F_2, \\ > 0 & \text{for} \quad (T, C, s) \in S_2. \end{cases} \tag{5.9}$$

It then follows that, depending on the numerator in (5.7), there are two types of fold points:

- A *jump point* [92] is a point p on a fold such that

$$\left(\frac{\partial f_1}{\partial C} \cdot f_2 + \frac{\partial f_1}{\partial T_a^1} \cdot \frac{dT_a^1}{ds} \cdot \frac{ds}{dt}\right)\bigg|_{p \in F_1 \cup F_2} \neq 0. \tag{5.10}$$

  If a solution of (5.7)–(5.8) approaches a jump point, the denominator in (5.7) approaches zero while the numerator remains finite, so that dT/dt tends to infinity, and $T(t)$ blows up in t. This means that the solution reaches a jump point in finite time and ceases to exist within S.[1] Jump points are typically found on open subsets of a fold [92].

[1] For $0 < \epsilon \ll 1$, the corresponding solution leaves the slow manifold and moves along the fast T-direction.

- A *folded singularity* [92] is a point q on a fold such that

$$\left(\frac{\partial f_1}{\partial C}\cdot f_2+\frac{\partial f_1}{\partial T_a^\nu}\cdot\frac{dT_a^\nu}{ds}\cdot\frac{ds}{dt}\right)\Bigg|_{q\in F_1\cup F_2}=0. \tag{5.11}$$

  If a solution of (5.7)–(5.8) approaches a folded singularity in a special direction where the numerator in (5.7) approaches zero faster than or at the same rate as the denominator in (5.7), then dT/dt remains finite, and this solution either grazes or crosses the fold at q with a finite speed. If the crossing is from an attracting to an unstable part of S, the solution, or the corresponding trajectory, is termed a *singular canard* [15, 14]. Folded singularities are typically found as isolated fold points.

Thus, in the singular limit $\epsilon=0$ for the slow time t, transitions from tracking to R-tipping caused by global warming can be understood in terms of singular canards through folded singularities [112, 68, 76]. These folded singularities are the "singular edge states" described in the introduction. The obstacle to analysis of folded singularities and their singular canards is that the right-hand side of (5.7) is undefined on F_1 and F_2. This obstacle is overcome by a *desingularisation* [92, 33] in the form of a state-dependent time rescaling:

$$dt=-d\hat{t}\,\frac{\partial f_1}{\partial T}\bigg|_S, \tag{5.12}$$

which gives the *desingularised system*

$$\frac{dT}{d\hat{t}}=\left(\frac{\partial f_1}{\partial C}\cdot f_2+\frac{\partial f_1}{\partial T_a^1}\cdot\frac{dT_a^1}{ds}\cdot\frac{ds}{dt}\right)\Bigg|_S \tag{5.13}$$

$$\frac{ds}{d\hat{t}}=-\left(\frac{\partial f_1}{\partial T}\cdot\frac{ds}{dt}\right)\Bigg|_S, \tag{5.14}$$

defined everywhere on S. In detail we obtain:

$$\frac{dT}{d\hat{t}}=R_s^*(T)\left(\Pi-\frac{\lambda}{A}\left(T-T_a^1(s)\right)\right)+\frac{r\lambda T_a^+}{2A}\left(\frac{1-s^2}{1+s^2}\right)^2, \tag{5.15}$$

$$\frac{ds}{d\hat{t}}=\frac{r\lambda}{2A}(1-s^2)\left(1+\alpha\left(T-T_a^1(s)\right)\frac{ce^{c\alpha(T-b)}-e^{-\alpha(T-b)}}{e^{c\alpha(T-b)}+e^{-\alpha(T-b)}}\right). \tag{5.16}$$

The main advantages of desingularisation are:

(i) Regular equilibria for the reduced problem (5.7)–(5.8) remain regular equilibria for the desingularised system (5.13)–(5.14). Folded singularities for (5.7)–(5.8) become (new) regular equilibria for (5.13)–(5.14). Hence the classification of folded singularities into "folded nodes", "folded foci", "folded saddles", and "folded saddle-nodes", based on their classification into different types of equillibria in (5.13)–(5.14) [92].

(ii) According to (5.9) and (5.12), the new time $\hat{t}$ in (5.13)–(5.14) flows in the same direction as t on S_1 and S_3, passes infinitely faster on F_1 and F_2, and reverses direction on S_2. Thus, a phase portrait for (5.7)–(5.8) can be obtained by producing the corresponding phase portrait for (5.13)–(5.14), reversing the direction of time (the arrows on trajectories) on S_2, and relabelling the (new) equilibria on F_1 and F_2 as folded singularities.

(iii) It follows from points (i) and (ii) above that a singular canard through a folded singularity in (5.7)–(5.8) can be obtained by smoothly concatenating two trajectories tangent to a stable eigendirection of the corresponding equilibrium in (5.13)–(5.14).

5.2.1 Three R-tipping Cases for $\epsilon = 0$

The above relations (i)–(iii) between the desingularised and reduced system dynamics allow us to identify three different cases of R-tipping in the singular reduced problem (5.7)–(5.8) through analysis of the regular desingularised system (5.13)–(5.14). Two of these cases are typical and closely related to the two cases of non-obvious tipping thresholds described in separate systems in [76], and termed as the "simple case" and the "complicated case". The third case is special and corresponds to a new *degenerate case* that separates the "simple case" and the "complicated case". Here, we identify all three cases in an unfolding of a *codimension-two global folded saddle-node type-I singularity*, which explains the problem at hand, consolidates the results of [76], and is of interest in its own right.

As the rate parameter r is increased in the desingularised system (5.13)–(5.14), there is a saddle-node bifurcation of equilibria on F_1 at some $r = r_{SN}$, giving rise to a saddle and a stable node. This corresponds to the following local bifurcation scenario in the reduced problem (5.7)–(5.8). When $r = r_{SN}$, a folded saddle-node type-I singularity (FSN-I) appears [52, 101]. As r is increased past r_{SN}, FSN-I bifurcates into a folded saddle (FS) and a folded node (FN). For even higher r, FN becomes a folded degenerate node (FDN) and subsequently turns into a folded focus (FF). Furthermore, it turns out that the saddle-node bifurcation in (5.13)–(5.14) can be a *a global bifurcation* in the sense that it can involve a heteroclinic orbit from $\tilde{e}^-$. Thus, we speak of a *global FSN-I* in the reduced problem (5.7)–(5.8).

To gain insight into the global dynamics in the reduced problem (5.7)–(5.8), we recall that FSN-I has one *folded-saddle-node singular canard* $\tilde{\gamma}^{SN}$, which crosses from S_1 to S_2 [92]. $\tilde{\gamma}^{SN}$ is obtained by computing the unique stable invariant manifold of the corresponding saddle-node equilibrium in the desingularised system (5.13)–(5.14). FS has one *folded-saddle singular canard* $\tilde{\gamma}^S$, which crosses from S_1 to S_2, and one *folded-saddle singular faux canard* $\tilde{\gamma}_f^S$, which crosses from S_2 to S_1 [14, 92]. $\tilde{\gamma}^S$ is obtained by computing the unique stable invariant manifold, and $\tilde{\gamma}_f^S$ by computing the unique unstable invariant manifold, of the corresponding saddle in (5.13)–(5.14). In contrast, FN has a family of singular canards that cross from S_1 to S_2 [92, 106]. A *folded-node strong singular canard* $\tilde{\gamma}_s^N$ is obtained by concatenating the two special solutions that approach the corresponding stable node in (5.13)–(5.14) along its strong eigendirection. In addition, there is a continuum of *folded-node weak singular canards*, each of which approaches FN along the weak eigendirection of the corresponding stable node in (5.13)–(5.14). The region of S_1 between $\tilde{\gamma}_s^N$ and F_1 containing the continuum of weak folded-node singular canards is referred to as the *singular funnel* [109, Def.3.11].[2] At FDN, $\tilde{\gamma}_s^N$ turns into $\tilde{\gamma}^{DN}$ and joins the continuum of singular canards that approach FDN along the one (degenerate) eigendirection of the corresponding stable degenerate node in (5.13)–(5.14). FF has no singular canards since every trajectory approaching the corresponding

[2]The singular funnel is shown in yellow in figures 5.4, 5.5 and 5.6.

stable focus in (5.13)–(5.14) reaches a jump point of F_1.

To be precise, we define tracking and R-tipping for $\epsilon = 0$ and slow external inputs as follows,

Definition 5.2.1. In the reduced problem (5.7)–(5.8):

(i) Tracking occurs when $W^{u,[r]}(\tilde{e}^-)$ connects to $\tilde{e}^+$ directly, that is without visiting F_1.

(ii) R-tipping occurs when $W^{u,[r]}(\tilde{e}^-)$ reaches a jump point on F_1.

We then note that, when $r < r_{SN}$, tracking occurs because the whole of F_1 is repelling, there are no folded singularities or canards, so $W^{u,[r]}(\tilde{e}^-)$ must remain on S_1 and connect directly to $\tilde{e}^+$. As the rate parameter r is increased past r_{SN}, $W^{u,[r]}(\tilde{e}^-)$ may interact with singular canards to cross F_1 and cause loss of tracking. Analysis of heteroclinic bifurcations in the desingularised system (5.15)–(5.16) reveals three cases of $W^{u,[r]}(\tilde{e}^-)$ crossing F_1, or equivalently three cases of loss of tracking:

(i) *Simple case:* $W^{u,[r]}(\tilde{e}^-)$ coalesces with the folded-saddle singular canard $\tilde{\gamma}^S$, and thus crosses from S_1 to S_2 via FS, at some critical rate $r = r_c > r_{SN}$.

(ii) *Complicated case:* $W^{u,[r]}(\tilde{e}^-)$ grazes F_1 at FSN-I when $r = r_{SN}$, coalesces with a folded-node weak singular canard when $r \in (r_{SN}, r_{Ns})$, coalesces with the folded-node strong singular canard $\tilde{\gamma}_s^N$ at some $r = r_{Ns} > r_{SN}$, and thus crosses from S_1 to S_2 via FN when $r \in (r_{SN}, r_{Ns}]$.

(iii) *Degenerate case:* $W^{u,[r]}(\tilde{e}^-)$ coalesces with the folded-saddle-node singular canard $\tilde{\gamma}^{SN}$, and thus crosses from S_1 to S_2 via FSN-I, at a critical rate $r_c = r_{SN}$.

In section 6, we refer to the three corresponding cases of R-tipping as the *slow R-tipping cases.*

We now discuss these three cases in terms of phase portraits for the reduced problem (5.7)–(5.8) on S by fixing three representative values of the shift magnitude T_a^+ and increasing the rate parameter r. To highlight interactions of

$W^{u,[r]}(\tilde{e}^-)$ with different singular canards, we colour S_1 in the phase portraits as follows. Solutions initialised in the *green* region remain in this region and converge directly to $\tilde{e}^+$. Solutions initialised in the *dark red* region reach a jump point of F_1 and cease to exist within S. Solutions initialised in the *yellow* (singular funnel) region are weak folded-node singular canards. The green and red regions are separated by the folded-saddle singular canard $\tilde{\gamma}^S$, whereas the red and yellow regions are separated by the folded-node strong singular canard $\tilde{\gamma}_s^N$. Finally, in the figures, we show projections of S onto the plane (T, s).

5.2.2 The simple case

As r is increased past r_{SN} for $T_a^+ = 1.5$, the appearance of FS and FN via FSN-I gives rise to folded-saddle and folded-node singular canards, and new dynamics. Of particular interest is an attracting interval of jump points on F_1 between FS and FN, and the corresponding (dark red) region of solutions between $\tilde{\gamma}^S$ and $\tilde{\gamma}_s^N$ that reach one of these jump points from S_1 and cease to exist within S; see figure 5.4 (a)-(b). In this case, $W^{u,[r]}(\tilde{e}^-)$ does not interact with FSN-I, meaning that the FSN-I is local. $W^{u,[r]}(\tilde{e}^-)$ does not interact with the folded-node singular canards either because it is separated from them by the folded-saddle singular canard $\tilde{\gamma}^S$. Rather, when $r = r_c$, $W^{u,[r]}(\tilde{e}^-)$ and $\tilde{\gamma}^S$ coalesce; see figure 5.4 (c). At this point, tracking is lost since $W^{u,[r]}(\tilde{e}^-)$ crosses F_1 from S_1 to S_2 via FS. For $r > r_c$, $W^{u,[r]}(\tilde{e}^-)$ reaches a jump point of F_1 and ceases to exist within S, or R-tips; see figure 5.4 (d).

Thus, in the simple case for $\epsilon = 0$, there is an isolated *critical rate* $r = r_c$. This critical rate is the value of r that gives a *codimension-one hetroclinic orbit* connecting $\tilde{e}^-$ to the corresponding saddle on F_1 in the desingularised system (5.15)–(5.16).

5.2.3 The complicated case

As r is increased past r_{SN} for $T_a^+ = 3.5$, the local bifurcation scenario is the same as in the simple case. However, the global dynamics are different in that $W^{u,[r]}(\tilde{e}^-)$ interacts with various folded-node singular canards.

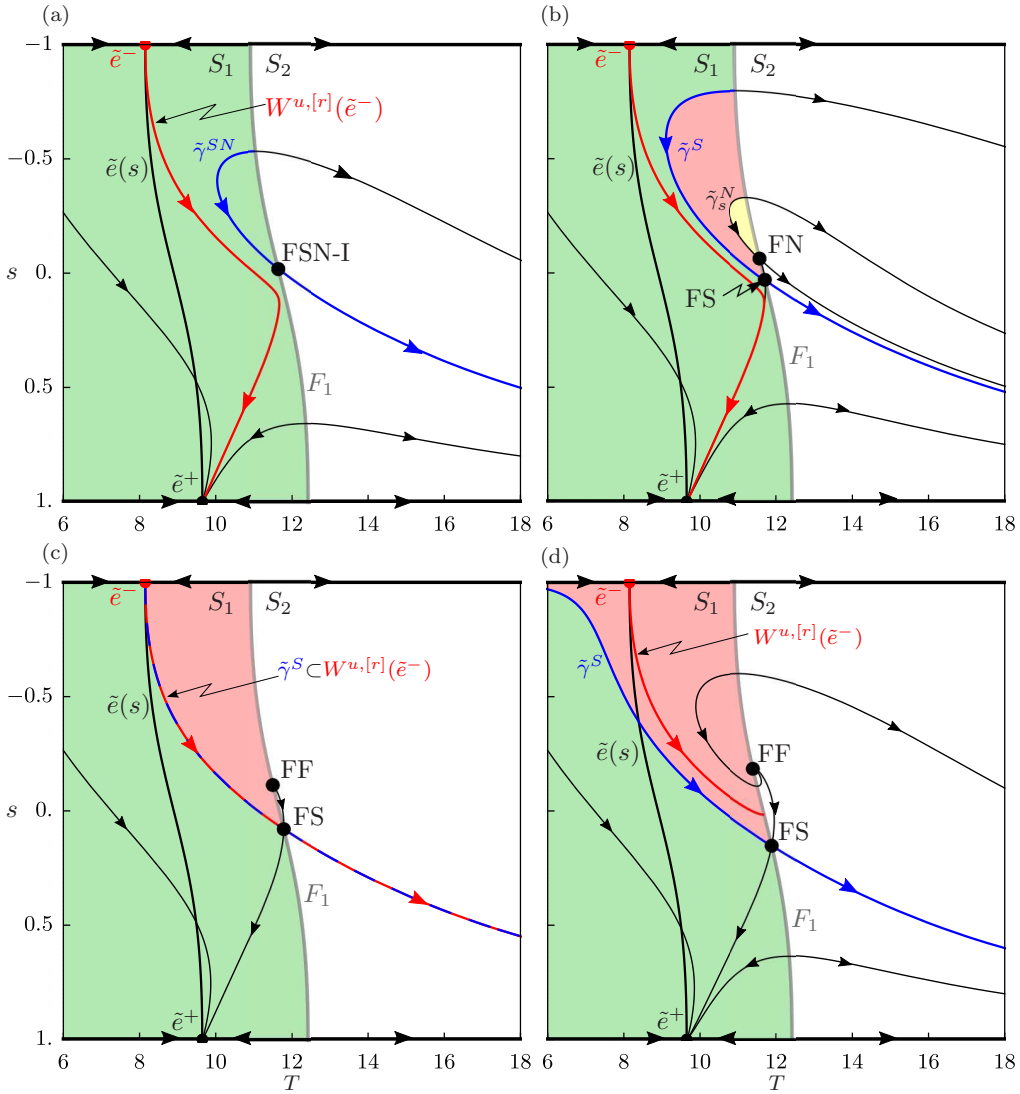


Figure 5.4: Phase portraits of the reduced problem (5.7)–(5.8) with nonlinear shift (5.2), obtained using the desingularised system (5.15). Shown is the simple case with a codimension-one local FSN-I in (a), and a codimension-one heteroclinic orbit connecting $\tilde{e}^-$ to FS in (c). $T_a^+ = 1.5$ and the rate parameter takes values (a) $r = r_{SN} \approx 0.107194$, (b) $r \approx 0.108119$, (c) $r = r_c \approx 0.111459$, and (d) $r = 0.12$; see the black dots in the left inset of figure 5.7. System parameter values are given in Table C.1.

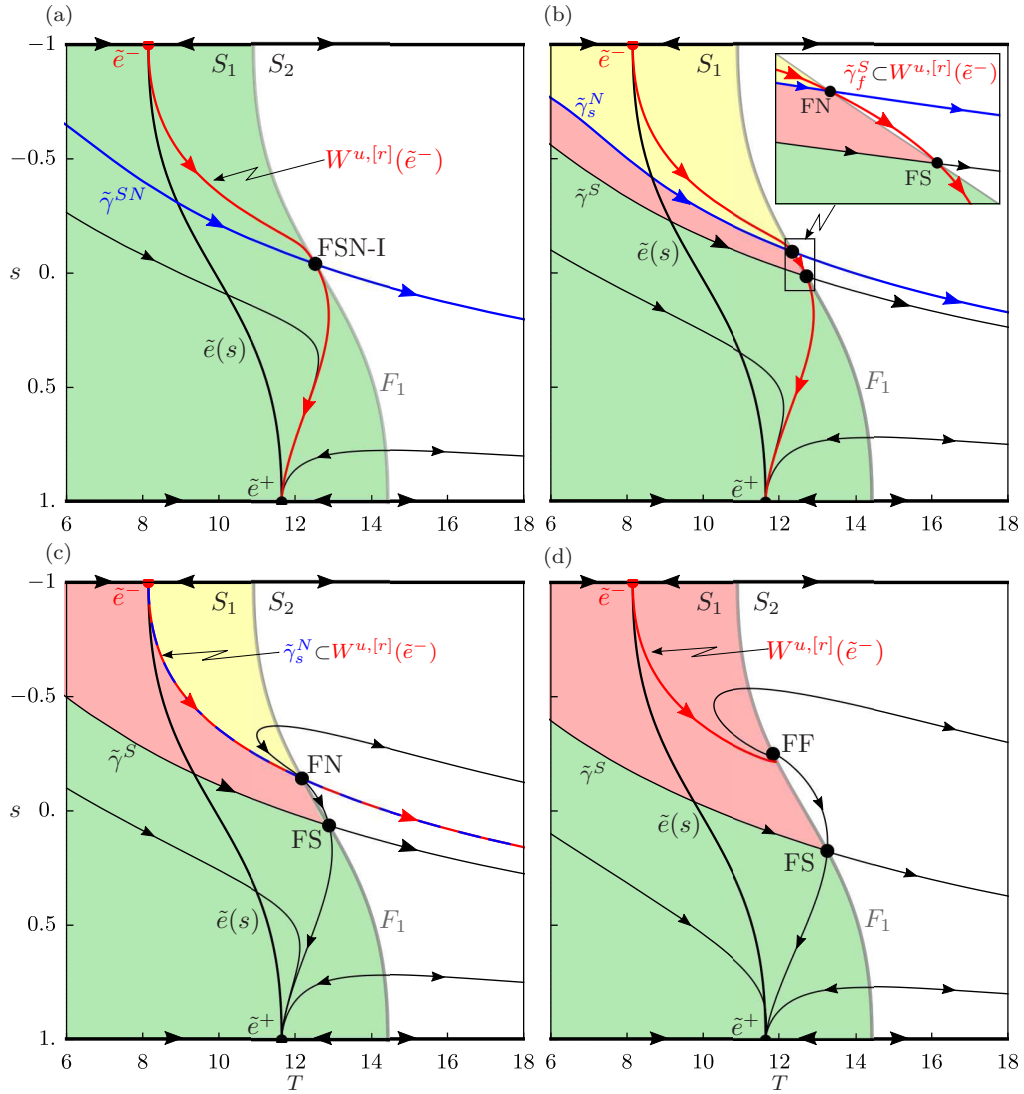


Figure 5.5: Phase portraits of the reduced problem (5.7)–(5.8) with nonlinear shift (5.2), obtained using the desingularised system (5.15)–(5.16). Shown is the complicated case with a codimension-one central heteroclinic FSN-I in (a), and a codimension-one heteroclinic orbit connecting $\tilde{e}^-$ to FN in (c). $T_a^+ = 3.5$ and the rate parameter takes values (a) $r = r_{SN} \approx 0.050086$, (b) $r \approx 0.050669$, (c) $r = r_c \approx 0.052266$, and (d) $r = 0.06$; see the black dots in the right inset of figure 5.7. System parameter values are given in Table C.1.

Similarly to the simple case, appearance of FS and FN via FSN-I gives rise to folded-saddle and folded-node singular canards, an attracting interval of jump points on F_1 between FS and FN, and the corresponding (dark red) region of solutions between $\tilde{\gamma}^S$ and $\tilde{\gamma}_s^N$ that reach one of these jump points from S_1 and cease to exist within S; see figure 5.5. In contrast to the simple case, when $r = r_{SN}$, $W^{u,[r]}(\tilde{e}^-)$ grazes F_1 at FSN-I, giving rise to a *codimension-one central heteroclinic FSN-I*; see figure 5.5 (a). In other words, the FSN-I is global. At this point tracking is lost, but R-tipping cannot occur yet. For r just above r_{SN}, $W^{u,[r]}(\tilde{e}^-)$ passes through the yellow singular funnel and crosses F_1 from S_1 to S_2 via FN; see figure 5.5 (b). Thus, $W^{u,[r]}(\tilde{e}^-)$ contains a folded-node weak singular canard. Furthermore, it attracts all other singular canards within the yellow funnel; see the relation (4.4) and [13, Th.2.2]. Then, $W^{u,[r]}(\tilde{e}^-)$ crosses F_1 back to S_1 via FS and connects to $\tilde{e}^+$; see figure 5.5 (b). Thus, $W^{u,[r]}(\tilde{e}^-)$ also contains the faux folded-saddle singular canard $\tilde{\gamma}_f^S$. For some $r = r_{Ns} > r_{SN}$, $W^{u,[r]}(\tilde{e}^-)$ and $\tilde{\gamma}_s^N$ coalesce. At this point, $W^{u,[r]}(\tilde{e}^-)$ crosses F_1 from S_1 to S_2 via FN and never returns to S_1; see figure 5.5 (c). It is only for $r > r_{Ns}$ that $W^{u,[r]}(\tilde{e}^-)$ reaches a jump point of F_1 and ceases to exist within S, or R-tips; see figure 5.4 (d).

Thus, in the complicated case for $\epsilon = 0$, there is a *critical range of* $r \in [r_{SN}, r_{Ns}]$. The minimum of the critical range is the value of r that gives a *codimension-one heteroclinic orbit* connecting $\tilde{e}^-$ to the corresponding saddle-node on F_1 along the centre eigendirection in the desingularised system (5.15)–(5.16). The maximum of the critical range is the value of r that gives a *codimension-one hetroclinic orbit* connecting $\tilde{e}^-$ to the corresponding stable node on F_1 along the strong eigendirection in (5.15)–(5.16). For r in the interior of the critical range, there is a *codimension-zero heteroclinic orbit* connecting $\tilde{e}^-$ to the corresponding stable node on F_1 along the weak eigendirection in (5.15)–(5.16).

5.2.4 The degenerate case

A natural question to ask, is what is the transition between the simple and complicated cases? It turns out that there is a special value $T_a^+ = T_{a,c}^+$ at which the transition occurs. As r is increased past r_{SN} for this special value of T_a^+, the

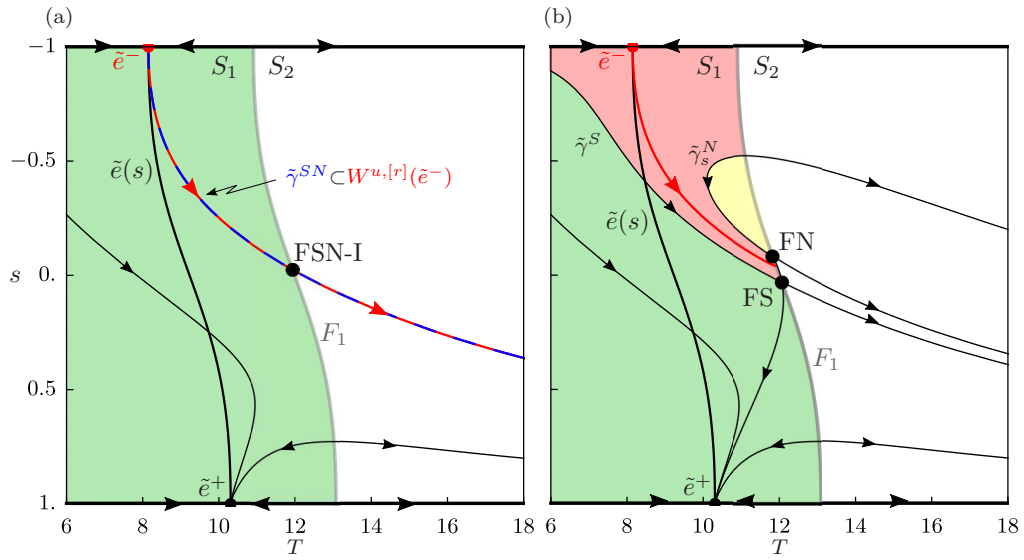


Figure 5.6: Phase portraits of the reduced problem (5.7)–(5.8) with nonlinear shift (5.2), obtained using the desingularised system (5.15)–(5.16). Shown is the degenerate case with a codimension-two non-central heteroclinic FSN-I in (a). $T_a^+ = 2.15938$ and the rate parameter takes values (a) $r = r_{SN} = r_c \approx 0.0766488$, and (b) $r \approx 0.0776488$; see the black dots in the middle inset of figure 5.7. System parameter values are given in Table C.1.

local bifurcation scenario is the same as in the simple and complicated cases. However, the global dynamics are different in that $W^{u,[r]}(\tilde{e}^-)$ interacts with the folded-saddle-node singular canard. In contrast to the simple and complicated cases, if $r = r_{SN}$ and $T_a^+ = T_{a,c}^+$, $W^{u,[r]}(\tilde{e}^-)$ and $\tilde{\gamma}^{SN}$ coalesce, giving rise to a *codimension-two non-central heteroclinic FSN-I*; see figure 5.6 (a). In other words, the FSN-I is global, but different from the complicated case. At this point, tracking is lost since $W^{u,[r_c]}(\tilde{e}^-)$ crosses F_1 from S_1 to S_2 via FSN-I; see figure 5.6 (a). For $r > r_{SN}$, $W^{u,[r]}(\tilde{e}^-)$ reaches a jump point of F_1 and ceases to exist within S, or R-tips; see figure 5.6 (b).

Thus, in the degenerate case for $\epsilon = 0$, there is an isolated *critical pair* $(T_{a,c}^+, r_c)$. This critical pair is the combination of r and T_a^+ that give a *codimension-two heteroclinic orbit* connecting $\tilde{e}^-$ to the corresponding saddle-node on F_1 along the stable eigendirection in the desingularised system (5.15)–(5.16).[3]

5.3 Bringing it Together: Unfolding of Global FSN-I

The aim of this section is twofold. First, we summarise our results from section 5.2.1 in the singular R-tipping diagram for $\epsilon = 0$ in figure 5.7. Second, we use the singular R-tipping diagram to explain the regular R-tipping diagram for $\epsilon \approx 0.064$ in figure 5.2.

The singular R-tipping diagram is obtained by the unfolding of a *codimension-two non-central heteroclinic FSN-I* in the plane (T_a^+, r) of the input parameters in the reduced problem (5.7)–(5.8). This unfolding, in turn, is obtained by the unfolding of a *codimension-two non-central saddle-node heteroclinic bifurcation* in the desingularised system (5.15)–(5.16).[4] The diagram is partitioned into three regions by two curves that are tangent at the special point of codimension-two non-central hetroclinic FSN-I, denoted $\tilde{e}$-to-FSN-I$_s$ in the middle inset. Each curve has two branches emanating from the special point.

[3]Note the difference from typical codimension-one heteroclinic orbits connecting $\tilde{e}^-$ to a saddle-node along the centre eigendirection as in the complicated case.

[4]This unfolding is reminiscent of the unfolding of a codimension-two non-central saddle-node homoclinic bifurcation in [25].

Both branches of the black curve of FSN-I were obtained by computing the saddle-node bifurcation of equilibria on F_1 in (5.15)–(5.16); we will return to this curve later. The left branch of the blue curve, denoted $\tilde{e}$-to-FS, was obtained by computing a codimension-one heteroclinic orbit connecting $\tilde{e}^-$ to the saddle on F_1 in (5.15)–(5.16). This connection gives the simple case for the reduced problem (5.7)–(5.8), where $W^{u,[r]}(\tilde{e}^-) \supset \tilde{\gamma}^S$. Thus, in the simple case, loss of (green) tracking is the onset of (red) R-tipping. Note that $\tilde{e}$-to-FS has a vertical asymptote $T_a^+ = T_a^{inst} \approx 0.423364$, which is given by condition (4.5) illustrated in figure 4.2. The right branch of the blue curve, denoted $\tilde{e}$-to-FN$_s$, was obtained by computing a codimension-one heteroclinic orbit connecting $\tilde{e}^-$ to the stable node on F_1 along the strong eigendirection in (5.15)–(5.16). This connection gives the upper boundary of the critical range in the complicated case for (5.7)–(5.8), where $W^{u,[r]}(\tilde{e}^-) \supset \tilde{\gamma}_s^N$ and the onset of (red) R-tipping does not correspond to loss of tracking. Rather, loss of tracking occurs along the right branch of the black curve, denoted $\tilde{e}$-to-FSN-I$_c$. This branch was obtained by computing a codimension-one heteroclinic orbit connecting $\tilde{e}^-$ to the saddle-node on F_1 along the centre eigendirection in (5.15)–(5.16). This connection gives the lower boundary of the critical range in the complicated case for (5.7)–(5.8), where tracking is lost because $W^{u,[r]}(\tilde{e}^-)$ grazes F_1 at FSN-I; see the red trajectory in figure 5.5(a).[5] In the (yellow) region between $\tilde{e}$-to-FSN-I$_c$ and $\tilde{e}$-to-FN$_s$, which is the interior of the critical range, there is a codimension-zero heteroclinic orbit connecting $\tilde{e}^-$ to the stable node on F_1 along the weak eigendirection in (5.15)–(5.16). This connection gives neither tracking nor R-tipping for (5.7)–(5.8). Here, $W^{u,[r]}(\tilde{e}^-)$ contains a folded-node weak singular canard, meaning that it crosses from S_1 to S_2 via FN, and also contains the faux folded-saddle singular canard, meaning that it crosses back to S_1 via FS; see the red trajectory in figure 5.5(b). The special point $\tilde{e}$-to-FSN-I$_s$, where the black and blue curves touch, corresponds to a codimension-two non-central saddle-node heteroclinic bifurcation that involves a heteroclinic orbit connecting $\tilde{e}^-$ to the saddle-node on F_1 along the stable eigendirection in (5.15)–(5.16). This connection gives the degenerate case for (5.7)–(5.8), where $W^{u,[r]}(\tilde{e}^-) \supset \tilde{\gamma}^{SN}$.

[5]The left branch of the black curve, denoted FSN-I, does not involve any global bifurcations and does not contribute to tracking-tipping transitions.

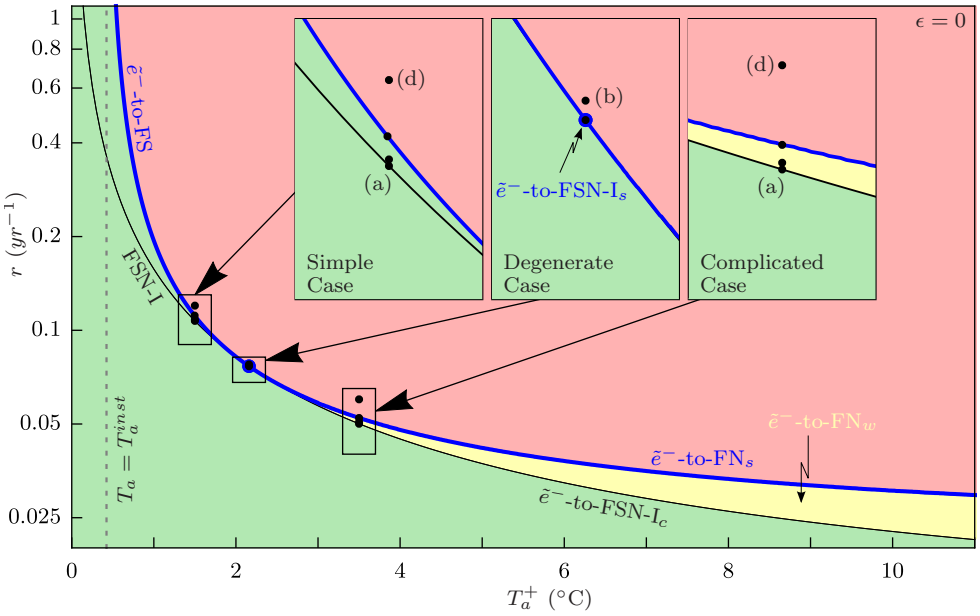


Figure 5.7: Singular R-tipping diagram for the reduced problem (5.7)–(5.8) with global warming scenario (5.2), obtained using the desingularised system (5.15)–(5.16). Regions of (green) tracking, (red) R-tipping, and (yellow) neither tracking nor R-tipping are separated by: (blue) $\tilde{e}^-$-to-FS, $\tilde{e}^-$-to-FSN-I$_s$ and $\tilde{e}^-$-to-FN$_s$, along which $W^{u,[r]}(\tilde{e}^-)$ contains the singular canards $\tilde{\gamma}^S$, $\tilde{\gamma}^{SN}$ and $\tilde{\gamma}_s^N$, respectively, and (black) $\tilde{e}^-$-to-FSN-I$_c$, along which $W^{u,[r]}(\tilde{e}^-)$ contains the weak folded saddle-node singular canard. System parameter values are given in Table C.1.

Next, we use the singular R-tipping diagram in figure 5.7, together with rigorous results on persistence of singular canards as maximal canards for $0 < \epsilon \ll 1$ [92, 52, 51, 106, 101], to explain the regular R-tipping diagram in figure 5.2.

In the simple case, the folded-saddle singular canard $\tilde{\gamma}^S$ perturbs to a family of canards when $0 < \epsilon \ll 1$. The family contains one maximal canard, namely the *folded-saddle maximal canard* $\tilde{\gamma}^S_\epsilon$, and associated canards "without head" and "with head" [92]. Thus, a folded-saddle maximal canard explains the simple part of the regular R-tipping diagram at lower values of T_a^+, including the (cyan) critical range and the vertical asymptote of the blue curve of maximal canards. In the context of excitable systems, we use Definition 4.1.3(ii) to relate a family of canards "without head" associated with a codimension-one normally hyperbolic repelling slow manifold near FS to a new type of excitability quasithreshold; see also [112, 68].

In the complicated case, the perturbed dynamics for $0 < \epsilon \ll 1$ are far less straightforward due to the presence of many folded-node maximal canards in addition to the folded-saddle maximal canard. The number and type of folded-node maximal canards depend on the distance between FN and FS, and on the ratio of the weak and strong eigenvalues of FN, denoted $\mu \in (0, 1)$. The folded-node strong singular canard $\tilde{\gamma}^N_s$ perturbs to a family of canards for all $\mu \in (0, 1)$. This family contains the *folded-node strong maximal canard* $\tilde{\gamma}^N_{s,\epsilon}$ and associated canards "without head" and "with head". Depending on μ, the family of folded-node weak singular canards from the singular funnel may perturb to a single *folded-node weak maximal canard* $\tilde{\gamma}^N_{w,\epsilon}$ [106, 109]. Additionally, there can be a number of *secondary folded-node maximal canards* that lie between $\tilde{\gamma}^N_{s,\epsilon}$ and $\tilde{\gamma}^N_{w,\epsilon}$ [92, 106, 30]. Furthermore, the interplay between the folded node and the folded saddle can give rise to *real-faux canards* described in [76, 101], that are a perturbation of the red trajectory from figure 5.5(b), and to *composite canards* identified in [76], that follow the folded-saddle maximal canard and then 'switch' to and follow one of the folded-node maximal canards. For example, we have checked that as r is increased for a fixed $T_a^+ \gtrsim 9.3°\text{C}$ in figure 5.2, $W^{u,[r]}(\tilde{e}^-)$ coalesces with a secondary folded-node canard at the bottom boundary of the R-tipping tongue, then with a composite canard at the upper

boundary of the tongue, and finally with the folded-node strong maximal canard at the bottom boundary of the main R-tipping region.[6] Thus, it is folded-node maximal canards and composite canards, together with the associated canards "without head" and "with head", that give rise to the complicated tracking-tipping transitions including R-tipping tongue(s), at higher values of T_a^+. In the context of excitable systems, we use Definition 4.1.3(ii) to relate a family of canards "without head" associated with a codimension-one normally hyperbolic repelling slow manifold near FSN-I to a new type of excitability quasithreshold. This quasithreshold is expected to have a very complicated shape as indicated by the computations of slow manifolds in [28, 77].

5.4 Secondary and Composite Canards

In this section we discuss maximal secondary and composite canards which form the boundaries of the R-tipping tongue in figure 5.2.

5.4.1 Secondary Canards

Maximal canards which cross from $S_{1,\epsilon}$ to $S_{2,\epsilon}$ do so via transverse intersections of $S_{1,\epsilon}$ and $S_{2,\epsilon}$. In general such transverse intersections arise as perturbations for $0 < \epsilon \ll 1$ of folded singularities which exist for $\epsilon = 0$. Close to a folded node FN, additional intersections may arise depending on the ratio of the weak and strong eigenvalues of FN denoted $\mu \in (0, 1)$. In particular, for $\mu^{-1} > 3$, new transverse intersections are created at odd integer values of μ^{-1} [109]. These additional transverse intersections arise from twisting of $S_{1,\epsilon}$ to $S_{2,\epsilon}$ close to FN for $0 < \epsilon \ll 1$ [28, 30], and the solutions which cross from $S_{1,\epsilon}$ to $S_{2,\epsilon}$ via these intersections are called *secondary folded-node maximal canards*, or simply *secondary canards*.

It is also possible for additional intersections to arise close to FS when FS and FN are close, such as near a FSN-I bifurcation. Such intersections give rise

[6] For higher T_a^{max}, we found additional R-tipping tongues, not shown in the figures, whose boundaries involve different secondary and composite canards; see also [76, Fig.4].

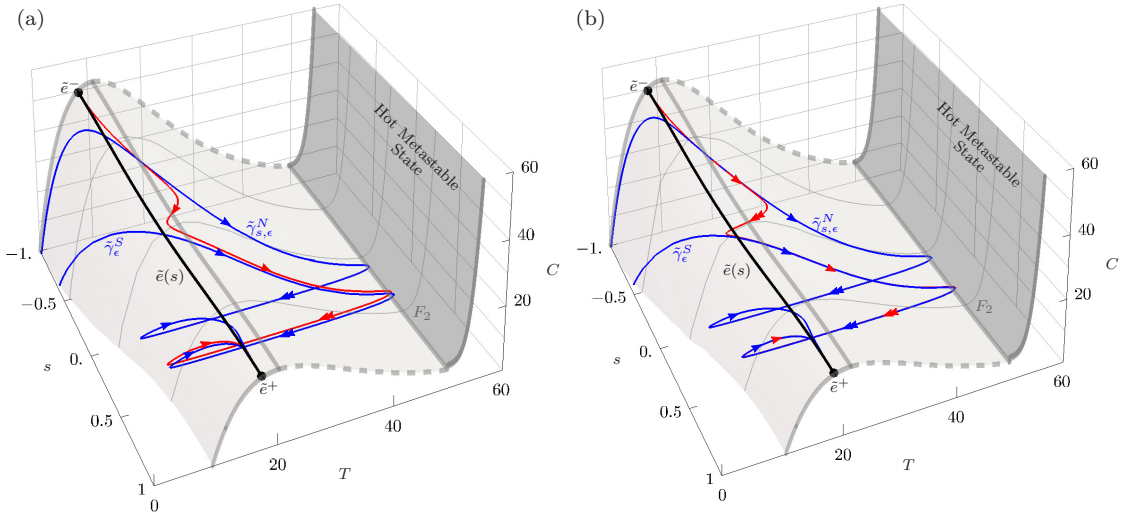


Figure 5.8: (a) (red) The unstable invariant manifold $W^{u,[r]}(\tilde{e}^-)$ of the saddle $\tilde{e}^-$ for the compactified system (7.8)–(7.10) with global warming scenario (5.2) with $T_a^+ = 9.3°\text{C}$ and $r \approx 0.0324705307595$ and containing a secondary canard, and (b) with $T_a^+ = 10.4°\text{C}$ and $r \approx 0.03182405106825$ and containing a composite canard. Included for reference are (blue) the folded saddle maximal canard $\tilde{\gamma}^S_\epsilon$, (blue) the primary folded-node maximal canard $\tilde{\gamma}^N_{s,\epsilon}$ and (grey) the critical manifold S defined in (5.3). System parameter values are given in Table C.1

to *secondary faux canards*. While we do not discuss this case here, an in-depth exploration of this phenomenon is available in [67].

The distinguishing feature of secondary folded-node maximal canards is that they perform at least one but possibly multiple rotations near F_1 before travelling along $S_{2,\epsilon}$ for as long as it exists; see figure 5.8(a). Such rotations have been found to play a role in mixed-mode oscillations [30, 102], and as they occur along curved sections of $S_{1,\epsilon}$ and $S_{2,\epsilon}$, they are governed by slow dynamics. We note also that secondary folded-node maximal canards have associated secondary canards "with head", and $W^{u,[r]}(\tilde{e}^-)$ contains such secondary canards "with head" in the interior of the R-tipping tongue.

5.4.2 Composite Canards

In contrast to secondary canards, composite canards do not arise from additional transverse intersections of $S_{1,\epsilon}$ and $S_{2,\epsilon}$. Instead, they arise from the interaction of a canard "without head" associated to the folded-node strong maximal canard $\tilde{\gamma}^N_{s,\epsilon}$ and the folded saddle maximal canard $\tilde{\gamma}^N_{s,\epsilon}$. A composite canard follows $\tilde{\gamma}^N_{s,\epsilon}$ for some time, before following a fast segment to $S_{1,\epsilon}$ as a canard "without head". This fast segment is directed toward $\tilde{\gamma}^S_\epsilon$, and the composite canard subsequently follows $\tilde{\gamma}^S_\epsilon$, following $S_{2,\epsilon}$ for as long as it exists; see figure 5.8(b). In summary, a composite canard consists of two distinct maximal canard segments, which are joined by a fast segment. For a further discussion of composite canards, we refer to [76, 117].

The difference between composite canards and secondary canards can be difficult to distinguish, as each appears to rotate about F_1 before travelling the length of $S_{2,\epsilon}$. The key distinction is that for a secondary canard, this is a genuine rotation as the trajectory travels slowly along $S_{1,\epsilon}$ and $S_{2,\epsilon}$. Meanwhile for a composite canard, the motion in the negative T direction is a fast segment. This distinction is highlighted in figure 5.9, where we compare the time trace of T for a secondary canard against the time trace of T for a composite canard. For the secondary canard, the speed at which $T(t)$ increases during the rotation is comparable to the speed at which is decreases; this can be seen by comparing the slopes of the increase and decrease in the slow rotation of

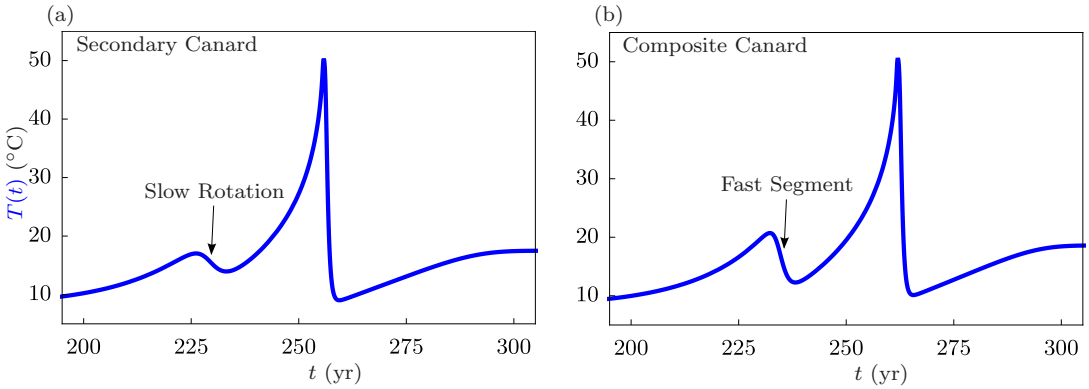


Figure 5.9: (a) Time trace of T for a secondary canard, where the initial motion in the negative T direction is a component of a slow rotation. (b)Time trace of T for a composite canard, where the initial motion in the negative T direction is a fast segment linking two maximal canards.

figure 5.9(a). This is because the slow rotation is caused by continuous slow motion along slow manifolds. In contrast, for the composite canard the speed at which $T(t)$ decreases during the fast segment is faster than that at which it increases just before; compare the slopes just before and during the fast segment of figure 5.9(b). This is because for the composite canard the rotation about F_1 consists of slow motion along a slow manifold, followed by the fast segment between slow manifolds.

5.5 R-tipping Tongues

Figure 5.10 shows that as T_a^+ is increased beyond the range shown in figure 5.2, an additional R-tipping tongue is observed in the (T_a^+, r) parameter space. This additional R-tipping tongue arises from the bifurcation of additional secondary canards caused by the twisting of $S_{2,\epsilon}$ close to FN. In general, for systems where R-tipping is connected to the unfolding of a global FSN-I, such R-tipping tongues will accumulate from below as additional secondary canards are created.

To better understand the twisting of slow manifolds near FN and how it gives rise to secondary canards, composite canards, and R-tipping tongues, we implement the numerical continuation methods presented in [28, 30] in order to

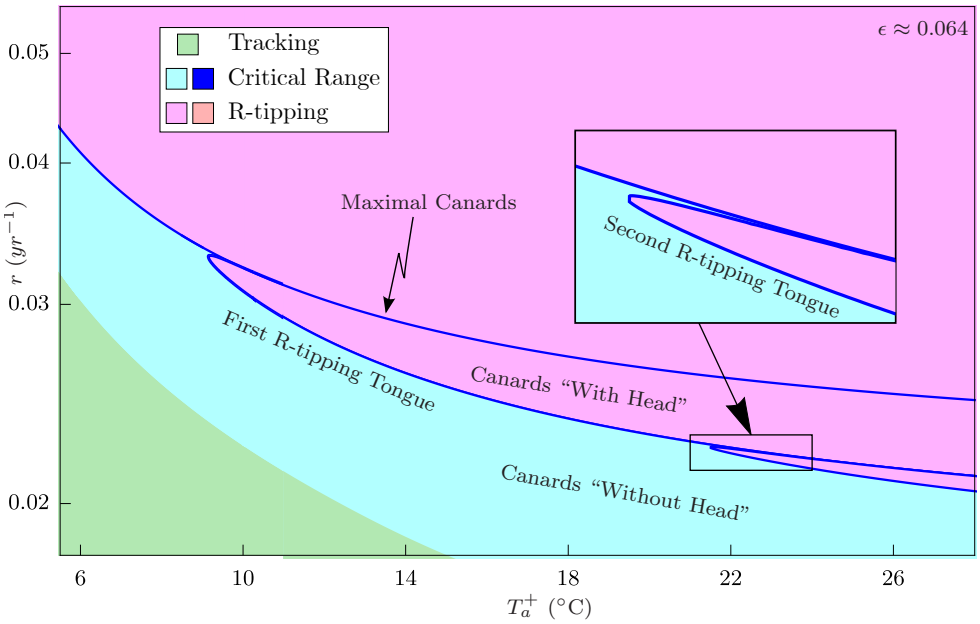


Figure 5.10: The R-tipping diagram for the nonautonomous system (2.3)–(2.4) with global warming scenario (5.1) of figure 5.2, extended to higher T_a^+ to show the second R-tipping tongue. Shown are regions of (green) tracking, (cyan, blue) critical range, and (magenta, red) R-tipping from $\tilde{e}^-$. System parameter values are given in Table C.1.

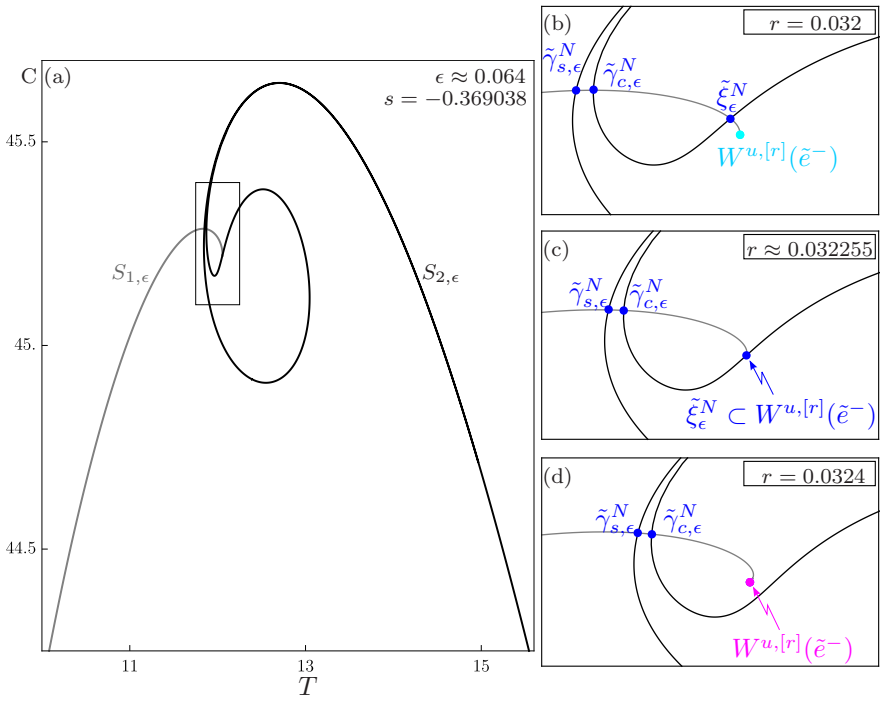


Figure 5.11: (a) Cross section of the (grey) attracting slow manifold $S_{1,\epsilon}$ and the (black) repelling slow manifold $S_{2,\epsilon}$ in the plane $s = -0.369038$ for $T_a^+ = 9.3$ and $r = 0.32255$, showing complicated twisting close to the folded node FN giving rise to (blue) multiple intersections of $S_{1,\epsilon}$ and $S_{2,\epsilon}$ corresponding to maximal canards. Panels (b)–(d) show a zoomed view of the intersections as r is increased across the bottom of the R-tipping tongue of figure 5.2. (b) View for $r = 0.032$ showing (blue) three intersections corresponding to the folded-node strong maximal canard $\tilde{\gamma}^N_{s,\epsilon}$, a composite canard $\tilde{\gamma}^N_{c,\epsilon}$, and a folded-node secondary canard $\tilde{\xi}^1_\epsilon$ along with (cyan) $W^{u,[r]}(\tilde{e}^-)$ which is a canard without head. (c) View for $r \approx 0.032255$, where (blue) $\tilde{\xi}^1_\epsilon$ is contained in $W^{u,[r]}(\tilde{e}^-)$. (d) View for $r \approx 0.0324$, where (magenta) $W^{u,[r]}(\tilde{e}^-)$ is a canard with head and $\tilde{\xi}^1_\epsilon$ has been annihilated in an infinite-time bifurcation in panel (c).

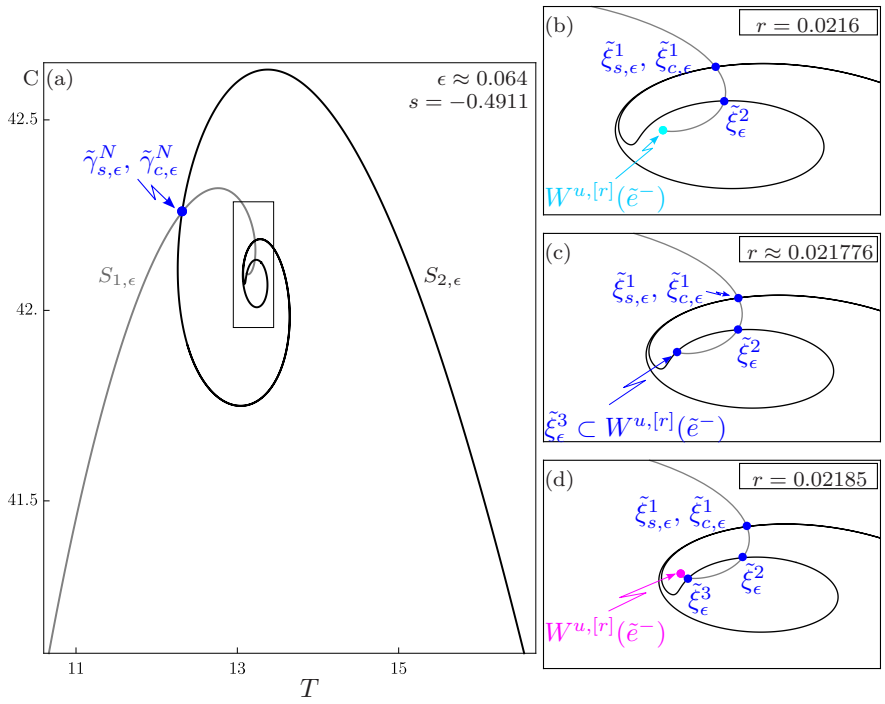


Figure 5.12: (a) Cross section of the (grey) attracting slow manifold $S_{1,\epsilon}$ and the (black) repelling slow manifold $S_{2,\epsilon}$ in the plane $s = -0.4911$ for $T_a^+ = 23$ and $r = 0.021776$, showing complicated twisting close to the folded node FN giving rise to multiple intersections of $S_{1,\epsilon}$ and $S_{2,\epsilon}$ corresponding to maximal canards including (blue) $\tilde{\gamma}^N_{s,\epsilon}$ and $\tilde{\gamma}^N_{c,\epsilon}$ which are exponentially close to each other. Panels (b)–(d) show a zoomed view of the other intersections as r is increased across the bottom of the second R-tipping tongue of figure 5.10. (b) View for $r = 0.0216$ showing (blue) three intersections corresponding to the secondary canards $\tilde{\xi}^1_\epsilon$ and $\tilde{\xi}^2_\epsilon$, as well as the *composite secondary canard* $\tilde{\gamma}^1_{c,\epsilon}$. Also shown is (cyan) $W^{u,[r]}(\tilde{e}^-)$ which is a canard without head. (c) View for $r \approx 0.021776$, where (blue) an additional secondary canard $\tilde{\xi}^3_\epsilon$ is contained in $W^{u,[r]}(\tilde{e}^-)$. (d) View for $r \approx 0.0324$, where (magenta) $W^{u,[r]}(\tilde{e}^-)$ is a canard with head.

numerically compute $S_{1,\epsilon}$ and $S_{2,\epsilon}$ close to the folded node FN. Figure 5.11(a) shows a cross section of (grey) $S_{1,\epsilon}$ and (black) $S_{2,\epsilon}$ in the plane:

$$\Sigma^{FN} := \{(T, C, s) \ : \ s = -0.369038\}, \tag{5.17}$$

which contains FN when $\epsilon = 0$. We choose (T_a^+, r) from along the bottom of the left R-tipping tongue in figure 5.10 (which is the R-tipping tongue shown in figure 5.2), when $W^{u,[r]}(\tilde{e}^-)$ contains a secondary canard $\tilde{\xi}_\epsilon^N$. The slow manifolds intersect transversely in three places indicated in blue, corresponding to the folded-node strong maximal canard $\tilde{\gamma}_{s,\epsilon}^N$, a composite canard $\tilde{\gamma}_{c,\epsilon}^N$, and a folded-node secondary canard $\tilde{\xi}_\epsilon^N$ which is contained in $W^{u,[r]}(\tilde{e}^-)$.

As $W^{u,[r]}(\tilde{e}^-)$ corresponds to a pullback attractor for the non-autonomous system, it is found at the edge of the attracting manifold in figure 5.11. The left R-tipping tongue observed in 5.10 is caused by the boundary of $S_{1,\epsilon}$, which is given by $W^{u,[r]}(\tilde{e}^-)$, crossing the twisted repelling slow manifold $S_{2,\epsilon}$. Furthermore, as r increases and $W^{u,[r]}(\tilde{e}^-)$ crosses $S_{2,\epsilon}$, the intersection is annihilated and the corresponding maximal canard disappears in what is termed an infinite-time bifurcation of canards in [77]. The term infinite-time bifurcation refers to the fact that at the moment of the bifurcation, the canard is contained in $W^{u,[r]}(\tilde{e}^-)$ and so connects to the saddle $\tilde{e}^-$.

For larger T_a^+, the repelling manifold $S_{2,\epsilon}$ undergoes additional twisting, giving rise to additional intersections of $S_{1,\epsilon}$ and $S_{2,\epsilon}$ corresponding to additional secondary canards as discussed in section 5.4; see figure 5.12. These secondary canards undergo additional rotations near F_1, and give rise to additional R-tipping tongues in the (T_a^+, r) plane; see figure 5.10.

5.6 Approximating the Critical Rate

For $T < T^*$, the non-monotone respiration function $R_s^*(T)$ introduced in section 2.3 is approximated with exponentially small error by $R_s^\dagger(T)$ used in [112]. It follows that the formula for approximating the critical rate derived in [112] may be applied to the current problem. Following [112], we first assume an initial condition $(C_s(0), T_s(0), s(0)) \in S_1$, sufficiently close to F_1, and that R-

tipping occurs due to the crossing of a folded saddle maximal canard γ_ϵ^S. Then the critical rate of warming v^c may be approximated by:

$$v^c = \frac{r_0}{2B\alpha} \exp\left(\frac{(1 + B + \sqrt{1+B^2})(\alpha T_a^\nu(s(0)) + 1) - \alpha T_a^\nu(s(0))}{B + \sqrt{1+B^2}} \right) + E_{lin} + E_\epsilon,$$
$$B = \left(2(1 - \alpha A \Pi \lambda^{-1})\right)^{-1},$$

where E_{lin} accounts for the deviation of the folded saddle singular canard γ^S (or correspondingly, the stable manifold of the saddle in the desingularised system) from its linearisation, and E_ϵ is a correction for a non-zero ϵ. We note that the critical rate of warming v^c is a physical quantity, that is a critical value of dT_a/dt, and as such differs from the rate parameter r which is examined in this study.

Following [112], we assume $2B^2 \gg 1$. Additionally, we assume the system begins near $\tilde{e}^-$ and $T_a^- = 0$ meaning the condition simplifies to:

$$v^c \approx \frac{r_0}{2B\alpha} \exp(1) \tag{5.18}$$

The critical rate of warming v^c as derived applies to a linear increase in T_a at a constant rate. As we consider a nonlinear ramp, we set the critical rate of warming v^c equal to the maximum rate of change of (5.1) to obtain a critical value for the rate parameter r. It follows from section 3.2.2 that for any time t the rate of change of atmospheric temperature T_a may be written:

$$\frac{dT_a(rt)}{dt} = \frac{2rT_a}{T_a^+}\left(T_a^+ - T_a\right). \tag{5.19}$$

For a given r and T_a^+, the right hand side of (5.19) is maximised by setting $T_a = T_a^+/2$ to obtain:

$$\sup_t \dot{T}_a(rt) = \frac{r(T_a^+)}{2}.$$

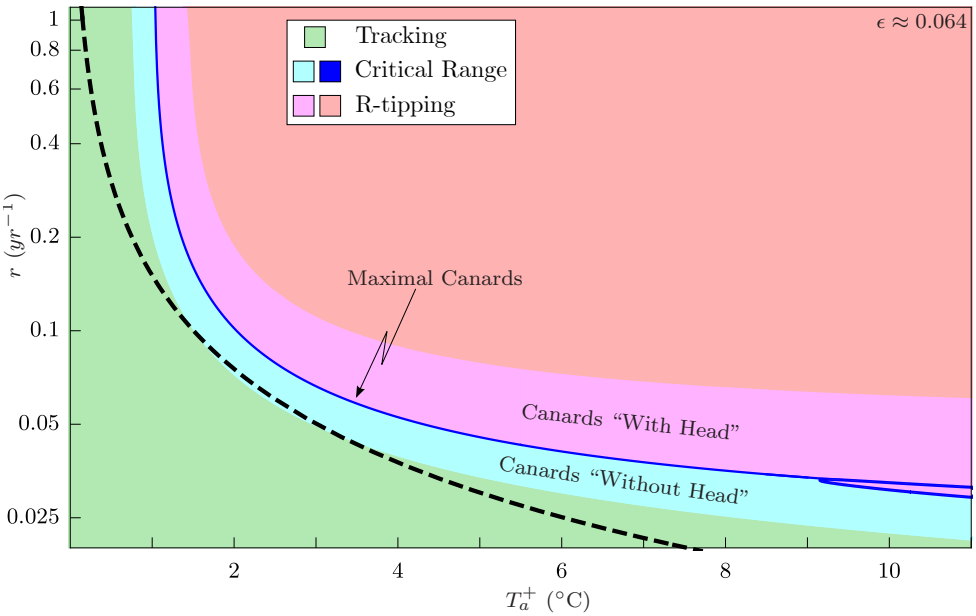


Figure 5.13: The R-tipping diagram of figure 5.2 with (black, dashed) the approximate critical rate (5.20) overlaid. For more information see the caption of figure 5.2

We set $v_c = \sup_t \dot{T}_a(rt)$, and rearrange to obtain an approximate critical rate:

$$r^c = \frac{2v^c}{T_a^+} \approx \frac{2\,R_s^\dagger(1/\alpha)}{(T_a^+)^2 B\alpha}. \tag{5.20}$$

Figure 5.13 shows this approximation of the critical value of the rate parameter r overlaid with the R-tipping diagram from figure 5.2. For smaller T_a^+, the deviation of the approximation may be explained by the sources of error E_{lin} and E_ϵ. Additionally for larger T_a^+, R-tipping occurs due to the crossing of a folded-node primary maximal canard $\tilde{\gamma}_{s,\epsilon}^N$, violating one of the assumptions in the derivation. We note however that the onset of loss of tracking, i.e. the lower bound of the critical range of r is well approximated for $2 < T_a^+ < 4$. This is within the range of uncertainty of temperature projections of CMIP5 models under an RCP2.6 scenario. Figure 5.13 shows the approximate critical rate (5.20) for varying T_a^+. The approximate critical rate most accurately predicts loss of tracking close to $\tilde{e}$-to-FSN-I$_s$. This may be attributed to the fact that the equilibrium $\tilde{e}^-$ is assumed to be close to the fold F_1, so that R-tipping

should occur shortly past the folded saddle-node bifurcation. From figure 5.7 we know that close to $\tilde{e}$-to-FSN-I_s, we expect loss of tracking to occur close to the folded bifurcation.

Finally, the numerical value of the critical rate of warming 5.18 is:

$$v^c \approx 0.0752948, \tag{5.21}$$

which is only slightly larger than the largest rates shown for Arctic regions in figure 1.1. We note however, that many of these regions have average annual temperatures below 0°C. In the soil-carbon model we examine, for initial atmospheric temperature below 0° the system will R-tip for lower rates.

Chapter 6

R-tipping mechanisms for Summer Heatwaves

6.1 R-tipping and Canards in The Compactified System

The R-tipping instability in figure 2.2 arises because time-variation of the atmospheric temperature T_a interacts with the fast timescale of soil temperature T. Thus, we work with the layer problem for the ensuing 2-fast 1-slow compactified system (7.8)–(7.10) to uncover the underlying dynamical mechanisms.

As a model of a summer heatwave, we consider a fast impulse rising from $T_a^{min} = 0°\text{C}$ to a given $T_a^{max} > 0°\text{C}$ and then dropping back to 0°C with the rate parameter $r \lesssim 1/\epsilon$:

$$T_a(rt) = T_a^{max} \operatorname{sech}(rt), \tag{6.1}$$

that decays exponentially with the decay coefficient $\rho = 1$ as per definition 3.1.1; see figure 5.1(b). We fix the compactification parameter $\nu = 1/2$ and consider system (7.8)–(7.10) with

$$T_a^{\nu}(s) = T_a^{\frac{1}{2}}(s) = \frac{2\,T_a^{max}\,(1-s)^2}{(1+s)^4 + (1-s)^4}, \tag{6.2}$$

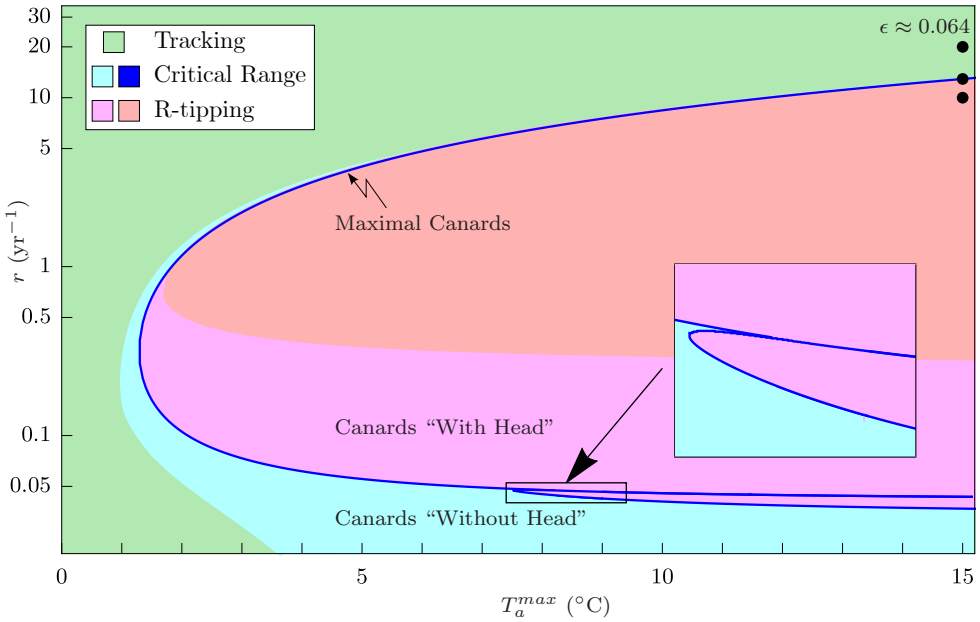


Figure 6.1: R-tipping diagram for nonautonomous system (2.3)–(2.4) with summer heatwave (6.1), in the plane of the impulse amplitude T_a^{max} and the rate parameter r, for $\epsilon \approx 0.064$. Shown are regions of (green) tracking, (cyan, blue) critical range, and (magenta, red) R-tipping from $\tilde{e}^-$. System parameter values are given in Table C.1.

which is obtained by applying the inverse compactification transformation (3.7) to (6.1). Our choice of ν ensures that the corresponding system (7.8)–(7.10) is at least C^1-smooth on the extended phase space $\mathbb{R}^2 \times [-1, 1]$; see Sec. 3.2 and the references therein.

To give a full overview of transitions from tracking to R-tipping for impulse inputs, and to make connections to Section 5, we plot an R-tipping diagram in the plane (T_a^{max}, r) of the input parameters in figure 6.1 for a wide range of the rate parameter r. The diagram was obtained by computing $W^{u,[r]}(\tilde{e}^-)$ in system (7.8)–(7.10) for different values of T_a^{max} and r, and using Definitions 4.1.1–4.1.3 to identify different dynamical regions for system (2.3)–(2.4). We note that the shape of the R-tipping region in figure 6.1 is rather different to that obtained in figure 5.2. There are two R-tipping tongues, one large akin to that in [72, Sec.6] and one small akin to that in figure 5.2, each enclosing a separate (magenta, red) region of R-tipping. These two tongues give rise to

up to three critical ranges of r for a fixed T_a^{max}. Furthermore they are reminiscent of resonance tongues for time-periodic inputs [61] in the sense of a strongly enhanced response to external inputs with 'optimal' timing. Most importantly, there are multiple tracking-tipping transitions for a large enough shift magnitude T_a^{max}. The lower part of the diagram corresponds to slow impulses that last for decades. The tracking-tipping transitions found in this part occur during the rise of the impulse $T_a(rt)$, and turn out to be of the same type as the tracking-tipping transitions described in Sec. 5. The upper part of the diagram corresponds to fast impulses and is the focus of this section. Specifically, the rate parameter r in the range of 10 to 15 yr^{-1} gives a pulse duration in the range of 3 to 2 months, in line with realistic summer heatwaves [75].[1] Thus, the single tipping-tracking transition found in the upper part of the diagram quantifies the intensity and duration of summer heatwaves that trigger R-tipping to the hot metastable state in the soil-carbon model (2.3)–(2.4).

To gain geometric insight into the R-tipping instability caused by a summer heatwave, we consider (6.1) with $r \lesssim 1/\epsilon$, and plot in figure 6.2 the unstable manifold $W^{u,[r]}(\tilde{e}^-)$ for a fixed $T_a^+ = 15°\mathrm{C}$ and three different rates $r_1 > r_2 > r_3 > 0$ (see the black dots in figure 6.1). Additionally, for reference, we include useful geometric objects. One is the (light gray) plane of constant C fixed at the equilibrium soil-carbon concentration $C^e(0)$ for the past and future limit systems. The other is the (dark gray) critical manifold for (7.8)–(7.10),

$$S = S^- \cup S^+, \tag{6.3}$$

which now consists of two disconnected one-dimensional components

$$S^{\mp} = \{(T, C, s) \ : \ f_1(T, C, 0) = 0, \ s = \mp 1\}\,. \tag{6.4}$$

Specifically, $S^- = S_1^- \cup F_1^- \cup S_2^- \cup F_2^- \cup S_3^-$ is the critical manifold of the past limit system (3.1)–(3.2) with $T_a^- = 0°\mathrm{C}$, embedded in the compactified phase space where it gains one unstable direction. Similarly, $S^+ = S_1^+ \cup F_1^+ \cup S_2^+ \cup F_2^+ \cup S_3^+$

[1] The pulse duration is obtained using the formula $2\ln(2+\sqrt{3})/r \approx 2.6/r$ for the full width at half maximum of the hyperbolic secant $\mathrm{sech}(rt)$.

is the critical manifold of the future limit system (3.3)–(3.4) with $T_a^+ = 0°\text{C}$, embedded in the compactified phase space where it gains one stable direction. Thus, the attracting branch S_3^+ of $S^+$is the hot metastable state. For tracking-tipping transitions, we will be interested in the hyperbolic saddle branch S_2^+ of S^+.

Figure 6.2 shows that, as r is *decreased* (meaning the duration of the heat-wave is *increased*), tracking by (green) $W^{u,[r_1]}(\tilde{e}^-)$ is lost via canard trajectories, including the maximal canard contained in (blue) $W^{u,[r_2]}(\tilde{e}^-)$ that approaches S_2^+ and moves along S_2^+ for the longest time. This is followed by R-tipping at *lower* r as shown by (red) $W^{u,[r_3]}(\tilde{e}^-)$ that visits the hot metastable state $S_{3,\epsilon}^+$ before connecting to $\tilde{e}^+ \in S_{1,\epsilon}^+$. Since $W^{u,[r]}(\tilde{e}^-)$ remains near $C = C^e(0)$ until $s(t) \approx 1$, it should be possible to explain the R-tipping instability caused by a summer heatwave in terms of the fast dynamics of a suitably chosen layer problem for (7.8)–(7.10).

6.2 The Layer Problem

The suitable layer problem for the 2-fast 1-slow system (7.8)–(7.10) with a summer heatwave (6.2) is obtained by rewriting (7.8)–(7.10) in terms of the fast time $\tau = t/\epsilon$, setting $\epsilon = 0$ while keeping ϵr non-zero, and setting $C = C^e(0)$, which gives:

$$\frac{dT}{d\tau} = f_1(T, C^e(0), T_a^{\frac{1}{2}}(s)), \tag{6.5}$$

$$\frac{ds}{d\tau} = \frac{\epsilon r}{4}(1 - s^2). \tag{6.6}$$

This system describes the evolution of the fast variables T and s in the fast time τ on the two-dimensional *layer*,

$$\tilde{L} = \{(T, C) \ : \ C = C^e(0)\},$$

shown in figure 6.2. Crucially, the layer problem (6.5)–(6.6) has six equilibria. Two of these equilibria, namely the saddle $\tilde{e}^- \in S_1^-$ and the sink $\tilde{e}^+ \in S_1^+$, are

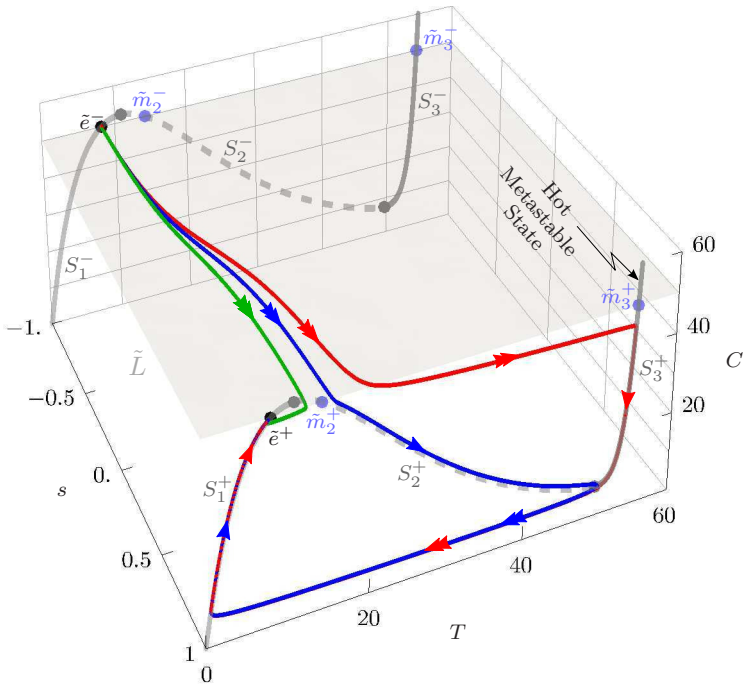


Figure 6.2: (Colour) The unstable invariant manifold $W_\nu^{u,[r]}(\tilde{e}^-)$ of the saddle $\tilde{e}^-$ for the compactified system (7.8)–(7.10) with $\epsilon \approx 0.064$, summer heatwave (6.2) with $T_a^{max} = 15°\text{C}$, and three different values of the rate parameter: (green) $r = 20$, (blue) $r \approx 12.9123$, and (red) $r = 10$; see the black dots in figure 6.1. Included for reference are (dark grey) the two disconnected components S^- and S^+ of the critical manifold, (light grey) the layer $\tilde{L}$ defined by $C = C^e(0)$, and (light blue) four new equilibria $\tilde{m}_2^\pm$ and $\tilde{m}_3^\pm$ for the layer problem (6.5)–(6.6). System parameter values are given in Table C.1.

the equilibria of the compactified system (7.8)–(7.10). The four new equilibria, that do not exist in (7.8)–(7.10), are found at the intersections of $\tilde{L}$ with $S_{2,3}^\pm$. These are: the source $\tilde{m}_2^- \in S_2^-$, the saddle $\tilde{m}_3^- \in S_3^-$, the saddle $\tilde{m}_2^+ \in S_2^+$, and the sink $\tilde{m}_3^+ \in S_3^+$; see the (blue) dots in figure 6.2.

In the the layer problem (6.5)–(6.6), the question of loss of tracking boils down to whether or not $W^{u,[r]}(\tilde{e}^-)$ connects to the saddle $\tilde{m}_2^+$. Thus, the saddle $\tilde{m}_2^+$ is the "singular edge state" described in the introduction. Before we address this question directly in figure 6.4, we provide more insight into R-tipping caused by a summer heatwave. We recognise that the layer problem (6.5)–(6.6) itself can evolve on two different time scales. Specifically, we rewrite (6.5)–(6.6) in

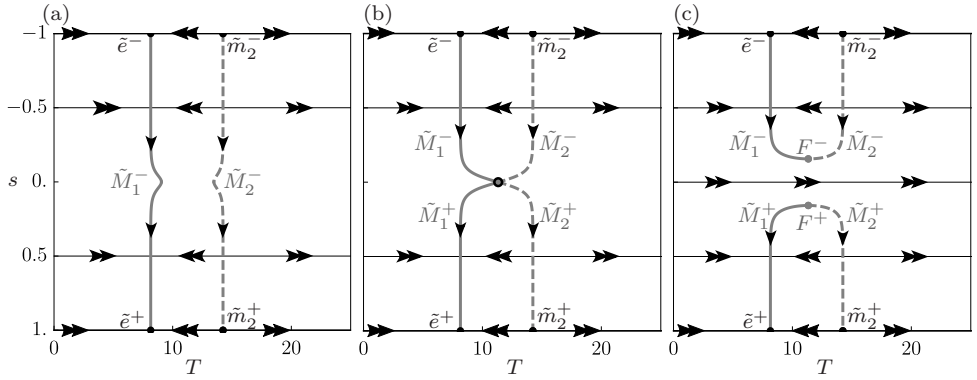


Figure 6.3: Phase portraits of the reduced problem for the layer problem (6.5)–(6.6) with impulse (B.2). Shown are (gray) different branches of the critical manifold $\tilde{M}$ defined in (6.7) for (a) $T_a^{max} = 0.2$, (b) $T_a^{max} = T_a^{inst} \approx 0.423364$ and (c) $T_a^{max} = 5$. Single arrows indicate the fast time $\tau = t/\epsilon$, and double arrows indicate the intermediate time $u = rt$. System parameter values are given in Table C.1. We use (B.2) instead of (6.2) to more easily see the separation of the branches of $\tilde{M}$.

terms of the intermediate time $u = rt$, take the limit $\epsilon r \to 0$, and consider the critical manifold

$$\tilde{M} = \left\{ (T, s) \ : \ 0 = f_1(T, C^e(0), T_a^{\frac{1}{2}}(s)) \right\} \subset \tilde{L}, \tag{6.7}$$

of the reduced problem (not shown) for the layer problem (6.5)–(6.6). It turns out that the number of branches[2] of $\tilde{M}$ depends on T_a^{max} and changes at $T_a^{max} = T_a^{inst} \approx 0.423364$, which is given by condition (4.5) illustrated in figure 4.2. If $T_a^{max} < T_a^{inst}$, there are three hyperbolic branches of $\tilde{M}$, two attracting, $\tilde{M}_1$ and $\tilde{M}_3$, and one repelling, $\tilde{M}_2$. In figure 6.3(a), we show only $\tilde{M}_1$ and $\tilde{M}_2$, where the interesting change occurs.[3] If $T_a^{max} = T_a^{inst}$, $\tilde{M}_1$ and $\tilde{M}_2$ become degenerate in a non-hyperbolic (transcritical) point at $s = 0$; see figure 6.3(b). If $T_a^{max} > T_a^{inst}$, $\tilde{M}_1$ and $\tilde{M}_2$ split up into four different branches, two attracting, $\tilde{M}_1^-$ and $\tilde{M}_1^+$, and two repelling, $\tilde{M}_2^-$ and $\tilde{M}_2^+$. Furthermore, $\tilde{M}_1^\pm$ and $\tilde{M}_2^\pm$ meet at non-hyperbolic fold points $F^\pm$, respectively; see figure 6.3(c). It is clear

[2]In a certain sense, a branch of $\tilde{M}$ corresponds to a moving equilibrium for the layer problem (6.5)–(6.6).

[3]$\tilde{M}_3$ is shown in figure 6.4.

from figure 6.3(a) that tracking in the layer problem (6.5)–(6.6) is guaranteed if $T_a^{max} < T_a^{inst}$, owing to the presence of the uninterrupted attracting manifold $\tilde{M}_1$ connecting $\tilde{e}^-$ to $\tilde{e}^+$. It is also clear from figure 6.3(c) that $T_a^{max} > T_a^{inst}$ is necessary for R-tipping to occur, owing to the presence of a 'gap' in $\tilde{M}_1$, which allows trajectories to jump from $\tilde{M}_1^-$ via F^- to $\tilde{M}_3$. Furthermore, it is intuitively clear that R-tipping occurs if ϵr is small enough so that the external input $T_a(u)$, or equivalently $s(u)$, changes *slowly enough* for the system to jump the 'gap' in $\tilde{M}_1$ between F^- and F^+.

To be precise, we define tracking and R-tipping for $\epsilon = 0$ and fast external inputs as follows,

Definition 6.2.1. In the layer problem (6.5)–(6.6) with two attractors $\tilde{e}^+$ and $\tilde{m}_3^+$,

(i) Tracking occurs when $W^{u,[r]}(\tilde{e}^-)$ connects to $\tilde{e}^+$.

(ii) R-tipping occurs when $W^{u,[r]}(\tilde{e}^-)$ connects to $\tilde{m}_3^+$.

The corresponding dynamics of the layer problem (6.5)–(6.6) on $\tilde{L}$ are shown in a series of phase portraits in figure 6.4, where we fix $T_a^{max} = 15 > T_a^{inst}$ and decrease r across the critical rate. The basin of attraction of $\tilde{e}^+$ is plotted in *green*, and the basin of attraction of $\tilde{m}_3^+$ is plotted in *dark red*. (Blue) $W^s(\tilde{m}_2^+)$ is contained in the basin boundary separating these two basins of attraction. For r sufficiently large, (red) $W^{u,[r]}(\tilde{e}^-)$ lies in the basin of attraction of $\tilde{e}^+$, initially follows $\tilde{M}_1^-$, then jumps the 'gap' between F^- and F^+, and connects to $\tilde{e}^+$; see figure 6.4(a). When $r = r_c$, $W^{u,[r]}(\tilde{e}^-)$ coalesces with $W^s(\tilde{m}_2^+)$ along the basin boundary. At this point, tracking is lost since $W^{u,[r]}(\tilde{e}^-)$ connects to the saddle $\tilde{m}_2^+$; see figure 6.4(b). For $r < r_c$, $W^{u,[r]}(\tilde{e}^-)$ lies in the basin of attraction of $\tilde{m}_3^+$, initially follows $\tilde{M}_1^-$, then fails to jump the 'gap' between F^- and F^+, moves towards $\tilde{M}_3$ and connects to $\tilde{m}_3^+$ along $\tilde{M}_3$. In other words, the system R-tips for $r < r_c$; see figure 6.4(c).

Thus, in the layer problem (6.5)–(6.6), there is an isolated *critical rate* $r = r_c$. This critical rate is the value of r that gives a *codimension-one hetroclinic orbit* connecting $\tilde{e}^-$ to the new saddle $\tilde{m}_2^+$ for the layer problem (6.5)–(6.6). This

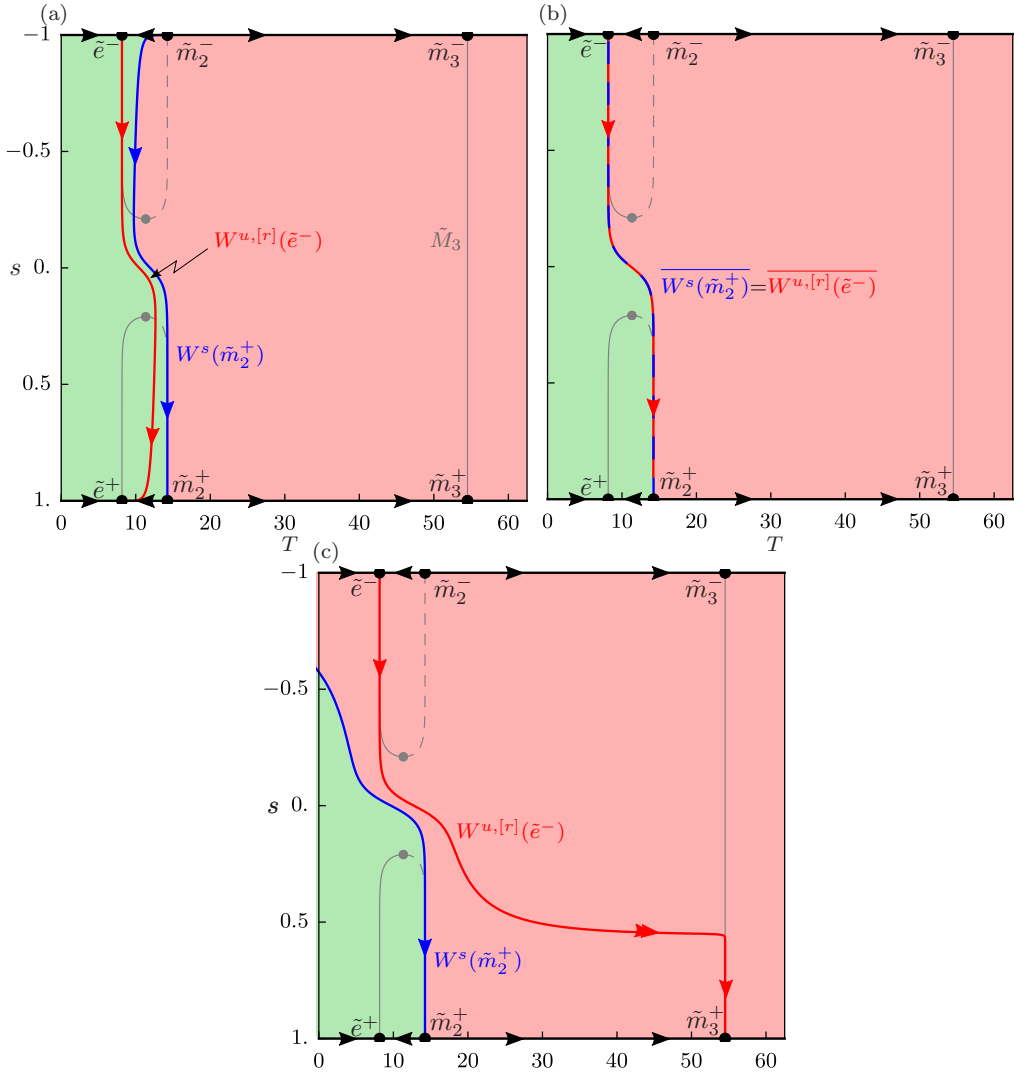


Figure 6.4: Phase portraits of the layer problem (6.5)–(6.6) with impulse (B.2). Shown is the fast case with codimension-one heteroclinic orbit connecting $\tilde{e}^-$ to $\tilde{m}_2^+$ in (b). Included for reference are different branches of (grey) $\tilde{M}$. $T_a^+ = 15$, and the rate parameter takes values (a) $r = 20$, (b) $r = r_c \approx 15.1674$, and (c) $r = 10$; see the black dots in the inset of figure 6.5. System parameter values are given in Table C.1. We use (B.2) instead of (6.2) to more easily see the separation of the branches of $\tilde{M}$.

gives just one case of R-tipping, which we refer to as the *fast R-tipping case* to distinguish it from the three *slow R-tipping cases* identified in section 5.2.1.

6.3 Bringing it Together: Saddle-to-Saddle Heteroclinic Orbit

The aim of this section is twofold. First, we combine our results from section 6.2 with the approach of section 5 to produce the singular R-tipping diagram for $\epsilon = 0$ in figure 6.5. Second, we use the singular R-tipping diagram to explain the regular R-tipping diagram for $\epsilon \approx 0.064$ in figure 6.1.

In the singular R-tipping diagram, the lower-r tracking-tipping transitions were obtained in the same manner as outlined in section 5, that is by computing different heteroclinic orbits in system (5.13)–(5.14). To avoid repetition, we skip the derivations and refer to sections 5.2.1 and 5.3 for more details.

The higher-r tipping-tracking transition, which is the focus of this section, is given by the (blue) curve denoted $\tilde{e}^-$-to-$\tilde{m}_2^+$. This curve was obtained by computing a codimension-one heteroclinic orbit connecting the saddle $\tilde{e}^-$ to the saddle $\tilde{m}_2^+$ in the layer problem (6.5)–(6.6); see figure 6.4(b). This connection gives the only case for (6.5)–(6.6), namely the *fast R-tipping case*, where $\overline{W^{u,[r]}(\tilde{e}^-)} = \overline{W^s(\tilde{m}_2^+)}$.[4] Thus, in the fast R-tipping case, (red) R-tipping is lost via $W^s(\tilde{m}_2^+)$, and this corresponds to the onset of (green) tracking. Note that curves $\tilde{e}^-$-to-$\tilde{m}_2^+$ and $\tilde{e}^-$-to-FS have a common vertical asymptote $T_a^{max} = T_a^{inst} \approx 0.423364$, which is given by condition (4.5) illustrated in figure 4.2.

Next, in addition to the 'first' Fenichel theorem on persistence of normally hyperbolic critical manifolds as slow manifolds for $0 < \epsilon \ll 1$, we recall the 'second' Fenichel theorem that guarantees persistence of stable and unstable invariant manifolds of normally hyperbolic saddle critical manifolds when $0 < \epsilon \ll 1$ [35, 36, 43, 109, 55]. We then use the singular R-tipping diagram in figure 6.5, together with both Fenichel theorems and rigorous results on persistence of singular canards as maximal canards for $0 < \epsilon \ll 1$ [92, 52, 51, 101, 106], to explain

[4] We write $\overline{A}$ to denote the closure of A, that is the smallest closed set containing A.

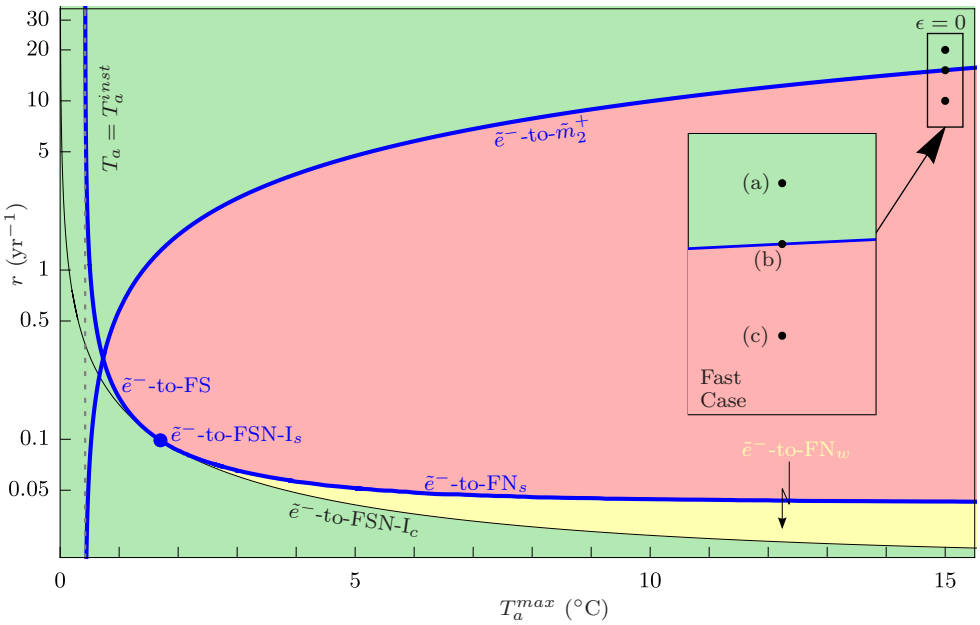


Figure 6.5: Singular R-tipping diagram obtained using a combination of (the lower curves) the reduced problem (5.7)–(5.8) with slow impulse (6.2) and (the upper curve $\tilde{e}^-$-to-$\tilde{m}_2^+$) the layer problem (6.5)–(6.6) with summer heatwave (6.2). At higher r, the (red) region of R-tipping is separated from the (green) region of tracking by (blue) $\tilde{e}^-$-to-$\tilde{m}_2^+$, along which $W^{u,[r]}(\tilde{e}^-)$ intersects $W^s(\tilde{m}_2^+)$ in (6.5)–(6.6). System parameter values are given in Table C.1.

the regular R-tipping diagram in figure 6.1. For the relevant results in the three *slow R-tipping cases* we refer to the discussion in section 5.3, which explains the presence of the small R-tipping tongue and the lower part of the large R-tipping tongue in figure 6.1.

In the *fast R-tipping case*, the heteroclinic $\tilde{e}^-$-to-$\tilde{m}_2^+$ connection for the layer problem (6.5)–(6.6) perturbs to an intersection of $W^{u,[r]}(\tilde{e}^-)$ with the (fast) stable manifold of the normally hyperbolic *saddle slow manifold* $S^+_{2,\epsilon}$ in the compactified system (7.8), giving rise to the (blue) maximal canard shown in figure 6.2. In other words, $W^{u,[r]}(\tilde{e}^-)$ approaches the normally hyperbolic saddle slow manifold $S^+_{2,\epsilon}$ along its stable manifold, thus moves along $S^+_{2,\epsilon}$ for as long $S^+_{2,\epsilon}$ exists, then approaches the stable slow manifold $S^+_{1,\epsilon}$ and eventually connects to $\tilde{e}^+$. In addition, for nearby values of r, we expect associated canards "without head" and canards"with head". These occur when $W^{u,[r]}(\tilde{e}^-)$ near misses the

stable manifold of $S^+_{2,\epsilon}$ to the left or right, respectively, and diverges away from $S^+_{2,\epsilon}$ before $S^+_{2,\epsilon}$ ceases to exist. Thus, it is the (blue) maximal canard shown in figure 6.2, together with the associated canards "without head", that give rise to the higher-r tipping-tracking transition in the regular R-tipping diagram in figure 6.1. In the context of excitable systems, we use Definition 4.1.3(ii) to relate a family of canards "without head" associated with a codimension-one stable manifold of a normally hyperbolic saddle slow manifold to yet another new type of excitability quasithreshold.

6.4 Approximating the Critical Rate

Analysis of the three-timescale problem in section 6.2 reveals the instability arising from from a summer heatwave may be understood as a perturbation of the passage and return though a fold bifurcation of equilibria. This motivates an attempt to approximate the critical rate by using the formula derived in [83].

The formula derived in [83] takes into account the magnitude by which the system overshoots the fold bifurcation, the time the system spends past the fold bifurcation, and the eigenvalues of the equilibria close to the fold bifurcation so that tipping occurs when:

$$a_0^2 \kappa (T_a^+ - T_a^{inst}) t_e^2 \geq 4. \tag{6.8}$$

Following [72], the time that the system spends past the fold bifurcation is given exactly by:

$$t_e = \frac{2}{r} \operatorname{sech}^{-1} \left(\frac{T_a^{inst}}{T_a^+} \right), \tag{6.9}$$

where the value of T_a^{inst} may be approximated with exponentially small error following the procedure outlined in B.1. This also allows calculation of the magnitude of the overshoot $(T_a^+ - T_a^{inst})$. The parameters a_0^2 and κ relate to the eigendirections of the non-hyperbolic fold $F_1(T_a^{inst})$ at the moment of the bifurcation. We note as outlined in section B.1, that the position of $F_1(T_a^{inst})$ may be approximated with exponentially small error by taking $R_s = R_s^\dagger$. Following

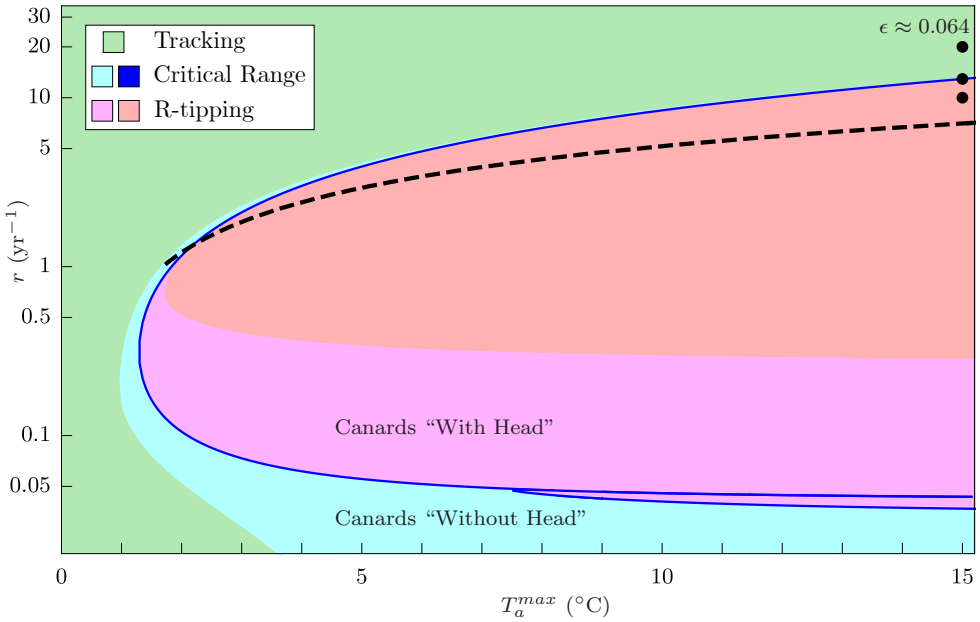


Figure 6.6: The R-tipping diagram of figure 6.1 with (black, dashed) the approximate critical rate for $r \geq 1$ overlaid, which is given when equality holds in (6.10). For more information see the caption of figure 6.1

the formulas derived in [83] these are determined to be:

$$a_0^2 \kappa = \frac{\lambda \alpha^2 A \Pi}{2\mu^2} e^{\alpha(T_a^{inst} - \frac{A\Pi}{\lambda})+1}. \tag{6.10}$$

Figure 6.6 shows (dashed) the curve $a_0^2\kappa(T_a^+ - T_a^{inst})t_e^2 = 4$ for $r \geq 1$ overlaid with the R-tipping diagram of figure 6.1. We note that while the case $r \ll 1$ is considered in [83] which allows the elimination of higher order terms in the derivation, we are primarily concerned with the case $r \lesssim 1/\epsilon$. This in part explains the deviation of the predicted R-tipping transition from the observed R-tipping transition. Additionally, it is assumed in [83] that the path of the system overshoot past the bifurcation is approximately a parabola, while in our case it is in-fact a sector of a hyperbolic sech.

Chapter 7

Numerical Methods for Duck Hunting in C#

In this section we review some of the numerical techniques employed in this work, some of which are particular to compactified systems, and slow-fast dynamical systems. All of the figures in this thesis have been produced in Mathematica, making extensive use of the NDSolve function. Section 7.1 details how $W^{u,[r]}(\tilde{e}^-)$ may be well approximated in this environment. More intensive numerical computations, such as the computation of R-tipping diagrams for $\epsilon = 0$ and $0 < \epsilon \ll 1$, were performed in C# where a fourth order Runge-Kutta (RK4) method with adapative stepsize control as described in section 7.2 was implemented. The methods used to compute R-tipping diagrams are described in section 7.3. The numerical computation of slow manifolds for sections 5.5 were performed using AUTO [32], which was run using Python in a virtual Linux environment and is described in section 7.4.

7.1 The Compactified System

In general R-tipping depends strongly on initial conditions [112, 76, 77], which makes problem formulation a challenge particularly in a nonautonomous setting. A significant advantage of the compactification approach of section 3, is that it allows us to investigate the behaviour of $W^{u,[r]}(\tilde{e}^-)$, with the clear

interpretation that it represents the behaviour of a system initialised near equilibrium for $T_a = T_a^-$ and subsequently exposed to external forcing. Additionally, $W^{u,[r]}(\tilde{e}^-)$ contains $x^{[r]}(t, e^-)$, a local pullback attractor of the corresponding nonautonomous problem in the sense discussed in section 4.1.

When the compactification parameter ν is suitably chosen, $W^{u,[r]}(\tilde{e}^-)$ is guaranteed be normal to the plane $\{s = -1\}$. In this work we choose such a ν where possible and all simulations of the compactified system are performed with the initial condition:

$$(T_0, C_0, s_0) = \tilde{e}^- + (0, 0, \delta), \tag{7.1}$$

i.e. the system is initialised at $\tilde{e}^-$ with a small perturbation in the positive s direction. We take $\delta = 0.0001$, and a solution with the initial condition 7.1 provides a good approximation to $W^{u,[r]}(\tilde{e}^-)$. Additionally, as $W^{u,[r]}(\tilde{e}^-)$ in the compactified system corresponds to a local pullback attractor for the nonautonomous system (4.3), the solution initialised at 7.1 will be initially pushed onto $W^{u,[r]}(\tilde{e}^-)$ provided δ is small enough, further reducing any error in approximation.

7.2 Adaptive Stepsize Control

Choice of stepsize is an important consideration for any system with multiple scales in either time or space. It is important to strike a balance between choosing a stepsize which is small enough to resolve interesting features of the system, and a stepsize which is large enough to enable simulations to be performed in a reasonable timeframe. The compactified system (7.8)–(7.10) evolves on slow timescales for extended periods of time, while many of the interesting dynamics happen on faster timescales and require a small stepsize. In this work, to compute R-tipping diagrams we implement in C# a 4th order Runge-Kutta method with a variable stepsize. At each timestep, we choose the following timestep according to the following pseduocode:

Inputs: t, x, f, h, **rk4_step**(f, x, t, h), Tol

Outputs: y

$y \leftarrow$ **rk4_step**(f, x, t, h)
$y_{small} \leftarrow$ **rk4_step**$(f, x, t, h/2)$
if $||y - y_{small}|| > tol$ **then**
    $t \leftarrow t + h/2$
    $h \leftarrow h/2$
    $y \leftarrow y_{small}$
else
    $y_{big} \leftarrow$ **rk4_step**$(f, x, t, 2h)$
    if $||y_{big} - y|| < tol$ **then**
        $t \leftarrow t + 2h$
        $h \leftarrow 2h$
        $y \leftarrow y_{big}$
    else
        $t \leftarrow t + h$
    end if
end if
return (y),

where t is the current time of the system being integrated, x is the current state variable, f is the vector field of the system, h is the current system stepsize, **rk4_step**(f, x, t, h) is a function which implements the 4th order Rungke-Kutta method to integrate the system forward by a timestep of size h, and Tol is a user-supplied tolerance.

To illustrate the need for a variable stepsize, consider that for a solution initialised at (7.1), the compactified system dynamics (7.8)–(7.10) will initially be super slow, as the system stays close to $\tilde{e}(s)$ and $ds/dt \approx \mathcal{O}(\delta^2)$. This means a large stepsize is required, especially when repeated runs are needed as part of a bisection method as used to produce figures 5.2 and 6.1. However, as s increases the system will evolve on a faster timescale. This is particularly important when s is a fast variable, or when s is a slow variable and the system reaches the fold F_1. As F_1 mediates the switch from slow to fast dynamics, it may be useful to impose a small stepsize as the system approaches the fold, such as when attempting to track secondary or composite canards; see section 7.4

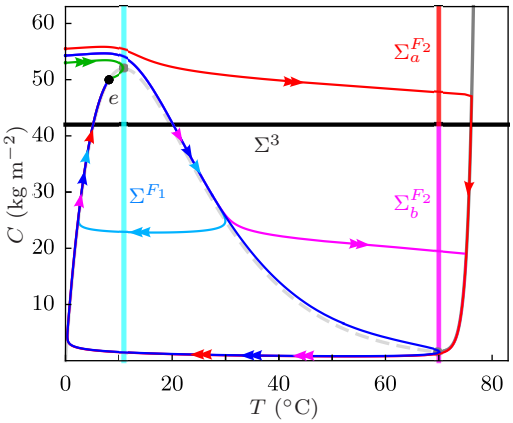


Figure 7.1: The frozen system with the planes (cyan) Σ^{F_1}, (black) Σ^3,(red) $\Sigma_a^{F_2}$ and (magenta)$\Sigma_b^{F_2}$ overlaid. The frozen system may be related to a cross section s =constant of the compactified system (7.8)–(7.10); see figure 7.2.

7.3 R-tipping Diagrams

The R-tipping diagrams of figures 5.2 and 6.1 were created using a bisection method by fixing $T_a^{+/max}$, choosing an interval of r and using the behaviour of $W^{u,[r]}(\tilde{e}^-)$ as the bisection conditions for updating iterations. In this section, we discuss and justify how we numerically determined the behaviour of $W^{u,[r]}(\tilde{e}^-)$ for the bisection conditions.

For the definitions of tracking, R-tipping, and different types of canards we refer to the discussion in section 4.1, and to definitions 4.1.1 and 4.1.2. It follows that to determine whether $W^{u,[r]}(\tilde{e}^-)$ tracks or R-tips, and similarly to determine if it contains a canard, we must determine if $W^{u,[r]}(\tilde{e}^-)$ visits $S_{2,\epsilon}$ and / or $S_{3,\epsilon}$. This may be achieved using suitably chosen planes in the (T, C, s) phase space.

The outflow boundary of $S_{3,\epsilon}$ (and of $S_{2,\epsilon}$) is well approximated by F_2. It follows that a trajectory will visit $S_{3,\epsilon}$ if it crosses the plane:

$$\Sigma^{F_2} := \left\{(T, C, s) \,:\, T = T^{F_2}(s)\right\}, \tag{7.2}$$

In the positive T direction. The only way to cross Σ^{F_2} in the negative T direction is to do so either along or below $S_{3,\epsilon}$. Similarly, the inflow boundary of $S_{2,\epsilon}$ is

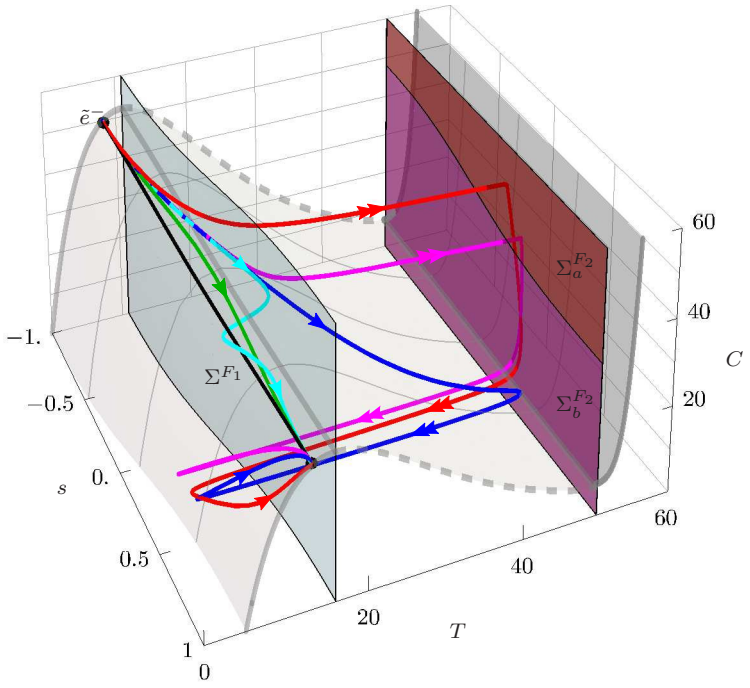


Figure 7.2: The compactified system (7.8)–(7.10) with the planes (cyan) Σ^{F_1},(red) $\Sigma_a^{F_2}$ and (magenta)$\Sigma_b^{F_2}$ overlaid. Also shown is $W^{u,[r]}(\tilde{e}^-)$ for different values of r to show how different types of canard solutions may be detected.

well approximated by F_1, and we define the plane:

$$\Sigma^{F_1} := \left\{(T, C, s) \,:\, T = T^{F_1}(s)\right\}, \tag{7.3}$$

where when s is a slow variable, if $W^{u,[r]}(\tilde{e}^-)$ crosses Σ^{F_1} in the positive T direction then it must leave $S_{1,\epsilon}$. This implies that it must visit at least one, and possibly both, of $S_{2,\epsilon}$ and $S_{3,\epsilon}$. When s is a fast variable, $W^{u,[r]}(\tilde{e}^-)$ always leaves $S_{1,\epsilon}$.

A solution which leaves $S_{1,\epsilon}$ will only undergo a substantial decrease in C by travelling along the other slow manifolds $S_{2,\epsilon}$ and $S_{3,\epsilon}$. This means a solution which leaves $S_{1,\epsilon}$ and reaches Σ^{F_2} only after undergoing a substantial decrease in carbon must have travelled along $S_{2,\epsilon}$ for some time $\mathcal{O}(1)$ as per definition 4.1.1. This motivates a partition of the plane Σ^{F_2} as follows:

$$\Sigma^{F_2}_a := \left\{(T, C, s) \in \Sigma^{F_2} \,:\, C \geq C^e(s) - k\right\}, \tag{7.4}$$

$$\Sigma^{F_2}_b := \left\{(T, C, s) \in \Sigma^{F_2} \,:\, C < C^e(s) - k\right\}, \tag{7.5}$$

where $k \in \mathbb{R}$ is a suitably chosen constant. We choose $C^e(s) - k$ to account for the fact that $C^{F_1}(s)$ varies with s, meaning that at the moment a solution leaves $S_{1,\epsilon}$ through F_1, its value of C will depend on s.

When s is slow, a solution which crosses Σ^{F_1} in the positive T direction but does not cross Σ^{F_2} must visit $S_{2,\epsilon}$. This is not the case when s is fast, as solutions may leave $S^-_{1,\epsilon}$, cross Σ^{F_1} in the positive T direction, before crossing again in the negative T direction and go to $S^+_{1,\epsilon}$, all without visiting $S^+_{2,\epsilon}$. However, such a solution will not undergo a substantial decrease in carbon. This is in contrast to a solution which travels along $S_{2,\epsilon}$ for some time $\mathcal{O}(1)$. This motivates the definition of a third plane:

$$\Sigma^3 := \left\{(T, C, s) \,:\, C = C^e(\pm 1) - k\right\}, \tag{7.6}$$

where $k \in \mathbb{R}$ is a suitably chosen constant. When s is fast, if a solution crosses Σ^3 but not Σ^{F_2}, it must have visited $S_{2,\epsilon}$. This does not hold when s is slow, as a solution may cross Σ^3 without leaving $S_{1,\epsilon}$.

We are now ready to describe how to numerically determine what is the behaviour of the system and of $W^{u,[r]}(\tilde{e}^-)$ for a given $(T_a^{+/max}, r)$:

- *R-tipping*: if $W^{u,[r]}(\tilde{e}^-)$ crosses $\Sigma_a^{F_2}$ in the positive T direction, the system is determined to R-tip and $W^{u,[r]}(\tilde{e}^-)$ is determined to be a regular trajectory.

- *Canard "with head"*: if $W^{u,[r]}(\tilde{e}^-)$ crosses $\Sigma_b^{F_2}$ in the positive T direction, the system is determined to R-tip and $W^{u,[r]}(\tilde{e}^-)$ is determined to be a canard "with head".

- *Maximal Canard*: if $W^{u,[r]}(\tilde{e}^-)$ is tangent to Σ^{F_2}, then it is determined to be a maximal canard.

- *Canard "without head"*: When s is slow, if $W^{u,[r]}(\tilde{e}^-)$ crosses Σ^{F_1} and does not cross Σ^{F_2} then it is determined to be a canard "without head". When s is fast, if $W^{u,[r]}(\tilde{e}^-)$ crosses Σ^3 and does not cross Σ^{F_2} then it is determined to be a canard "without head".

- *Tracking*: When s is slow, if $W^{u,[r]}(\tilde{e}^-)$ does not cross Σ^{F_1} then the system is determined to track. When s is fast, if $W^{u,[r]}(\tilde{e}^-)$ does not cross Σ^3 then the system is determined to track. Alternatively, if we do not have cases (i)–(iv), then the only other possibility is that the system tracks.

7.4 Hunting Secondary and Composite Canards

The boundaries of the R-tipping tongues in figures 5.2 and figures 6.1 are formed by secondary and composite canards. We recall from section 5.4 that the common feature shared by these canards is that they leave $S_{1,\epsilon}$, then follow $S_{2,\epsilon}$ for a time before heading back to $S_{1,\epsilon}$. A secondary canard does so by travelling along an intersection of $S_{1,\epsilon}$ and $S_{2,\epsilon}$, while a composite canard makes a fast switch in the manner of a canard "without head". These trajectories then leave $S_{1,\epsilon}$ for a second time and follow $S_{2,\epsilon}$ for as long as it exists in the manner of a maximal canard. For further detail we refer to the discussion in section 5.4.

Numerically, speaking then secondary and composite canards are identified as maximal canards per section 7.3. However they may be distinguished if necessary using the planes already defined:

- *Composite and Secondary Canards*: If $W^{u,[r]}(\tilde{e}^-)$ crosses Σ^{F_1} *three* times, first in the positive T direction, followed by the negative T direction and the positive T direction again, and is subsuquently tangent to Σ^{F_2} then it is determined to be either a composite or secondary canard.

Note that it is particularly important to use a small stepsize close to the fold F_1 in this instance, as maximal canards are numerically unstable objects and the secondary canard 'twist' about F_1 may be small. To distinguish whether $W^{u,[r]}(\tilde{e}^-)$ is a secondary canard or a composite canard requires a visual inspection of $W^{u,[r]}(\tilde{e}^-)$ together with $\tilde{\gamma}_\epsilon^S$ and $\tilde{\gamma}_{s,\epsilon}^N$ in the manner shown in figures 5.8. However, as we are primarily interested in the numerical continuation of curves where $W^{u,[r]}(\tilde{e}^-)$ is either a secondary or composite canard in $(T_a^{+/max}, r)$ parameter space, a single inspection will suffice to determine which type of curve is being tracked.

While the boundaries of R-tipping tongues are formed by composite and secondary canards, for resolving R-tipping tongues with a bisection method it is useful to know when a chosen pair of $(T_a^{+/max}, r)$ is taken from *inside* and R-tipping tongue. Inside an R-tipping tongue, $W^{u,[r]}(\tilde{e}^-)$ is a *secondary canard "with head"*, in that it twists about F_1 once before R-tipping. Such behaviour may be determined as follows:

- *Secondary Canards "with head"*: If $W^{u,[r]}(\tilde{e}^-)$ crosses Σ^{F_1} *three* times, in the same manner as a secondary or composite canard (see (vi)), and following this crosses $\Sigma_b^{F_2}$, then it is determined to be a secondary canard "with head".

7.5 Computing Slow Manifolds

Following the numerical continuation methods outlined in [28, 30], the slow manifolds $S_{1,\epsilon}$ and $S_{2,\epsilon}$ as well as canard trajectories may be computed as solutions to an appropriately formulated boundary value problem in AUTO [32].

Broadly speaking, the idea is to calculate both slow manifolds in the plane Σ^{FN}, then manually identify their intersections in Σ^{FN} by visual inspection. Such intersections correspond to maximal canards. The intersecting slow manifolds $S_{1,\epsilon}$ and $S_{2,\epsilon}$ as shown in figure 5.11 may be extended outwards from the plane $s = -0.369038$ in the negative and positive s directions by following solutions initialised on $S_{1,\epsilon}$ and $S_{2,\epsilon}$ in the plane Σ^{FN} backwards and forwards in time respectively, and piecing together the resulting trajectories. Figure 7.3 shows (blue) $S_{1,\epsilon}$ and (red) $S_{2,\epsilon}$ extended backwards and forwards in time respectively from the plane $s = -0.369038$. This allows us to see how the maximal canards, shown in black, cross from $S_{1,\epsilon}$ to $S_{2,\epsilon}$.

The method for computing slow manifolds and their intersections is as follows. The folded singularity FN which exists for $\epsilon = 0$, perturbs to a transverse intersection of $S_{1,\epsilon}$ and $S_{2,\epsilon}$ for $0 < \epsilon \ll 1$. We choose a plane of constant s which contains FN to approximate the location of the transverse intersection:

$$\Sigma^{FN} := \{(T, C, s) \ : \ s = s^{FN}\}, \tag{7.7}$$

where s^{FN} is the value of s such that Σ^{FN} contains FN when $\epsilon = 0$. The initial goal is to calculate $S_{1,\epsilon} \bigcap \Sigma^{FN}$ and $S_{2,\epsilon} \bigcap \Sigma^{FN}$ using a pair of boundary value problems. When the two sets intersect, such intersections correspond to maximal canards. Additionally, the solutions to these boundary value problems are two families of orbit segments which represent the slow manifolds $S_{1,\epsilon}$ and $S_{2,\epsilon}$ respectively.

We aim to represent the slow manifolds $S_{1,\epsilon}$ and $S_{2,\epsilon}$ as a family of orbit segments calculated using numerical continuation in AUTO. We consider the following system:

$$\epsilon \frac{dT}{dt} = T_{int}\, f_1(T, C, T_a^{\nu}(s)), \tag{7.8}$$

$$\frac{dC}{dt} = T_{int}\, f_2(T, C), \tag{7.9}$$

$$\frac{1}{r}\frac{ds}{dt} = T_{int}\, \frac{\nu}{2}(1 - s^2), \tag{7.10}$$

where T_{int} is the total integration time and is a free parameter. So that any

orbit segment $u(t)$ is represented over the interval $t \in [0,1]$. the strategy is as follows. Taking $X(t) = (T(t), C(t), s(t))$, we define the following boundary value problems:

$$\begin{cases} X(0) \in L_a, \\ X(1) \in \Sigma^{FN}, \end{cases} \quad \text{and} \quad \begin{cases} X(0) \in \Sigma^{FN}, \\ X(1) \in L_r, \end{cases} \tag{7.11}$$

where $L_{a,r}$ are one-dimensional submanifolds and Σ^{FN} is as defined in (7.7) - a codimension-one submanifold of $\mathbb{R}^3$. We choose L_a to be on the attracting sheet of the critical manifold S_1 sufficiently far from the fold F_1 so that S_1 is a good approximation of $S_{1,\epsilon}$, while we choose L_r on S_2 similarly far from F_1. In this way, an orbit segment which begins in L_a and ends Σ^{FN} approximates an orbit segment along $S_{1\epsilon}$. Similarly, an orbit segment beginning in Σ^{FN} and ending on L_r approximates an orbit segment along $S_{1\epsilon}$. By varying $X(0)$ along L_a in the first BVP and $X(1)$ along L_r in the second BVP we obtain two collections of such orbit segments which provide approximations of $S_{1,\epsilon}$ and $S_{2,\epsilon}$ respectively.

These boundary value problems are solved via numerical continuation by first restricting $L_{a,r}$ to be on the fold F_1 amd growing T_{int} from 0, then moving $L_{a,r}$ away from F_1 until it sits sufficiently far away. This homotopy-type method gives initial solutions to the boundary value problems of interest (7.11), from which other solutions may be found. This procedure is described in detail in [29], and is implemented as an example in the current distribution of AUTO for the Fitzhugh-Nagumo oscillator.

This computation has already been performed close to a folded node in [29, 28, 30]. However aside from the work of [77], to the best of our knowledge a similar computation has not been performed close to a composite canard to date. Additionally, figure 7.3 is the first time slow manifolds have been extended into three dimensions close to a composite canard. The reason they have not been studied intensely to date may be due to their peculiar nature, occurring close to both the folded-node primary maximal canard $\tilde{\gamma}^N_{s,\epsilon}$ and a secondary canard $\tilde{\xi}^1_\epsilon$. Additionally, while analytic results have been obtained which prove the existence of secondary canards [109], to the best of our knowledge no such results exist for composite canards which have only been observed numerically [76, 77]. Finally,

composite canards should be more apparent where the small parameter ϵ is relatively large for a singular perturbation problem as in the current study.

This work may be extended in a number of ways. In particular there is more work to be done in understanding how the kind of folding shown in figure 7.3, which gives rise to composite canards, arises as the ratio of the strong and weak eigenvalues μ increases. Also of interest is how $W^s(\tilde{\gamma}^S)$, the stable manifold of the folded saddle singular canard and $W^u(\tilde{\gamma}_s^N)$, the unstable manifold of the folded-node strong singular canard, each of which exists for $\epsilon = 0$, persist for $0 < \epsilon \ll 1$ as stable and unstable fast manifolds of the corresponding maximal canards and interact. A similar study of fast manifolds of faux canards was performed in [67], where they were shown to be responsible for rotational behaviour of solutions close to a folded saddle. Finally, we have presented in section 5.3 a unified picture of the unfolding of a *codimension two non-central heteroclinic FSN-I* in the plane (T_a^+, r) for $\epsilon = 0$. It should be possible to study the unfolding for $0 < \epsilon \ll 1$ of the corresponding slow manifolds with the methods used here, together with numerical continuation in ϵ following [30]. This would provide a unified picture of the three parameter unfolding of an FSN-I bifurcation.

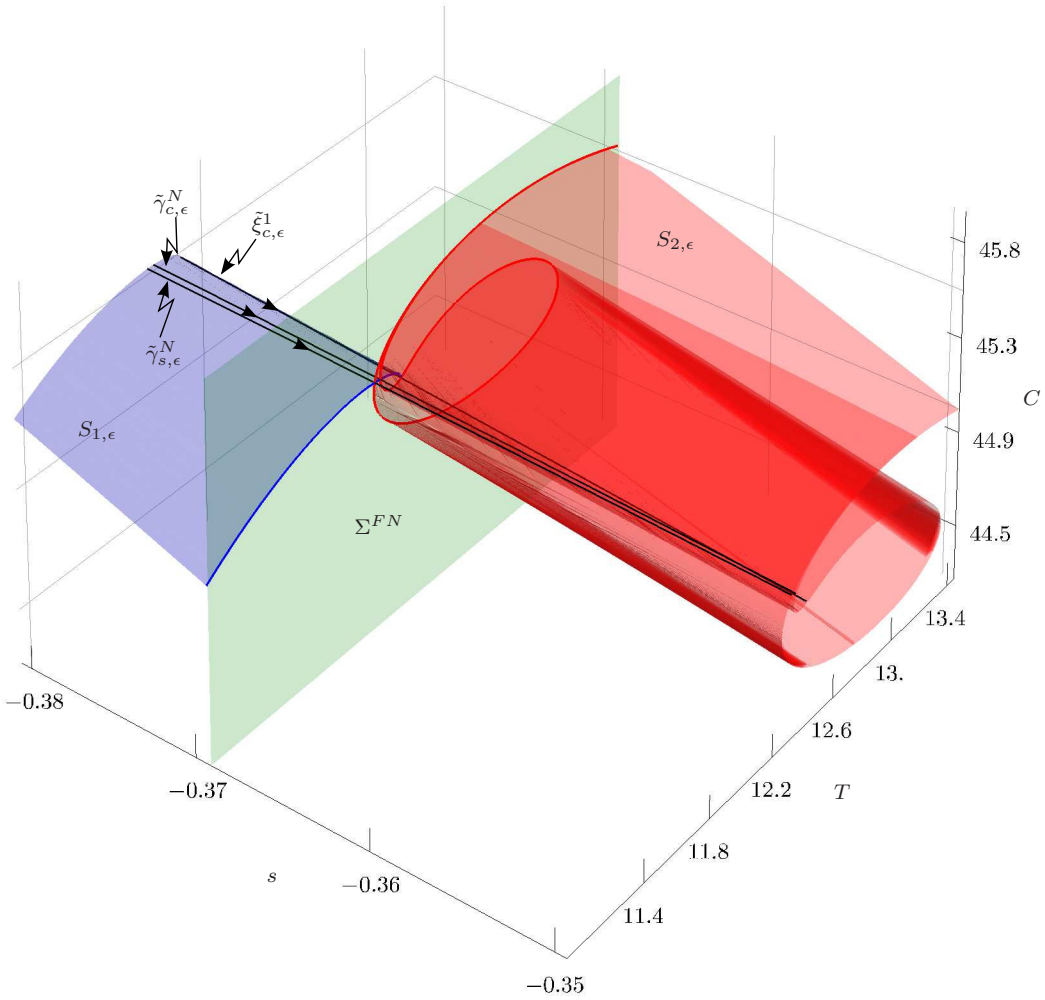


Figure 7.3: The (blue) attracting and (red) repelling slow manifolds $S_{1\epsilon}$ and $S_{2,\epsilon}$ extended outwards from the (green) plane $s \approx -0.369038$. Shown also are (black) the folded-node maximal canard $\tilde{\gamma}^N_{s,\epsilon}$, folded-node composite canard $\tilde{\gamma}^N_{c,\epsilon}$ and the secondary canard $\tilde{\xi}^1_\epsilon$ which travel along intersections of $S_{1\epsilon}$ and $S_{2,\epsilon}$. Note that the secondary canard is contained within $W^{u,[r]}(\tilde{e}^-)$

Chapter 8

Conclusion and Outlook

This thesis showcases three kinds of results. First, we demonstrate that sufficiently fast atmospheric warming can cause R-tipping to a subsurface hot metastable state in bioactive peat soils, using a conceptual process-based ODE model with realistic soil parameter values and contemporary climate patterns. This gives rise to the hypothesis that such R-tipping is a main cause of "Zombie fires" observed in peatlands, that disappear from the surface, smoulder underground during the winter, and "come back to life" in the spring. Second, we recognise that such R-tipping is a nonautonomous instability that occurs due to crossing an elusive quasithreshold in the phase space of a multiple timescale dynamical system, and thus cannot be explained by traditional autonomous stability theory. Therefore, to understand the underlying dynamical mechanisms, we provide a mathematical framework that is underpinned by a compactification technique for asymptotically autonomous dynamical systems and concepts from geometric singular perturbation theory, such as slow manifolds, canard trajectories and folded singularities, and use the conceptual soil-carbon model as an illustrative example. This explains R-tipping to the hot metastable state and, more generally, identifies generic cases of R-tipping due to crossing a quasithreshold. Furthermore, it shows that a quasithreshold gives rise to critical ranges of the rate of change of the external input rather than isolated critical rates, and reveals new types of quasithresholds. Third, we compute of slow manifolds in the compactified system together with their maximal canards in order

to understand the complicated shape of R-tipping quasithresholds in three dimensions. The twisting of the repelling slow manifold in particular may give rise to secondary canards, composite canards, and composite secondary canards. As such canards form part of a corresponding R-tippign quasithreshold, this shows its complicated shape and gives insight into how for a given $T_a^{+/max}$ large enough there may be multiple critical ranges of the rate parameter r. These results pose three types of challenges for future research.

First, to strengthen our hypothesis, it would be interesting to build on the excellent agreement with the medium-complexity PDE model in figure 2.4 and extend the conceptual ODE model in different directions. For example, include terms describing peat soil ignition processes at higher temperatures [120]. This would allow investigation of existence of additional (quasi)thresholds for the onset of flames. Include other physical processes, in addition to soil temperature, that contribute to microbial soil respiration. For example, microbial soil respiration is also strongly moisture dependent [90, 60, 46], and the inclusion of soil hydrology would extend the applicability of the model; see for example DigiBog_Hydro [8] and [103]. Include random fluctuations to account for the fact that climate and weather patterns are inherently noisy. This would give a more accurate description of the tipping being a combination of R-tipping and noise-induced tipping (N-tipping). Understanding how the two tipping mechanisms interact is non-trivial [82] and an area of ongoing research for quasithresholds [91]. Account for spatio-temporal dynamics by extending the conceptual ODE model to a PDE model. Vertical diffusion has already been studied in the extended Luke and Cox model with interesting results confirming validity of the conceptual ODE model [26]. Further to this, the inclusion of lateral diffusion on a heterogeneous spatial domain would allow investigation of lateral heat and fire patterns, and how they evolve over time, in the ensuing reaction-diffusion equation. This, in turn, would enable comparisons with satellite data of peatland fires. Finally, it might be interesting to couple the conceptual model to spatially extended land-surface models such as JULES [7] or DigiBog [6]. Currently, such models often neglect heat produced by microbial decomposition which is a key factor for the R-tipping instability to the hot metastable state described in this

thesis.

Second, there are challenges related to extending the mathematical framework and obtaining rigorous results. The definitions of R-tipping and a quasithreshold introduced here for the soil-carbon model are a good starting point towards a general theory of R-tipping due to crossing quasithresholds in multiple timescale systems. Of particular interest to scientists and mathematical modelers are rigorous yet easily testable criteria for the occurrence of such R-tipping, akin to those derived in [113] for R-tipping due to crossing regular thresholds.

Third, there are challenges relating to the computation of slow manifolds and quasithresholds. Aside from the current work, to the best of our knowledge computation of slow manifolds close to a composite canard has only been performed in [77], meaning there is still much work to be done. Moreover, although we extend the slow manifolds into three dimensions in figure 7.3, this computation is only performed local to the folded node FN, meaning there is more work to be done on obtaining a global picture of the slow manifolds. This computation could be performed with the methods used here, and would also give a global picture of an R-tipping quasithreshold in three dimensions. Additionally, there are outstanding questions regarding how composite canards which exist for $0 < \epsilon \ll 1$, relate to stable and unstable manifolds of singular canards which exist for $\epsilon = 0$; see the discussion at the end of section 7.5. Finally, a study of the three parameter unfolding of an FSN-I bifurcation as discussed in section 7.5 would consolidate much of the work that has been performed to date on folded singularities and canards, as well as giving insight into the persistence of FSN-I dynamics for $0 < \epsilon \ll 1$, where there is still much to be understood [67].

Appendix A

Details for Figures

A.1 Details for Figure 1

The Berkeley Earth dataset [5] gives a field of the land temperature anomalies $\Phi(\mathbf{x}, m)$ for a given month m compared to the average temperature for that month for the period 1951-1980. We take the mean temperature anomaly field $\bar{\Phi}(\mathbf{x})$ for the 60 months from January 2017 to December 2021 inclusive. A field of the rates of warming, as shown in figure 1.1, is then obtained as follows:

$$r(\mathbf{x}) = \frac{\bar{\Phi}(\mathbf{x})}{\frac{1}{2}(2021 + 2017) - \frac{1}{2}(1980 + 1951)}. \tag{A.1}$$

A.2 External Input and Parameter Details for Figure 2

In figure 2.2, the external input is given by

$$T_a(rt) = \frac{T_a^{Jul} - T_a^{Jan}}{2} \left(\sin\left(2\pi t\right) + 1\right) + T_a^{Jan} + T_a^{+} \operatorname{sech}\left(r(t - 10.25)\right). \tag{A.2}$$

where $r = 10$, $T_a^{+} = 20$, and $T_a^{Jan} = -33.1°\text{C}$, $T_a^{July} = 12.9°\text{C}$ are the mean January, July temperatures recorded at Cherskii in Northern Siberia [2].

A.3 External Input and Parameter Details for Figure 3

In figure 2.3, the external input is given by

$$T_a(rt) = \frac{T_a^+ - T_a^-}{2} \left(\tanh\left(r(t-140)\right) + 1\right) + T_a^-, \tag{A.3}$$

where $r = 0.025$, $T_a^+ = -6$, and $T_a^- = -10.1$ is the mean value of seasonal component of (A.2), which is based on temperatures recorded at Cherskii in Northern Siberia [2].

A.4 External Input and Parameter Details for Figure 4

In figure 2.4, atmospheric temperature external input is given by

$$T_a(rt) = \frac{T_a^+ - T_a^-}{2} \left(\tanh\left(r(t-2050)\right) + 1\right) + T_a^-. \tag{A.4}$$

Parameter values used are $T_a^- = -5°\text{C}$, $T_a^+ = 2°\text{C}$, $\Pi = 0.09$, $r = 0.025$ and $T^* = 35$, which correspond to values used by [46].

Appendix B

Additional Derivations

B.1 Threshold Instability Condition

For $T < T^*$, the modified non-monotone respiration function $R_s^*(T)$ in (2.11) is well approximated by the monotone $R_s^\dagger(T)$ (2.10), which may be used to a derive a closed-form approximation for F_1. We recall the fold condition for a fixed value of T_a with $R_s(T) = R_s^\dagger(T)$:

$$\partial f_1/\partial T|_S = -\frac{\lambda}{A}\left(1 + (T - T_a\frac{r_s'(T)}{R_s^\dagger(T)}\right) = 0.$$

This gives an approximation of the T-component of the fold F_1, which we denote T^{F_1}. We use $\approxeq$ to indicate that the expression is exact when $R_s(T) = R_s^\dagger(T)$, and near exact (has an exponentially small error) when $R_s(T) = R_s^*(T)$. Applying the critical manifold condition gives

$$\left(T^{F_1}(T_a), C^{F_1}(T_a)\right) \approxeq \left(\frac{1}{\alpha} + T_a, \frac{\lambda}{\alpha A R_s^\dagger(T^{F_1}(T_a))}\right).$$

We note from section 4.1 that there is a special value T_a^{inst} for which $e(0) \in \theta(T_a^{inst})$. This condition is equivalent to $C^e(0) = C^{F_1}(T_a^{inst})$, which gives

$$\frac{\Pi}{R_s^\dagger(\frac{A\Pi}{\lambda})} = \frac{\lambda}{\alpha A R_s^\dagger(T^{F_1}(T_a^{inst}))}.$$

Solving for T_a^{inst} gives the following expression

$$T_a^{inst} \approxeq -\frac{1}{\alpha}\left(1 + \log\left(\alpha\frac{A\Pi}{\lambda}\right) - \alpha\frac{A\Pi}{\lambda}\right). \tag{B.1}$$

B.2 Compactified Summer Heatwave

In figure 6.4, to more easily see the separation of the branches of $\tilde{M}$ rather than $T_a^{0.5}(s)$ (6.2) we use $T_a^{\nu}(s) = T_a^{0.1}(s)$ which is given by:

$$T_a^{\nu}(s) = T_a^{\frac{1}{10}}(s) = \frac{2\,T_a^{max}\,(1-s)^{10}}{(1+s)^{20} + (1-s)^{20}}. \tag{B.2}$$

Appendix C

Table of Parameters

Parameters		
Symbol	Description	Value
μ	Areal Soil Heat Capacity	$2.5 \times 10^6\,\mathrm{J\,m^{-2}\,{}^\circ C^{-1}}$
λ	Soil-to-Atmosphere Heat Transfer Coefficient	$5.049 \times 10^6\,\mathrm{J\,y^{-1}\,m^{-2}\,{}^\circ C^{-1}}$
r	Rate Parameter	$r \in (0, \infty)\ \mathrm{y^{-1}}$
A	Specific Heat of Microbial Respiration	$3.9 \times 10^7\,\mathrm{J\,kg^{-1}}$
Π	Gross Primary Production	$1.055\,\mathrm{kg\,m^{-2}\,y^{-1}}$
α	Respiratory Growth Rate	$\ln(2.5)/10$
$R_s(0)$	Reference respiration at 0°C	0.01
c	Decay : Growth Ratio	10
T^*	Respiration Die-Off Temperature	$30, 50$ or 70°C

Table C.1

Bibliography

[1] 2021 2021 38°C record Arctic temperature confirmed, others likely to follow: WMO. *UN News*, 14 December. See https://news.un.org/en/story/2021/12/1107872. 3

[2] 2021 Chersky climate: Average Temperature, weather by month. *Climate-Data.org*. See https://en.climate-data.org/asia/russian-federation/sakha-republic/chersky-333972/#climate-table. Accessed: 2021-04-21. 26, 31, 32, 33, 119, 120

[3] 2021 What are 'zombie fires' and why is the Arctic Circle on fire?. *BBC Newsround*, 20 May. See https://www.bbc.co.uk/newsround/57173570. 22, 30, 31, 32

[4] 2022 2022 A milestone in UK climate history. *Met Office: Weather and Climate*, 22 July. See https://www.metoffice.gov.uk/about-us/press-office/news/weather-and-climate/2022/july-heat-review. 3

[5] 2022 Berkeley Earth: Data Overview. See http://berkeleyearth.org/data/. 3, 4, 119

[6] 2022 Digibog: water@leeds. See https://water.leeds.ac.uk/our-missions/mission-1/digibog/. Accessed: 2022-09-12. 117

[7] 2022 Joint UK Land Environment Simulator (JULES). See https://jules.jchmr.org/. Accessed: 2022-09-12. 117

[8] 2022 Resources: water@leeds. See https://water.leeds.ac.uk/

our-missions/mission-1/digibog/resources/. Accessed: 2022-09-12. 117

[9] Alkhayuon HM, Ashwin P. 2018 Rate-induced tipping from periodic attractors: Partial tipping and connecting orbits. *Chaos* **28**, 033608. 5

[10] Alkhayuon H, Tyson RC, Wieczorek S. 2021 Phase tipping: how cyclic ecosystems respond to contemporary climate. *Proc. R. Soc. A* **477**, 20210059. 5

[11] Arnscheidt CW, Rothman DH. 2022 Rate-induced collapse in evolutionary systems. *Journal of The Royal Society Interface* **19**. 22

[12] Ashwin P, Wieczorek S, Vitolo R, Cox P. 2012 Tipping points in open systems: bifurcation, noise-induced and rate-dependent examples in the climate system. *Phil. Trans. R. Soc. A* **370**, 1166–1184. 5, 6, 30

[13] Ashwin P, Perryman C, Wieczorek S. 2017 Parameter shifts for nonautonomous systems in low dimension: bifurcation- and rate-induced tipping. *Nonlinearity* **30**, 2185–2210. 5, 6, 30, 50, 58, 75

[14] Benoît É. 1983 Systemes lents-rapides dans R^3 et leurs canards. *Asterisque* pp. 109–110. 48, 68, 70

[15] Benoît É, Callot J, Diener F, Diener M. 1981 Chasse au canard (première partie). *Collectanea Mathematica* **32**, 37–76. 49, 68

[16] Beringer J, Lynch AH, Chapin FS, Mack M, Bonan GB. 2001 The Representation of Arctic Soils in the Land Surface Model: The Importance of Mosses. *Journal of Climate* **14**, 3324 – 3335. 26, 27

[17] Berner LT, Massey R, Jantz P, Forbes BC, Macias-Fauria M, Myers-Smith I, Kumpula T, Gauthier G, Andreu-Hayles L, Gaglioti BV, Burns P, Zetterberg P, D'Arrigo R, Goetz SJ. 2020 Summer warming explains widespread but not uniform greening in the Arctic tundra biome. *Nature Communications* **11**. 60

[18] Boers N, Rypdal M. 2021 Critical slowing down suggests that the western Greenland Ice Sheet is close to a tipping point. *Proc. Natl Acad. Sci.* **118**, e2024192118. 4

[19] Boulton CA, Lenton TM, Boers N. 2022 Pronounced loss of Amazon Rainforest Resilience since the early 2000s. *Nat. Clim. Change* **12**, 271–278. 5

[20] Box JE, Hubbard A, Bahr DB, Colgan WT, Fettweis X, Mankoff KD, Wehrlé A, Noël B, van den Broeke MR, Wouters B, Bjørk AA, Fausto RS. 2022 Greenland ice sheet climate disequilibrium and committed sea-level rise. *Nature Climate Change* **12**, 808–813. 5

[21] Buggeln R, Rynk R. 2002 Self-Heating In Yard Trimmings: Conditions Leading To Spontaneous Combustion. *Compost Science & Utilization* **10**, 162–182. 3, 30

[22] Buldovicz SN, Khilimonyuk VZ, Bychkov AY, Ospennikov EN, Vorobyev SA, Gunar AY, Gorshkov EI, Chuvilin EM, Cherbunina MY, Kotov PI, Lubnina NV, Motenko RG, Amanzhurov RM. 2018 Cryovolcanism on the Earth: Origin of a Spectacular Crater in the Yamal Peninsula (Russia). *Scientific Reports* **8**. 46

[23] Caesar L, Rahmstorf S, Robinson A, Feulner G, Saba V. 2018 Observed fingerprint of a weakening Atlantic Ocean Overturning Circulation. *Nature* **556**, 191–196. 4

[24] Chen Y, Gemmer JA, Silber M, Volkening A. 2019 Noise-induced tipping under periodic forcing: Preferred tipping phase in a non-adiabatic forcing regime. *Chaos: An Interdisciplinary Journal of Nonlinear Science* **29**, 043119. 6

[25] Chow S, Lin X. 1990 Bifurcation of a homoclinic orbit with a saddle-node equilibrium. *Differential and Integral Equations* **3**, 435–466. 77

[26] Clarke J, Huntingford C, Ritchie P, Cox P. 2021 The compost bomb instability in the continuum limit. *Eur. Phys. J. Spec. Top.* **230**, 3335–3341. 3, 30, 117

[27] Cox PM, Betts RA, Collins M, Harris PP, Huntingford C, Jones CD. 2004 Amazonian forest dieback under climate-carbon cycle projections for the 21st Century. *Theoretical and Applied Climatology* **78**. 5

[28] Desroches M, Krauskopf B, Osinga HM. 2008a The geometry of slow manifolds near a folded node. *SIAM J. Appl. Dyn. Syst.* **7**, 1131–1162. 23, 81, 84, 111, 113

[29] Desroches M, Krauskopf B, Osinga HM. 2008b Mixed-mode oscillations and slow manifolds in the self-coupled FitzHugh-Nagumo system. *Chaos: An Interdisciplinary Journal of Nonlinear Science* **18**, 015107. 113

[30] Desroches M, Krauskopf B, Osinga HM. 2010 Numerical continuation of canard orbits in slow–fast dynamical systems. *Nonlinearity* **23**, 739–765. 23, 80, 81, 83, 84, 111, 113, 114

[31] Ditlevsen PD, Johnsen SJ. 2010 Tipping points: Early warning and wishful thinking. *Geophysical Research Letters* **37**, n/a–n/a. 6

[32] Doedel EJ, Fairgrieve TF, Sandstede B, Champneys AR, Kuznetsov YA, Wang X. 2007 *AUTO-07P: Continuation and bifurcation software for ordinary differential equations.* 104, 111

[33] Dumortier F, Roussarie R. 1996 *Canard Cycles and Center Manifolds.* Number no. 577 in American Mathematical Society: Memoirs of the American Mathematical Society. American Mathematical Soc. 68

[34] Dumortier F. 1993 Techniques in the Theory of Local Bifurcations: Blow-Up, Normal Forms, Nilpotent Bifurcations, Singular Perturbations. In Schlomiuk D, editor, *Bifurcations and Periodic Orbits of Vector Fields* pp. 19–73. Dordrecht: Springer Netherlands. 48

[35] Fenichel N, Moser JK. 1971 Persistence and Smoothness of Invariant Manifolds for Flows. *Indiana University Mathematics Journal* **21**, 193–226. 48, 100

[36] Fenichel N. 1979 Geometric Singular Perturbation Theory for Ordinary Differential Equations. *Journal of Differential Equations* **31**, 53–98. 22, 46, 48, 100

[37] FitzHugh R. 1955 Mathematical models of threshold phenomena in the nerve membrane. *The bulletin of mathematical biophysics* **17**, 257–278. 10, 17

[38] Guckenheimer J, Meerkamp P. 2012 Unfoldings of Singular Hopf Bifurcation. *SIAM Journal on Applied Dynamical Systems* **11**, 1325–1359. 59

[39] Halekotte L, Feudel U. 2020 Minimal fatal shocks in multistable complex networks. *Scientific Reports* **10**. 6

[40] Hasselmann K. 1976 Stochastic climate models Part I. Theory. *Tellus* **28**, 473–485. 43

[41] Hill K, Zanetell J, Gemmer JA. 2022 Most probable transition paths in piecewise-smooth stochastic differential equations. *Physica D: Nonlinear Phenomena* **439**, 133424. 6

[42] Izhikevich EM. 2006 *Dynamical systems in neuroscience: the geometry of excitability and bursting*. Cambridge, MA: The MIT Press. 10, 11

[43] Jones CKRT. 1995 Geometric Singular Perturbation Theory. In Johnson R, editor, *Dynamical Systems. Lecture Notes in Mathematics*. Berlin, Heidelberg: Springer. 12, 22, 46, 48, 100

[44] Kaur T, Sharathi Dutta P. 2022 Critical rates of climate warming and abrupt collapse of ecosystems. *Proc. R. Soc. A* **478**. 22

[45] Khvorostyanov DV, Ciais P, Krinner G, Zimov SA, Corradi C, Guggenberger G. 2008a Vulnerability of permafrost carbon to global warming.

Part II: sensitivity of permafrost carbon stock to global warming. *Tellus B: Chemical and Physical Meteorology* **60**, 265–275. 3, 22, 32, 34, 35

[46] Khvorostyanov DV, Krinner G, Ciais P, Heimann M, Zimov SA. 2008b Vulnerability of permafrost carbon to global warming. Part I: model description and role of heat generated by organic matter decomposition. *Tellus B* **60**, 250–264. 26, 34, 35, 117, 120

[47] Kiers C, Jones CK. 2019 On conditions for rate-induced tipping in multidimensional dynamical systems. *J. Dyn. Differ. Equ.* **32**, 483–503. 5

[48] Kirschbaum MUF. 1995 The temperature dependence of soil organic matter decomposition, and the effect of global warming on soil organic C storage. *Soil Biology and Biochemistry* **27**, 753–760. 29

[49] Kloeden PE, Rasmussen M. 2011 *Nonautonomous dynamical systems*. Number 176. American Mathematical Soc. 11, 38

[50] Krauskopf B, Schneider K, Sieber J, Wieczorek S, Wolfrum M. 2003 Excitability and self-pulsations near homoclinic bifurcations in semiconductor laser systems. *Optics Communications* **215**, 367–379. 11

[51] Krupa M, Szmolyan P. 2001 Extending Geometric Singular Perturbation Theory to Nonhyperbolic Points—Fold and Canard Points in Two Dimensions. *SIAM J. Math. Anal* **33**, 286–314. 16, 48, 80, 100

[52] Krupa M, Wechselberger M. 2010 Local analysis near a folded saddle-node singularity. *Journal of Differential Equations* **248**, 2841–2888. 16, 70, 80, 100

[53] Kuehn C, Longo IP. 2022 Estimating rate-induced tipping via asymptotic series and a Melnikov-like method*. *Nonlinearity* **35**, 2559–2587. 5

[54] Kuehn C. 2011 A mathematical framework for critical transitions: Bifurcations, fast–slow systems and stochastic dynamics. *Physica D* **240**, 1020–1035. 5

[55] Kuehn C. 2016 *Multiple Time Scale Dynamics*. Springer International PU. 12, 15, 22, 46, 48, 58, 59, 100

[56] Leibman MO, Kizyakov AI, Plekhanov AV, Streletskaya ID. 2014 New permafrost feature – deep crater in Central Yamal (West Siberia, Russia) as a response to local climate fluctuations. *Geography, Environment, Sustainability* **7**, 68–79. 46

[57] Lenton TM, Held H, Kriegler E, Hall JW, Lucht W, Rahmstorf S, Schellnhuber HJ. 2008 Tipping elements in the Earth's climate system. *Proc. Natl Acad. Sci.* **105**, 1786–1793. 3, 4, 5

[58] Levashova N, Sidorova A, Semina A, Ni M. 2019 A Spatio-Temporal Autowave Model of Shanghai Territory Development. *Sustainability* **11**. 11

[59] Longo IP, Nunez C, Obaya R, Rasmussen M. 2021 Rate-induced tipping and saddle-node bifurcation for quadratic differential equations with nonautonomous asymptotic dynamics. *SIAM J. Appl. Dyn. Syst.* **20**, 500–540. 5

[60] Luke CM, Cox PM. 2011 Soil carbon and climate change: from the Jenkinson effect to the compost-bomb instability. *European Journal of Soil Science* **62**, 5–12. 3, 22, 25, 26, 27, 29, 30, 48, 117

[61] Marchionne A, Ditlevsen P, Wieczorek S. 2018 Synchronisation vs. resonance: Isolated resonances in damped nonlinear oscillators. *Physica D* **380**, 8–16. 94

[62] Maruyama S, Moriya S. 2021 Newton's Law of Cooling: Follow up and exploration. *Int. J. Heat and Mass Transfer* **164**. 25

[63] Masson-Delmotte V, Zhai P, Pörtner HO, Roberts D, Skea J, Shukla P, Pirani A, Moufouma-Okia W, Péan C, Pidcock R, Connors S, Matthews J, Chen Y, Zhou X, Gomis M, Lonnoy E, Maycock T, Tignor M, Waterfield Te. 2018 Global Warming of 1.5°C. An IPCC Special Report on the impacts of global warming of 1.5°C above pre-industrial levels and related global greenhouse gas emission pathways, in the context of strengthening

the global response to the threat of climate change, sustainable development, and efforts to eradicate poverty.. *IPCC*. 33

[64] Masson-Delmotte V, Zhai P, Pirani A, Connors SL, Péan C, Berger S, Caud N, Chen Y, Goldfarb L, Gomis M et al.. 2021 Climate change 2021: the physical science basis. *Contribution of working group I to the sixth assessment report of the intergovernmental panel on climate change* **2**. 3

[65] McCarty JL, Smith TEL, Turetsky MR. 2020 Arctic fires re-emerging. *Nature Geoscience* **13**, 658–660. 22, 30, 32

[66] Mishra U, Hugelius G, Shelef E, Yang Y, Strauss J, Lupachev A, Harden JW, Jastrow JD, Ping C, Riley WJ, Schuur EAG, Matamala R, Siewert M, Nave LE, Koven CD, Fuchs M, Palmtag J, Kuhry P, Treat CC, Zubrzycki S, Hoffman FM, Elberling B, Camill P, Veremeeva A, Orr A. 2021 Spatial heterogeneity and environmental predictors of permafrost region soil organic carbon stocks. *Science Advances* **7**, eaaz5236. 3

[67] Mitry J, Wechselberger M. 2017 Folded Saddles and Faux Canards. *SIAM Journal on Applied Dynamical Systems* **16**, 546–596. 83, 114, 118

[68] Mitry J, McCarthy M, Kopell N, Wechselberger M. 2013 Excitable neurons, firing threshold manifolds and canards. *Journal of Mathematical Neuroscience* **3**, 12. 10, 11, 22, 68, 80

[69] Mäkiranta P, Laiho R, Fritze H, Hytönen J, Laine J, Minkkinen K. 2009 Indirect regulation of heterotrophic peat soil respiration by water level via microbial community structure and temperature sensitivity. *Soil Biology and Biochemistry* **41**, 695–703. 3

[70] Nelson M, Marchant T, Wake G, Balakrishnan E, Chen X. 2007 Self-heating in compost piles due to biological effects. *Chemical Engineering Science* **62**, 4612–4619. 30

[71] Nichols JE, Peteet DM. 2019 Rapid expansion of northern peatlands and doubled estimate of carbon storage. *Nature Geoscience* **12**, 917–921. Copy-

right - Copyright Nature Publishing Group Nov 2019; Last updated - 2022-04-18. 3

[72] O'Keeffe PE, Wieczorek S. 2020 Tipping Phenomena and Points of No Return in Ecosystems: Beyond Classical Bifurcations. *SIAM J. Appl. Dyn. Syst.* **19**, 2371–2402. Publisher: Society for Industrial and Applied Mathematics. 5, 30, 93, 102

[73] Overland J, Dunlea E, Box JE, Corell R, Forsius M, Kattsov V, Olsen MS, Pawlak J, Reiersen L, Wang M. 2019 The urgency of Arctic change. *Polar Science* **21**, 6–13. 3, 33

[74] Pachauri RK, Allen MR, Barros VR, Broome J, Cramer W, Christ R, Church JA, Clarke L, Dahe Q, Dasgupta P et al.. 2014 In *Climate change 2014: synthesis report. Contribution of Working Groups I, II and III to the fifth assessment report of the Intergovernmental Panel on Climate Change,*. Ipcc. 33

[75] Perkins-Kirkpatrick SE, Lewis SC. 2020 Increasing trends in regional heatwaves. *Nat. Commun.* **11**. 3, 94

[76] Perryman C, Wieczorek S. 2014 Adapting to a changing environment: non-obvious thresholds in multi-scale systems. *Proc. R. Soc. A* **470**, 20140226. 22, 37, 65, 68, 69, 80, 81, 83, 104, 113

[77] Perryman CG. 2015 *How fast is too fast? Rate-induced bifurcations in multiple time-scale systems*. PhD thesis University of Exeter. 6, 81, 88, 104, 113, 118

[78] Pierini S, Ghil M. 2021 Tipping points induced by parameter drift in an excitable ocean model. *Sci. Rep.* **11**. 11

[79] Quarteroni A, Manzoni A, Vergara C. 2017 The cardiovascular system: Mathematical modelling, numerical algorithms and clinical applications. *Acta Numerica* **26**, 365–590. 11

[80] Rees S, Zhou Z, Thomas H. 2001 The influence of soil moisture content variations on heat losses from earth-contact structures: an initial assessment. *Building and Environment* **36**, 157–165. 27

[81] Rinzel J, Ermentrout GB. 1989 Analysis of Neural Excitability and Oscillations. In , p. 135–169. Cambridge, MA, USA: MIT Press. 10, 11

[82] Ritchie P, Sieber J. 2017 Probability of noise- and rate-induced tipping. *Phys. Rev. E* **95**, 052209. 117

[83] Ritchie P, Karabacak O, Sieber J. 2019 Inverse-square law between time and amplitude for crossing tipping thresholds. *Proc. R. Soc. A* **475**, 20180504. 102, 103

[84] Ritchie PD, Clarke JJ, Cox PM, Huntingford C. 2021 Overshooting tipping point thresholds in a changing climate. *Nature* **592**, 517–523. 4

[85] Rohde R, Muller R, Jacobsen R, Perlmutter S, Mosher S. 2013 Berkeley Earth temperature averaging process. *Geoinformatics I& Geostatistics: An Overview* **01**. 3, 4

[86] Roy J, Saugier B, Mooney HA. 2001 *Terrestrial Global Productivity*. Elsevier. 25

[87] Sawer P. 2022 Wennington Fire: Compost blaze that devastated village started just yards from fire station. *The Telegraph*, 20 July. See `https://www.telegraph.co.uk/news/2022/07/20/wennington-fire-compost-blaze-devastated-village-started-just/`. 3

[88] Scholten RC, Jandt R, Miller EA, Rogers BM, Veraverbeke S. 2021 Overwintering fires in boreal forests. *Nature* **593**, 399–404. 22, 30, 32

[89] Screen JA, Simmonds I. 2010 The central role of diminishing sea ice in recent Arctic temperature amplification. *Nature* **464**, 1334–1337. 3, 33

[90] Sierra CA, Trumbore SE, Davidson EA, Vicca S, Janssens I. 2015 Sensitivity of decomposition rates of soil organic matter with respect to simultaneous changes in temperature and moisture. *Journal of Advances in Modeling Earth Systems* **7**, 335–356. 117

[91] Slyman K, Jones CK. 2022 Rate and Noise-Induced Tipping Working in Concert. *arXiv.* 6, 117

[92] Szmolyan P, Wechselberger M. 2001 Canards in R^3. *J. Differ. Equ.* **177**, 419–453. 16, 23, 48, 67, 68, 69, 70, 80, 100

[93] Tarnocai C, Canadell JG, Schuur EaG, Kuhry P, Mazhitova G, Zimov S. 2009 Soil organic carbon pools in the northern circumpolar permafrost region. *Global Biogeochemical Cycles* **23**. 3

[94] Thompson JM, Sieber J. 2011 Predicting climate tipping as a noisy bifurcation: A Review. *International Journal of Bifurcation and Chaos* **21**, 399–423. 5

[95] Turetsky MR, Abbott BW, Jones MC, Anthony KW, Olefeldt D, Schuur EAG, Grosse G, Kuhry P, Hugelius G, Koven C, Lawrence DM, Gibson C, Sannel ABK, McGuire AD. 2020 Carbon release through abrupt permafrost thaw. *Nature Geoscience* **13**, 138–143. 46

[96] UNFCCC V. 2015 *Adoption of the Paris agreement* vol. 282. Proposal by the President. 33

[97] van der Pol B. 1920 A theory of the amplitude of free and forced triode vibrations. *Radio Review* **1**, 701–710. 20, 22

[98] Vanselow A, Wieczorek S, Feudel U. 2019 When very slow is too fast - collapse of a predator-prey system. *J. Theor. Biol.* **479**, 64–72. 6, 11, 22, 65

[99] Vanselow A, Halekotte L, Feudel U. 2021 Evolutionary rescue can prevent rate-induced tipping. *Theor. Ecol.* **15**, 29–50. 11, 22

[100] Vaughan A. 2020 Arctic 'zombie fires' keep burning beneath the ice. *New Scientist* **246**, 14. 22, 30, 32

[101] Vo T, Wechselberger M. 2015 Canards of Folded Saddle-Node Type I. *SIAM J. Math. Anal* **47**, 3235–3283. 70, 80, 100

[102] Vo T, Bertram R, Wechselberger M. 2013 Multiple Geometric Viewpoints of Mixed Mode Dynamics Associated with Pseudo-plateau Bursting. *SIAM Journal on Applied Dynamical Systems* **12**, 789–830. 10, 83

[103] Waddington JM, Morris PJ, Kettridge N, Granath G, Thompson DK, Moore PA. 2014 Hydrological feedbacks in northern peatlands. *Ecohydrology* **8**, 113–127. 117

[104] Warburton D, Thrower A. 2022 Man claims wennington fire started 'when compost heap spontaneously combusted'. *The Mirror*, 20 July. See `https://www.mirror.co.uk/news/uk-news/man-claims-wennington-fire-started-27525488`. 3

[105] Weber TKD, Iden SC, Durner W. 2017 Unsaturated hydraulic properties of Sphagnum moss and peat reveal trimodal pore-size distributions. *Water Resources Research* **53**, 415–434. 27

[106] Wechselberger M. 2005 Existence and Bifurcation of Canards in $\mathbb{R}^3$ in the Case of a Folded Node. *SIAM J. Appl. Dyn. Syst.* **4**, 101–139. 16, 70, 80, 100

[107] Wechselberger M. 2007 Canards. *Scholarpedia* **2**, 1356. revision #152256. 49

[108] Wechselberger M. 2020 *Geometric Singular Perturbation Theory Beyond the Standard Form*. Springer International Publishing. 12

[109] Wechselberger M, Mitry J, Rinzel J. 2013 Canard Theory and Excitability. In Kloeden PE, Pötzsche C, editors, *Nonautonomous Dynamical Systems in the Life Sciences* pp. 89–132. Cham: Springer International Publishing. 10, 11, 12, 22, 46, 48, 49, 70, 80, 81, 100, 113

[110] Wieczorek S, Krauskopf B, Lenstra D. 2002 Multipulse Excitability in a Semiconductor Laser with Optical Injection. *Physical Review Letters* **88**. 11

[111] Wieczorek S, Krauskopf B, Simpson T, Lenstra D. 2005 The dynamical complexity of optically injected semiconductor lasers. *Physics Reports* **416**, 1–128. 11

[112] Wieczorek S, Ashwin P, Luke CM, Cox PM. 2011 Excitability in ramped systems: the compost-bomb instability. *Proc. R. Soc. A* **467**, 1243–1269. 3, 5, 6, 10, 11, 22, 26, 29, 30, 35, 37, 65, 68, 80, 88, 89, 104

[113] Wieczorek S, Xie C, Ashwin P. 2021a Rate-induced tipping: Thresholds, edge states and connecting orbits. *arXiv preprint arXiv:2111.15497*. 5, 6, 8, 9, 22, 30, 37, 38, 39, 42, 49, 50, 52, 53, 56, 118

[114] Wieczorek S, Xie C, Jones CKRT. 2021b Compactification for asymptotically autonomous dynamical systems: theory, applications and invariant manifolds. *Nonlinearity* **34**, 2970–3000. 22, 37, 38, 39, 40, 42

[115] Wikipedia contributors. 2021 Thermal runaway. *Wikipedia, The Free Encyclopedia*. See `https://en.wikipedia.org/w/index.php?title=Thermal_runaway&oldid=1018731502`. Accessed: 12-May-2021. 31

[116] Wikipedia contributors. 2022 Sphagnum. *Wikipedia, The Free Encyclopedia*. See `https://en.wikipedia.org/wiki/Sphagnum`. Accessed: 20-Dec-2022. 26, 27

[117] Xie C. 2020 *Rate-Induced Critical Transitions*. PhD thesis University College Cork. 6, 12, 37, 58, 83

[118] Xu J, Morris PJ, Liu J, Holden J. 2018 PEATMAP: Refining estimates of global peatland distribution based on a meta-analysis. *CATENA* **160**, 134–140. 3, 4

[119] Yu ZC. 2012 Northern peatland carbon stocks and dynamics: a review. *Biogeosciences* **9**, 4071–4085. 3

[120] Yuan H, Restuccia F, Rein G. 2021 Spontaneous ignition of soils: A multi-step reaction scheme to simulate self-heating ignition of smouldering peat fires. *Int. J. Wildland Fire* **30**, 440. 117

[121] Zimov SA, Schuur EA, Chapin III FS. 2006 Permafrost and the global carbon budget. *Science* **312**, 1612–1613. 32